Carnegie Mellon University

CARNEGIE INSTITUTE OF TECHNOLOGY

THESIS

SUBMITTED IN PARTIAL FULFILLMENT OF THE REQUIREMENTS

FOR THE DEGREE OF Doctor of Philosophy

TITLE The Effects of Microstructural and Thermal Stresses on the Hardness of CVD Deposited α-Al_2O_3 and $TiC_xN_{(1-x)}$ Coatings

PRESENTED BY **Harry Chien**

ACCEPTED BY THE DEPARTMENT OF

Materials Science and Engineering

_____ _____

ADVISOR, MAJOR PROFESSOR DATE

_____ _____

DEPARTMENT HEAD

DATE

APPROVED BY THE COLLEGE COUNCIL

_____ _____

DEAN DATE

The Effects of Microstructural and Thermal Stresses on the Hardness of CVD Deposited α-Al_2O_3 and $TiC_xN_{(1-x)}$ Coatings

Submitted in partial fulfillment of the requirements for

the degree of

Doctor of Philosophy

in

Materials Science and Engineering

Harry Chien

B.S., Materials Science and Engineering, Carnegie Mellon University

M.S., Materials Science and Engineering, Carnegie Mellon University

Carnegie Mellon University

Pittsburgh, PA

May, 2011

Acknowledgement

This work was supported primarily by Kennametal Inc. and the Pennsylvania DCED. Partial support by the MRSEC program of the National Science Foundation under Award Number DMR-0520425 is also acknowledged.

Doctorate Thesis Committee

Dr. Gregory Rohrer (Advisor, Carnegie Mellon University)

Dr. Paul Prichard (Kennametal Incorporated)

Dr. Anthony Rollett (Carnegie Mellon University)

Dr. Yoosuf Picard (Carnegie Mellon University)

Abstract

While chemical vapor deposited coatings have been widely used in many different industries, the influence of the microstructural features and the thermal stress on the macroscopic properties is not well understood. In this thesis, a comprehensive study of the grain size, aspect ratio, texture, hardness, and residual stresses of Al_2O_3 and TiC_xN_{1-x} coatings on four tool inserts is described. To do this, methods were developed to measure microstructural features and calculate residual stresses. A correlation was then established between the residual stress calculated in the observed microstructures and the experimentally measured hardness. Assuming that the observed correlation holds in all cases, the thermal stresses in a number of synthetic microstructures were calculated to isolate the influence of individual microstructural characteristics on the hardness.

Electron backscatter diffraction mapping has been used to study the microstructural features and texture of Al_2O_3 and TiC_xN_{1-x}. The Al_2O_3 layers have [0001] or $[10\bar{1}4]$ texture in the growth direction that are 4.2 to 8.8 times random. The TiC_xN_{1-x} layers have weak [112] or [101] textures in the growth direction and are highly twinned, with coherent twins making up 13%-20% of the grain boundary length. Nanoindentation was used to measure the hardness of the TiC_xN_{1-x} and α-Al_2O_3 layers in each coating. The hardest coatings consist of highly twinned TiC_xN_{1-x} layers with weak [112] texture and α-Al_2O_3 with strong $[10\bar{1}4]$ texture.

Two-dimensional finite element analysis (FEM) is used for the residual stress calculation in these materials. The thermal strains and stored elastic energy in the α-Al_2O_3

layer are larger than those in the TiC_xN_{1-x} layer. Furthermore, the mean value and distribution of stored elastic energy are influenced by the texture in the alumina layer. Coatings with weaker texture have a broader distribution of thermal stresses. Coatings with alumina oriented so that the [0001] direction is parallel to the film growth direction have less stored elastic energy. This is because the thermal expansion perpendicular to [0001] is less than the thermal expansion parallel to [0001] and, therefore, the thermal expansion mismatch between the alumina coating and the substrate is minimized when grains are oriented with [0001] perpendicular to the substrate.

The thermal stresses in hypothetical coatings with synthetic microstructures were also computed. These calculations tested the effects of coating thickness, channel crack spacing, composition of the TiC_xN_{1-x} layer, grain aspect ratio, and cobalt enrichment of the substrate on the thermal stresses. In one set of calculation, AlON was substituted for Al_2O_3. Based on the thermal stresses, it is concluded that the composition of the TiC_xN_{1-x} layer and the cobalt enrichment of the substrate have the greatest impact on coating hardness. The calculation also suggested that the substitution of AlON for Al_2O_3 is a promising potential route for improving hardness.

Table of Contents

THESIS i

Chapter 1 1

Introduction 1

1.1 Multilayer Coating Systems 1

1.1.1 History 1

1.1.2 Typical CVD Coatings for Machine Tools 2

1.1.3 Physical Properties 3

1.1.4 Applications of Coated Tools 4

1.2 Motivation 4

1.3 Hypothesis and Objective 7

Chapter 2 9

Background 9

2.1 CVD Coatings and Substrates 9

2.1.1 Substrates – WC-Co 9

2.1.2 CVD Coatings - Al_2O_3 11

2.1.3 CVD Coatings - TiC_xN_{1-x} 12

2.2 Residual Stress and Crack Formation 13

2.2.1 Sources of Residual Stress 13

2.2.3 Crack propagation 16

2.2.5 Fracture Toughness 20

2.3 CVD Coating texture 20

2.3.1 Basic Crystallography 20

2.3.2 Inverse Pole Figure 22

2.3.3 Texture 22

2.3.4 Misorientation distributions in axis-angle space 23

2.4 Mechanical behavior of Al_2O_3 and TiC_xN_{1-x} coatings 24

2.4.1 Stresses and strains 24

2.4.2 Elastic Energy Density 25

2.5 Hardness of Al_2O_3 and TiC_xN_{1-x} coatings 26

2.6 Finite element models (FEM) for structural analysis 27

2.6.1 Object-oriented finite element (OOF) model 27

2.6.2 Previous Calculations of Thermal Stresses in Coatings Using OOF 27

Chapter 3 29

Microstructural Characterization and Simulation Methods 29

3.1 Sample Geometry 30

3.2 Microstructure and Property Characterization Method 31

3.2.1 Atomic force microscopy (AFM) 31

3.2.2 Electron Backscatter Diffraction Mapping 32

3.2.3 Microstructural Analysis 33

3.2.4 Measurement of mechanical properties 35

3.3 Numerical models for structural analysis 35

3.4 Simulation methods 36

3.4.1 Simulation Procedure and Input Material Properties 36

3.4.2 Simulation Assumptions and Boundary Conditions 37

3.4.3 Modification of the input file to create artificial cracks 39

Chapter 4 ..... **41**

Structure of the Coatings **41**

4.1 Microstructure Findings **41**

4.1.1 Crystal Orientations of TiC_xN_{1-x} 41

4.1.2 Crystal Orientations of Al_2O_3 45

4.1.3 Twin Structures in TiC_xN_{1-x} 48

4.2 X-Ray Diffraction **51**

4.3 Residual Stress and Texture **52**

4.4 Summary **53**

Chapter 5 ..... **54**

Hardness and Cracking **54**

5.1 Hardness **54**

5.2 Cracking **56**

5.3 Fracture Toughness **60**

5.4 Correlation between Microstructure and Hardness **61**

5.5 Correlation Between Indenter Crack Length and Hardness **63**

5.6 Summary **64**

Chapter 6 ..... **66**

Residual stresses **66**

6.1 Effect of misorientation related stresses in the alumina with free boundary conditions. **66**

6.2 Elastic Energies and Strains in Al_2O_3 and $TiC_xN_{(1-x)}$ **68**

6.3 Effect of Cracks on Elastic Energies and Stress Distributions **71**

6.3.1 Boundary Conditions and Materials Property Input 71

6.3.2 Effect of Cracking in Al_2O_3 and TiC_xN_{1-x} 72

6.4 Correlation Between Hardness and Calculated Residual Stress **77**

6.5 Summary **81**

Realistic, microstructure based models of multilayer coatings on WC-Co substrates have been used to compute the thermal stress distribution. Channel cracks relieve stress in the coatings and this stress relief is more effective in thicker coatings. The residual thermal stresses are determined by the texture, thickness, and average crack spacing of the coating. The residual thermal stresses in the coating are inversely related to the hardness of the coating. This relationship provides guidance in the search for improved coatings.**Chapter 7** **81**

Chapter 7 ..... **82**

Thermal Stresses in Hypothetical Coating Structures **82**

7.1 Coating Thickness **82**

7.2 Thermal Stresses in Hypothetical AlON coatings **84**

7.3 Cobalt Enriched Substrate **87**

7.4 TiC_xN_{1-x} with different compositions **91**

7.5 Crack Spacing **94**

7.6 Grain Aspect Ratio **97**

Chapter 8 ..... **100**

Summary **100**
References: **103**
Appendix A **109**
OOF2 Tutorial Guide **109**

List of Tables

Table 1. Physical Properties of the Materials used for the Simulation

Table 2. Twin Populations in TiC_xN_{1-x} coatings

Table 3. Summary of microstructural characteristics and hardness for coatings.

Table 4. Average crack length and average hardness (Fig 9) of Al_2O_3

Table 5. Number of cracks counted manually along the sample width and length.

Table 6. Summary of Measured Properties of the Coatings. Values in parentheses are standard deviations of measured quantities.

Table 7. The materials properties input for the AlON and Al_2O_3 in hypothetical simulation

Table 8. The materials properties input for the cobalt-enriched substrate. The materials properties for the cobalt enriched regions are calculated from the original WC and Co materials properties.

Table 9. The materials properties input for TiC_xN_{1-x}. The materials properties for the different TiC_xN_{1-x} are calculated from the original TiC and TiN materials properties.

List of Figures

Figure 1. Schematic of a TiN coating on top of a WC-Co substrate. (a) shows the unconstrained case where coating and substrate are separate before and after cooling. (b) shows constrained case where coatings are on the substrate before and after cooling.

Figure 2. : Schematic of an anisotropic material on top of WC-Co substrate. (a) shows the unconstrained case where coating and substrate are separate before and after cooling. (b) shows constrained case where coatings are on the substrate before and after cooling. Red arrows are orientations and the red colors in (b) shows the intensities in thermal stress.

Figure 3. SEM image of the (0001) textured α-Al_2O_3 coating. This image was reproduced from reference 30.

Figure 4. TEM image of the microstructure of TiC_xN_{1-x} coating[33]. This image is in cross section view with the substrate at the bottom. This image was reproduced from reference 33.

Figure 5. Some fundamental cracking and decohesion problem, indicating magnitudes of the cracking number λ[37].

Figure 6. Steady-state channeling crack in a thin film. The function g(α,β) and the normalized length defining the in-plane resistance of the substrate[38].

Figure 7. Illustration of the sample reference frame (red) and crystal reference frame (blue). w_i and w_i''' represent unit vectors in both sample and crystal reference frame.

Figure 8. Example of misorientation distributions in axis-angle space of TiC_xN_{1-x}. Scales are multiples of a random distribution (MRD). The misorientation angle is specified at each section.

Figure 9. Schematics of the sample preparation method showing a) area of detail, b) two different methods of polishing, c) cross section view of the polishing method 1, viewed from the [010] axis, and d) cross section view of the polishing method 2, viewed from the [010] axis

Figure 10. Scanning electron microscope (SEM) image of a sample cross section. Layered structure of the coatings and substrate can be observed. Note that the colors for each coating is artificial in SEM.

Figure 11. a) Sample OIM image of TiC_xN_{1-x} coating. b) Ellipse shaped image produced by ImageJ for grain shape information and grain area calculation.

Figure 12. Inverse pole figure maps for the TiC_xN_{1-x} layers in (a) sample 1, (b) sample 2, (c) sample 3, and (d) sample 4. Each color corresponds to a crystal orientation, defined in the key in (d). The 5 μm scalebar in (a) is the same in all four maps.

Figure 13. Inverse pole figures for the TiC_xN_{1-x} layers (a) sample 1, (b) sample 2, (c) sample 3, and (d) sample 4 with [100] (the growth direction) as the reference.

Figure 14. Inverse pole figure maps for the Al_2O_3 layers in (a) sample 1, (b) sample 2, (c) sample 3, and (d) sample 4. Each color corresponds to a crystal orientation on the left. The scale in (c) is the same in all four maps.

Figure 15. Inverse pole figures for the Al_2O_3 layers (a) sample 1, (b) sample 2, (c) sample 3, and (d)

sample 4 with [100] (the growth direction) as the reference.

Figure 16. Misorientation distribution function for the TiC_xN_{1-x} coatings with misorientation of 60° about the [111] axis.

Figure 17. (a) Image quality map of the TiC_xN_{1-x} layer in sample 1. Dark contrast corresponds to poor image quality that is characteristic of patterns recorded at grain boundaries. The red lines denote Σ3 type grain boundaries. (b) The distribution of grain boundary planes for the Σ3 grain boundaries. The distribution is plotted on a stereographic projection. The peak is at the position of the misorientation axis, [111], indicates a high fraction of pure twist grain boundaries with (111) planes on either side of the boundary. This geometry corresponds to the coherent twin

Figure 18. XRD diffraction pattern of the experimental coatings for sample 1 (purple), sample 2 (green), sample 3 (blue), sample 4 (red). The Al_2O_3 peaks are labeled in blue and the TiN peaks are labeled in red.

Figure 19. Measured hardness values across section 2 as a function of position (see Fig. 1d) for sample 1 (circles), sample 2 (squares), sample 3 (diamonds), and sample 4 (triangles). Each data set is offset along the x-axis by 0.25 to minimize overlap of the data. The symbols represent mean values and the bars show ± one standard deviation. Above the graph is a montage of optical micrographs showing the location of the indents in sample 1. The vertical rows of black spots are the multiple indents used to determine the mean and standard deviation of the hardness and the different regions are labeled.

Figure 20. Atomic Force Microscopy deflection images of cracks that extend from the nanoindentation marks. Cracks are highlighted by the red lines.

Figure 21. Schematics of cracks counted along sample length and sample width

Figure 22. Images of the channel cracks in CVD deposited coatings. (a) plane view optical image of the pattern of cracks. (b) SEM image of a transverse section of a coating. The position of the crack is highlighted by the arrows.

Figure 23. Average area of the three divided regions in TiC_xN_{1-x} layer versus the average hardness of position 4, 5, 6 in Fig. 19.

Figure 24. Average crack length for each sample versus the average hardness for each sample.

Figure 25. The stored elastic energy distributions for the four alumina layers computed for $\Delta T = -800$ K and free boundary conditions. The intensity (relative) is indicated by the shading of the figure. (a), (b), (c), and (d) are for sample 1, 2, 3, and 4, respectively.

Figure 26. (a) Histogram of the values of the elastic energy in each element for the four alumina layers computed with free boundary conditions and $\Delta T = -800$ K. (b) Histogram of the values of the stress invariant 1 (trace of the stress tensor) in each element.

Figure 27. The stored elastic energy distributions for the coatings computed for $\Delta T = -800$ K and strained lateral boundary conditions. The intensity (relative) is indicated by the shading of the figure. (a), (b), (c), and (d) are for sample 1, 2, 3, and 4, respectively.

Figure 28. The horizontal component of the strain (ε_{xx}) for the four samples. The magnitude of the strain is indicated by the color. (a), (b), (c), and (d) are for sample 1, 2, 3, and 4, respectively.

Figure 29. (a) Histogram of the horizontal component of the strain (ε_{xx}) for the four samples, based on the data in Fig. 27. (b) Histogram of the stored elastic energy of the four samples, based on the data in Fig. 26.

Figure 30. The thermal stress distribution along the x direction for the samples without cracks (a-d) and the same samples with a crack (e-h). All of the figures have the same scale.

Figure 31. Histogram of the values of the stress invariant 1 in Al_2O_3 (trace of the stress tensor) in each element for the four sample, based on the data in Fig. 30 (e-h).

Figure 32. Histogram of the values of the stress invariant 1 in TiC_xN_{1-x} (trace of the stress tensor) in each element for the four sample, based on the data in Fig. 30 (e-h).

Figure 33. The elastic energy density distribution for all for samples without cracks (a-d) and with a single crack in the center (e-h). All of the figures have the same scale.

Figure 34. Schematics of thermal stress of coatings with different thickness before and after crack formation. The bottom black color represents the substrate whereas the orange color represents stress in the coating. Red color shows the amount of thermal stress relieved. Darker red color means more stress relieved.

Figure 35. (a) Coating Thickness Versus Thermal Residual Stress for TiC_xN_{1-x}. (b) Coating Thickness versus Residual Thermal Stress for α-Al_2O_3. In each case, the numbers refer to the sample coating. Blue data points refer to the coatings without cracking and black data points refer to the coatings with cracking.

Figure 36. (a) Hardness Versus Thermal Residual Stress for TiC_xN_{1-x}. (b) Hardness Versus Residual Thermal Stress for a-Al_2O_3. In each case, the numbers refer to the sample coating.

Figure 37. Examples of hypothetical microstructures with stress distribution. Simulation is performed on TiCN coatings with 2 μm, 4 μm, and 6 μm thickness without cracks (a-c) and with a single crack in the center (d-f). All the figures have the same scale.

Figure 38. Average stress of the TiC_xN_{1-x} coating with different thicknesses. Stress decreases as coating thickness increases when the crack is added. Blue data points refer to simulations with no crack whereas black data points refer to simulations with crack.

Figure 39. Examples of hypothetical microstructures with stress distribution. (a) and (b) show stress distribution in the AlON and Al_2O_3 without cracking. (c) and (d) shows the stress distribution in AlON and Al_2O_3 with cracking.

Figure 40. Average thermal stress in AlON and Al_2O_3 coating. Blue data points refer to simulations with no crack whereas black data points refer to simulations with crack.

Figure 41. Thermal Stress for Al_2O_3 and TiC_xN_{1-x} on different cobalt-enriched substrate. (a) shows the effect of having two (25%, and 12%) cobalt enriched substrate on top of 3%WC-Co. (b) shows 25% cobalt enriched substrate. (c) shows 12% cobalt enriched substrate, and (d) shows only the uniform 3% cobalt content WC-Co. Note the scale ranges from 750 MPa to -750 MPa which is different compared to other simulations.

Figure 42. Average thermal stress in TiC_xN_{1-x} coating with different cobalt enriched content. Higher cobalt-enriched regions have smaller thermal stress.

Figure 43. Examples of hypothetical microstructures with stress distribution. Simulation is performed on TiC_xN_{1-x} coatings with x = 0.1, 0.3, 0.5, 0.7, 0.9 for (a) ~ (e) and x = 0.1, 0.3, 0.5, 0.7, 0.9 with cracking in (f-j). All the figures have the same scale.

Figure 44. Thermal stress of TiC_xN_{1-x} coating with different x values. The thermal stress decreases with increasing x value. Blue data points refer to those simulations without cracking and red points refer to the simulations with cracking.

Figure 45. Examples of hypothetical microstructures with stress distribution. Simulation is performed on 4 μm TiC_xN_{1-x} coatings with crack spacing decreasing from 90 μm, 70 μm, 50 μm, 30 μm, to 10 μm shown in (a) to (e).

Figure 46. Examples of hypothetical microstructures with stress distribution. Simulation is performed on 8 μm TiC_xN_{1-x} coatings with crack spacing decreasing from 90 μm, 70 μm, 50 μm, 30 μm, to 10 μm shown in (a) to (e).

Figure 47. Average thermal stress of TiC_xN_{1-x} coating with different crack spacing. Smallest crack spacing result in higher thermal stress. The lowest thermal stress lies on where the 50 μm crack spacing is.

Figure 48. Microstructures used to measure the thermal stress with different gain aspect ratio shown in (a) to (c). Hypothetical grains with different aspect ratios are stacked in (d) and (e).

Figure 49. Examples of hypothetical microstructures with stress distribution. The average stress decreases as the grain aspect ratio increases. The grains that are stacked (d) ~ (e) have thermal stresses that depends on the texture.

Figure 50. Examples of hypothetical microstructures with stress distribution. Simulation is performed on TiC_xN_{1-x} coatings with x = 0.1, 0.3, 0.5, 0.7, 0.9 for (a) ~ (e) and x = 0.1, 0.3, 0.5, 0.7, 0.9 with cracking in (f-j). All the figures have the same scale.

Figure 51. Schematic illustration of the effects of microstructural features and coating deposition parameters on the hardness.

Chapter 1

Introduction

Coatings are well known for increasing the lifetime and improving the performance of cutting tools. Since the 20th century, coatings have been widely used on cemented carbide tools that benefit from their combination of high chemical and wear resistance, hardness, and strength. This chapter provides a brief overview of chemical vapor deposited coatings, describes the motivation for the current work, and defines the objectives of this thesis.

1.1 Multilayer Coating Systems

1.1.1 History

Chemical vapor deposition (CVD) is a relatively mature technique. However, it was not until the 1970s that a considerable in-depth understanding of the process was achieved. Simultaneously, the number of applications of CVD increased[1-2]. The industrial exploitation of CVD can be traced back to Peterson's[3] discovery in 1964 of a method of forming highly adherent thin metal oxide films on suitable substrates at 200°C. Stroupe et al.[4] then disclosed a method of forming titanium carbide (TiC) coatings on metal or composite substrates to produce parts with extremely hard, wear resistant surfaces. Stroupe's method describes the deposition of TiC coatings by reacting a volatile hydrocarbon and a titanium halide in hydrogen at the surface of the metal. Using a similar

method, Hale[5] disclosed a cemented carbide product covered with a dense coating of alumina in 1971. At this time, CVD technology subsequently took on new dimensions with emphasis on the deposition aspects of the process. The evolution of the deposition process has made CVD an important technique in coating technology for producing functional thin films and coatings with improved surface properties such as protection against wear, corrosion, oxidation, chemical reaction, and thermal shock.

In the early 1970s, CVD attained significant success in the manufacturing of electronic semiconductors and protective coatings for electronic circuits. This supported rapid expansion of CVD technology into many other areas of ceramic processing such as thermal barrier coatings for high temperature turbine blades and ceramic fibers. In 1973, Post et al.[6] discovered that applying an additional coating layer of titanium nitride (TiN) over TiC could further extend the useful life of TiC coated wear surfaces. This technique has been extended and it is now common for CVD coatings to be comprised of multiple materials. In fact, most of the protective coatings are now deposited in the form of multilayers or compositionally graded coating systems containing a combination of different materials for improved component lifetime.

1.1.2 Typical CVD Coatings for Machine Tools

Throughout this dissertation, the phrase 'CVD coatings' will be used to refer to wear resistant hard coatings on tools applied by CVD. Many different materials can be used as CVD coatings. Chromium, Al_2O_3, TiC, Fe_4N, and TiN are commonly used, and other materials are being studied[1]. Usually these CVD coatings have thicknesses that range from 3 to 20

μm. Among all the CVD coatings, Al_2O_3, TiC, TiN, and TiC_xN_{1-x} are typically used on bulk composite cutting tools. Comparing the properties of these coatings, Al_2O_3 has good wear and corrosion resistance, but it has low thermal shock resistance, low strength, and high brittleness. These characteristics can be complemented by the titanium based coatings such as TiN[7]. The most popular wear-resistant coatings are TiC and TiN, which are used to coat high-speed, cold-work die and hot-work die tool steels[8-9].

1.1.3 Physical Properties

The physical properties of these coatings depend on microstructural features such as grain size, grain aspect ratio, orientations, and misorientations[10]. Titanium carbonitride coatings have a hardness that ranges from 21 to 23 GPa[11], and a coefficient of thermal expansion (CTE) that ranges from 7.6 to $9.5x10^{-6}/K$[12,13]. Alumina coatings have hardnesses that range from 23 to 25.5 GPa[11] and a CTE of $8.3x10^{-6}/K$ along the a-axis and $9.35x10^{-6}/K$ along the c axis[14]. It is also known that the chemical and wear resistances of these coatings are three to five times higher than that of an uncoated cutting tool[15]. The details of the physical properties of the WC-Co substrate will be described in section 2.1.3. It should be noted that while the relationship between the mechanical properties and the mean grain size is known, the influence of grain shape, orientation, and misorientation are not yet clear. Furthermore, it is not clear how changing these microstructural characteristics beyond normally observed ranges alters the properties of the cutting tools.

1.1.4 Applications of Coated Tools

CVD-coated cemented carbides are employed in a variety of metal cutting applications, including turning, boring, parting, threading, grooving, and milling[16]. They are used in machining carbon, alloy, and stainless steels and gray and ductile cast irons, covering a wide range of speeds and feeds[8,17]. Some WC-Co substrates are produced to have a thin cobalt-enriched region near the surface; these are referred to as edge-toughened substrates[15]. Coated tools produced from such substrates can handle medium to heavy roughing to semifinishing operations on cast irons and high-temperature alloys, as well as stainless, low-carbon, and alloy steels. The broad application range of cobalt-enriched tools enables them to cover a large percentage of the metalcutting operations in a plant.

1.2 Motivation

The use of high temperatures in CVD ensures good bonding between the coating and the substrate. However, the CTEs of the coating materials (TiC, TiN, TiCN, and Al_2O_3) are higher than that of the WC-Co based substrate, so CVD coatings are in residual tension at room temperature. Fig. 1 shows schematics of a TiN coating on top of a WC-Co substrate when the temperature is decreased. In the unconstrained case in Fig 1(a), the TiN coating and WC-Co substrate shrink after the temperature is decreased. The TiN coating shrinks more because it has a higher CTE. In the constrained case in Fig 1(b), the TiN coating is deposited on the WC-Co substrate and residual stresses form in the TiN coating as the temperature decreases. These thermal residual stresses may be partially relieved by

through-thickness cracks that form in the coating. These cracks do not significantly affect the adhesion of the coatings, but they may initiate tool failure during machining.

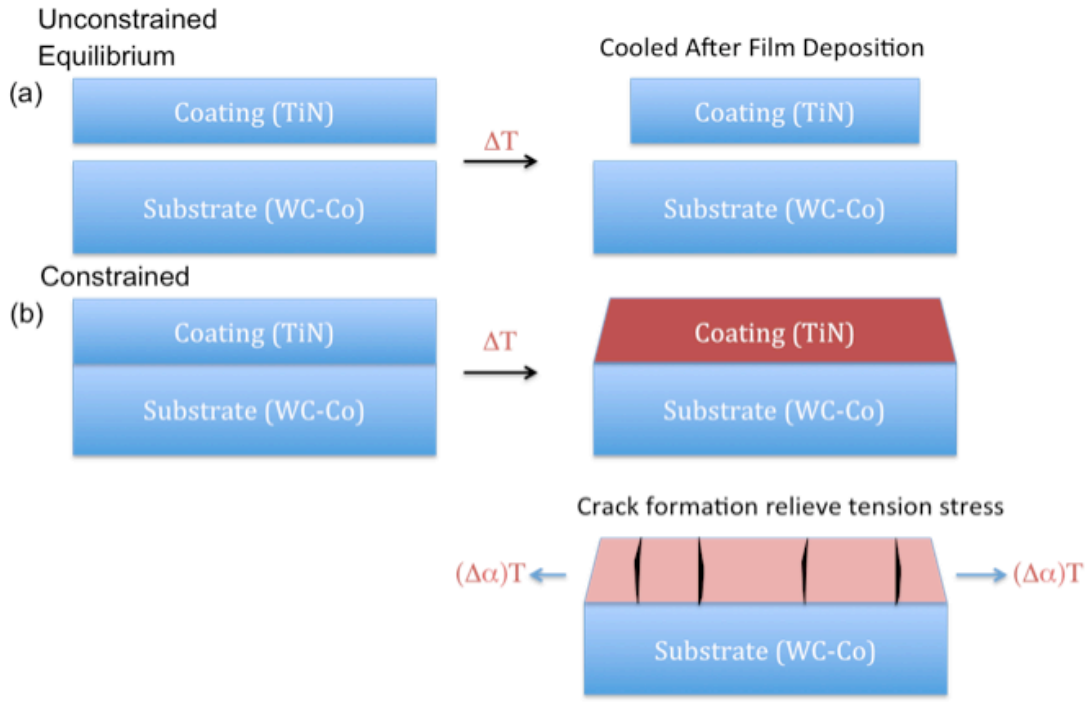

Figure 1. Schematic of a TiN coating on top of a WC-Co substrate. (a) shows the unconstrained case where coating and substrate are separate before and after cooling. (b) shows constrained case where coatings are on the substrate before and after cooling.

For alumina coatings, the CTE along the crystal c-axis direction is greater than the CTE along the a-axis. Grains that are aligned in different directions will shrink by different amounts during cooling. Figure 2 shows a schematic of alumina on a WC-Co substrate when the temperature is decreased. In the unconstrained case in Fig 2(a), the alumina coating has grains that are aligned in different crystal directions. As the temperature decreases, grains that have their c-axis aligned along the horizontal direction shrink more than the grains that have their a-axis aligned along the horizontal direction. In the constrained case in Fig 2(b), the coating is under tension. Grains with their c-axis aligned along the

horizontal direction will have the largest tensile thermal stresses of all orientations, while those aligned in the perpendicular orientation will have the smallest stresses. In real alumina coatings, not all grains are perfectly aligned as in the schematic, thus there will be a distribution of thermal stress. One of the goals of this work is to model these stresses for realistic microstructures.

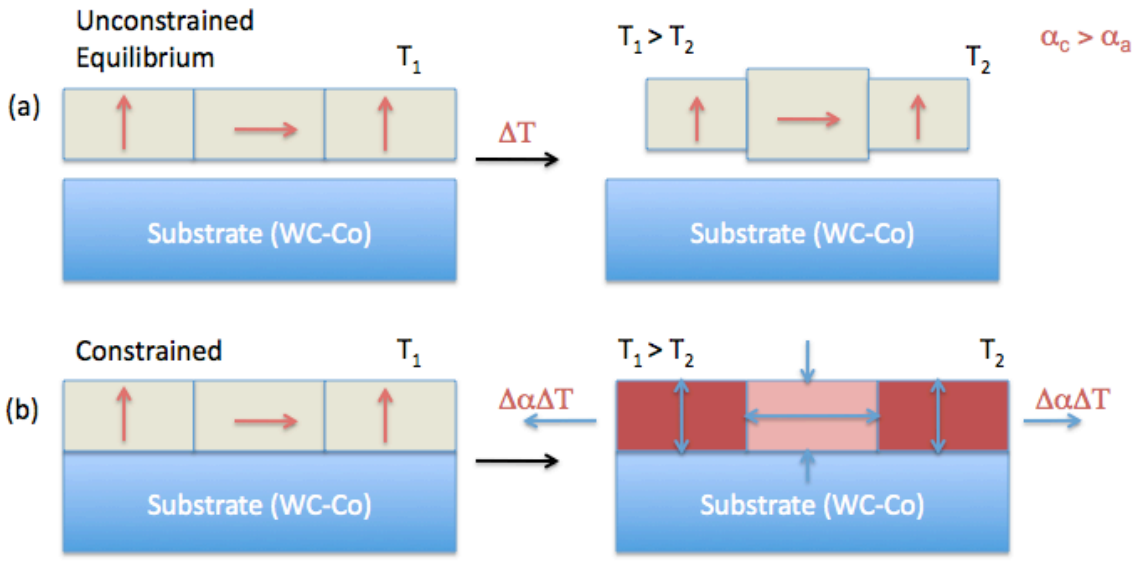

Figure 2. : Schematic of an anisotropic material on top of WC-Co substrate. (a) shows the unconstrained case where coating and substrate are separate before and after cooling. (b) shows constrained case where coatings are on the substrate before and after cooling. Red arrows are orientations and the red colors in (b) shows the intensities in thermal stress.

In this thesis, I focus on CVD Coatings of TiC_xN_{1-x} ||α-Al_2O_3||TiN on WC/Co substrates. In these coatings, the TiC_xN_{1-x} ($0.3 < x < 0.5$) and α-Al_2O_3 layers are each less than 10 μm thick and the TiN-capping layer is approximately 1 μm thick.

1.3 Hypothesis and Objective

Like many other engineering materials, the mechanical properties of CVD deposited coatings are strongly influenced by their microstructure[18]. While the qualitative effects of microstructural variables on the mechanical performance are relatively well understood, the quantitative functional relationship between micro- and macro- features and their fundamental underpinnings are not well established. This work focuses on an analysis of relationship between microstructural and mechanical properties. As microstructural parameters, we include the conventional factors, such as grain size, grain shape, grain aspect ratio, microtexture and size distribution of Al_2O_3 and TiC_xN_{1-x} grains. As a mechanical property parameter, I mainly focus on hardness. While it is probably unrealistic to correlate a single property to any particular figure of merit for the performance of a coating in a metal cutting operation, it is generally true that harder coatings perform better. Unfortunately, there is no straightforward way to directly compute the hardness of the coating from knowledge of the microstructure. However, it is possible to compute the residual thermal stresses using finite element analysis. This leads to the formulation of a hypothesis: the distribution of residual stresses calculated by the finite element method can be correlated to measured hardness. If the hypothesis is correct, then the residual stress model can be used to determine the most influential parameters that determine hardness and predict the hardnesses of hypothetical microstructures.

There are several objective that will have to be reached to test this hypothesis, which are enumerated below:

1) Establish a reliable method for the accurate measurement of microstructural features of Al_2O_3 and TiC_xN_{1-x}.films. These data will be used to search for relationships between microstructural parameters and the hardness of the coatings.

2) Develop a numerical simulation model to predict the thermal stresses as a function of microstructure, composition, coating thickness and coating layer structure. The thermal stresses calculated using the measured microstructures as input will then be compared to the measured hardnesses of the coatings to determine whether a correlation can be established.

3) Use the model to calculate the sensitivity of residual thermal stresses to the structure and properties of the film components.

A model that can be used to predict mechanical properties of hypothetical microstructures would be valuable for the development of new coatings. The value of using a model for the development of new coatings, compared to experiment, is that the relative hardness can be predicted for hypothetical materials and microstructures with controlled and nearly independent variations in the microstructural parameters. By testing such hypothetical materials, it will be possible to identify the most important microstructural characteristics that affect hardness and performance.

Chapter 2

Background

This chapter begins with some background on the CVD coatings and tool substrates. Next, the relevant aspects of crystallography are described. This is followed by a short review of the mechanical behavior and hardness measurements of the coatings. Finally, finite element models (FEM) for stress-strain field calculations are presented.

2.1 CVD Coatings and Substrates

2.1.1 Substrates – WC-Co

WC-Co composites have outstanding mechanical properties that make them commercially useful in machining and cutting. Since the 20th century, WC-Co tools have been widely used in many manufacturing processes that benefit from their combination of high hardness, fracture toughness and wear resistance[19-20]. WC-Co has high deformation resistance, toughness, and thermal shock resistance and can be designed to meet the demands of specific applications which may require impact, abrasion, and/or corrosion resistance.

This thesis is focused on CVD coatings that are deposited on WC-Co substrates. Previous research focused on WC-Co used Electron Backscattered Diffraction (EBSD) to determine the crystallographic orientation distribution of WC crystals in a WC-Co composite[21,22,23,24]. A stereological technique that combines orientation data, measured by

EBSD, and geometric data measured by atomic force microscopy (AFM), was employed to determine the habit planes of surfaces and grain boundaries in WC-Co composites[25]. It was found that $(10\bar{1}0)$ prism facets and the (0001) basal planes are the surfaces that are most frequently in contact with Co. Furthermore, finite element simulations were used to study the effects of orientation texture on the transverse rupture strengths of WC-Co composites. By comparing the calculated fractured strength based on finite element simulations and measured rupture strength, a model for predicting the strengths of WC-Co was developed[26]. It has been shown that the greatest potential for increasing the strength occurs when the [001] axes of the carbide grains are orientated perpendicular to the sample loading direction. Hypothetical structures showed that the textured-derived strength enhancement is greater in microstructures with large contiguity.

As noted in chapter 1, the residual tensile stresses in CVD coatings can also produce transverse cracks in the coatings. The effect of these cracks is not well understood. If there are no cracks in the coating, the film will be under high stress which could create crack initiation sites at any point. On the other hands, if the crack spacing is too small, the structural integrity of the coating will be reduced. A reasonable hypothesis is that there is an ideal crack spacing that lowers the residual stresses without degrading the adherence or structural integrity of the coating.

The cracks may initiate tool fracture in cutting operations in which the cutting edge is subjected to fatigue-type loading. One solution to this problem is to improve the fracture toughness of the substrate by increasing the cobalt content (cobalt enrichment). The cobalt-enriched surface zone, which is 10 to 40 μm thick, provides superior edge strength while maintaining the wear resistance of the coating layer.

2.1.2 CVD Coatings - Al_2O_3

It is well known that alumina has several different crystallographic polymorphs, the gamma, delta, eta, theta, kappa, and alpha phases.[27] Only two of these are of interest for CVD applications: the stable α-Al_2O_3 and the metastable κ-Al_2O_3 polymorphs. α-Al_2O_3 has a trigonal Bravais lattice with a space group of $R\bar{3}c$. The oxygen ions nearly form a hexagonal closed-packed structure with aluminum ions filling two-thirds of the octahedral interstices. The hexagonal lattice constants are a = 4.758 Å and c = 12.991 Å with c/a = 2.73. A typical scanning electron microscope image is shown in Fig. 3. It is clear that the cross sections of α-Al_2O_3 coatings have a columnar structure.

Several studies were done to compare the suitability of α-Al_2O_3 and κ-Al_2O_3 for applications as protective coatings [28-31]. In some cases, the alumina is deposited as the kappa phase, and then transforms to alpha[28,29]. The time to fully transform to α-Al_2O_3 is about five times longer when the temperature is above 1030°C compared to 800°C. The stacking sequence is changed from ABAC for metastable κ-Al_2O_3 to ABAB for stable α-Al_2O_3 polymorphs during the transformation. By comparing κ-Al_2O_3 and α-Al_2O_3, the as-grown α-Al_2O_3 has higher hardness and modulus as well as superior cutting performance in comparison to κ-Al_2O_3[30]. It was also shown that the texture of α-Al_2O_3 influences the wear resistance and performance of the tool especially in turning steel. Alumina coatings with (0001) and $(10\bar{1}4)$ textures exhibited highest hardness and modulus. The best wear resistance was obtained when (0001) planes were nearly parallel to the coating surface[31].

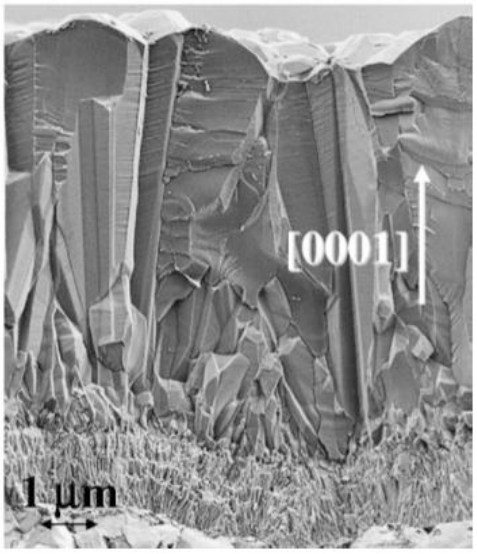

Figure 3. SEM image of the (0001) textured α-Al_2O_3 coating. This image was reproduced from reference 30.

2.1.3 CVD Coatings - TiC_xN_{1-x}

TiN can be deposited on cemented carbides to protect cutting tools. It can also be deposited on stainless steel to strengthen implants used in the human body[9]. It is believed that the performance of the implant could be enhanced by TiN due to its excellent resistance to corrosion and wear. TiC has often been compared with TiN which, despite its low chemical stability and oxidation resistance, has high hardness which can complement TiN. It was shown that the wear resistance of TiC was about two times larger than TiN[32]. Today, manufacturers combine both TiN and TiC into titanium carbon nitride (TiC_xN_{1-x}). The composition, x, can be adjusted for either better oxidation resistance or high hardness depending on the application. In this thesis, TiC_xN_{1-x} is studied with a composition of x

approximately equal to 0.5. However, hypothetical coatings with different compositions are also considered.

Previous research has shown that the grains in a TiC_xN_{1-x} coating have a columnar structure[33]. They are twinned along the growth direction, with a [112] texture. Both titanium nitride (TiN) and titanium carbide (TiC) have a cubic structure with space group $m\bar{3}m$. The lattice constants of TiN and TiC are 4.24 Å and 4.31 Å respectively. A typical transmission electron microscope image of a TiC_xN_{1-x} coating cross section shown in Fig. 4.

Figure 4. TEM image of the microstructure of TiC_xN_{1-x} coating[33]. This image is in cross section view with the substrate at the bottom. This image was reproduced from reference 33.

2.2 Residual Stress and Crack Formation

2.2.1 Sources of Residual Stress

Residual stresses arise because of thermal expansion differences between the substrate and coating. Because the substrate is so much thicker than the coatings, the coatings are constrained to change shape with the substrate and elastic strains develop in

the films. The coefficient of thermal expansion of the substrate is smaller than that of the coatings, so at room temperature, the coatings are loaded in tension.

When the substrate and the coatings respond to changes in temperature in an elastic manner, the misfit residual stress is defined by

$$\sigma = E\Delta a(T_R - T) \tag{2.1}$$

where T is the ambient temperature. T_R is the reference temperature when the coatings are deposited. Δa is the mismatch in thermal expansion between the layer and substrate. E is the Young's modulus of the reference layer.

Considering the relative values of the thermal expansion coefficient (7.67 x 10^{-6}) and modulus (500 GPa) of Al_2O_3, and cooling temperature of -800°C above room temperature, the expected residual stress arising from thermal expansion mismatch (7.67 x 10^{-6} minus 6.52 x 10^{-6}) are on the order of 460MPa. The scale of expected residual stress for the titanium based coatings, we assume a modulus of 550 GPa, a temperature difference of -1200°C (because of the higher deposition temperature), and a higher thermal expansion mismatch of 9.35 x 10^{-6} minus 6.52 x 10^{-6}. This leads to thermal stresses on the order of 1 to 2 GPa.

The second source of residual thermal stress is the anisotropic thermal expansion of α-Al_2O_3. The linear coefficient of thermal expansion (CTE) along the *a*-axis is smaller than along the *c*-axis. Therefore, if there is any misalignment between adjacent grains, incompatible shape changes during cooling lead to residual stresses. These stresses are referred to as misorientation stresses. These stresses have been measured experimentally[34] and modeled[35]. The experimental result showed a range of thermal stress

between 250 to 500 MPa and the modeled result showed a maximum thermal stress of 530 MPa.

2.2.2 Crack Formation

The basic mechanics needed to predict the onset of either the surface debonding or cracks in the ceramic have been established[36]. A fundamental discovery from mechanics is that many of the cracking and decohesion problems in stressed multilayer structures are subject to a steady state energy release rate. When this energy release rate is equated to the relevant fracture energy, a crack initiation site can be found. Also this condition is associated with a critical layer thickness h_c having non-dimensional form.

$$E\Gamma/h_c(\sigma)^2 = \lambda \tag{2.2}$$

where λ is a configuration dependent, non-dimensional cracking number and Γ is the relevant fracture energy (ceramic or interface). The significance of this result is that cracking and decohesion occurs when $h>h_c$. When only small flaws are present, film cracks will not begin to spread until the pre-stress or film thickness exceeds the steady-state requirement.

Different modes of cracking are illustrated in Fig. 5. For surface channeling cracks, the relevant toughness Γ is the film toughness. For debonding, it is the interface toughness Γ.

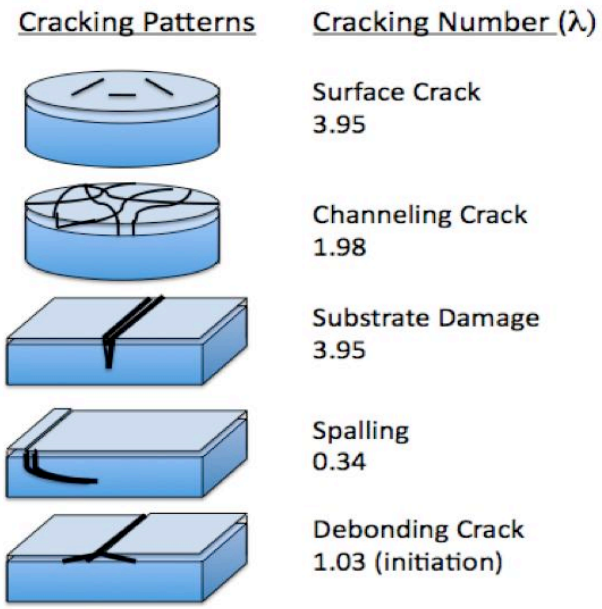

Figure 5. Some fundamental cracking and decohesion problem, indicating magnitudes of the cracking number λ[37].

2.2.3 Crack propagation

When the relevant fracture energy is greater than the energy release rate, the crack will channel through the film and the crack will have an assumed curved shape so that the energy release rate is the same at all points along it[38].

The Nakamura-Kamath study shows that steady state conditions can be achieved by channeling cracks[39]. They present a full 3D analysis of crack channeling for film bonded to a rigid substrate. It was shown that in this limiting case, steady state conditions are achieved by channeling cracks having lengths about twice the film thickness. The solution for steady state channeling in films been presented by Beuth[38], and further relevant mechanics and results are summarized in the review article by Hutchinson and Suo[36]. Beuth's result for

the energy release rate averaged over the advancing front of a semi-inifinite isolated crack is

$$G = \frac{\pi}{2}\frac{(1-\nu^2)h\sigma^{0^2}}{E}g(\alpha, \beta) \tag{2.3}$$

where h is the film thickness, E and ν are the Young's modulus and Poisson's ratio of the film. Film thickness is directly proportional to the energy release rate. The Dundur's parameters, α and β, characterizing the elastic mismatch between the film and the substrate are

$$\alpha = \frac{\bar{E} - \bar{E}_s}{\bar{E} + \bar{E}_s} \tag{2.4}$$

and

$$\beta = \frac{1}{2}\frac{\mu(1-2\nu_s) - \mu_s(1-2\nu)}{\mu(1-\nu_s) + \mu_s(1-\nu)} \tag{2.5}$$

where E_s and ν_s are the elastic constants of the substrate. $\mu = E/(2(1+\nu))$ denotes a shear modulus and $E = E/(1-\nu^2)$ is a plane strain tensile modulus. The equation of energy release G above applies for cracks extending down to the film/substrate interface with uniform pre-stress in the film acting normal to the crack line. The pre-stress has no shear component acting parallel to the crack. The function $g(\alpha,\beta)$ is presented in Fig. 6.

By applying this equation to the TiC_xN_{1-x} and Al_2O_3 coatings that are of interest in this thesis. The calculated energy release rate for TiC_xN_{1-x} and Al_2O_3 are 4.57 GPa – μm and

2.25 GPa – μm. The numbers used for calculating the energy release rate for TiC_xN_{1-x} is 625 GPa, 0.23, and 800 for young's modulus, poisson's ratio, and residual stress. Assuming that the thickness is 8 μm. The numbers used for calculating the energy release rate for Al_2O_3 is 497 GPa, 0.21, and 500 MPa for young's modulus, poisson's ratio, and residual stress. For the substrate, the young's modulus and poisson's ratio used for the calculation is 695 GPa and 0.24. Depending on its thickness, thickner coatings have higher energy release rate.

For the steady state condition, the total work release per unit length of crack propagation can be arrived at by subtracting the energy stored in a unit slice far behind the crack front from that of a unit slice far ahead of the crack front.

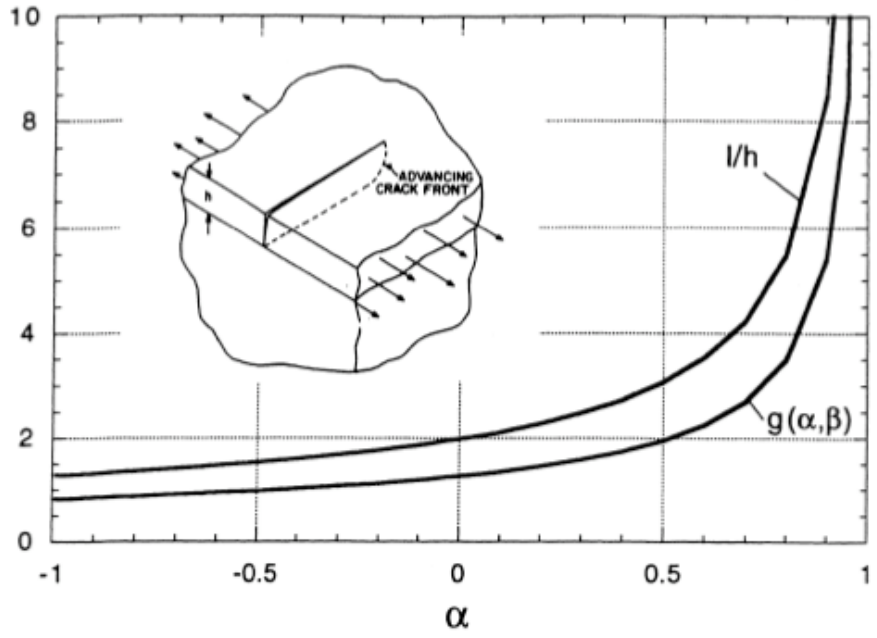

Figure 6. Steady-state channeling crack in a thin film. The function g(α,β) and the normalized length defining the in-plane resistance of the substrate[38]. This figure is reproduced from reference 38.

2.2.5 Fracture Toughness

Fracture toughness is a measure of the energy required for mechanical failure. The general procedure for measuring fracture toughness involves indenting and pre-cracking the specimen, applying a load where crack grows, and measurement of the crack advancement. Fracture toughness is not an intrinsic property. It depends not only the material being fractured but also the size of the material being fractured. The plane strain fracture toughness can be estimated:

$$K_c = 1.076 X_v \left(\frac{a}{l}\right)^{1/2} \left(\frac{E}{H}\right)^{2/3} \left(\frac{P}{c^{3/2}}\right)$$

Where K_c is the fracture toughness, X_v is an empirical constant 0.015[9], a is the distance between the center of the indent to any of the tip corners, c is the crack length that extends out from the indent tip corner, *l* is the overall crack length (c+a), E is the elastic modulus, H is the hardness, and P is the maximum load. In this case, P = 766 mN and a = 7.5 microns and measured values of the modulus, hardness, and crack length are used for the other parameters.

2.3 CVD Coating texture

2.3.1 Basic Crystallography

There are two reference frames to describe the orientation of grains in polycrystals. They are the sample reference frame and the crystal reference frame. To transform the

sample reference frame into the crystal reference frame, three Euler angles (φ_1, ϕ, φ_2) are used. Euler angle defines a sequence of rotations from one reference frame to another reference frame.

If w_i is denoted as the sample reference frame, to reach crystal reference frame, w_i will first yield w_i' by a rotation of φ_1 around the z direction. w_i' will yield to w_i'' by a rotation of ϕ around the x' direction. Noted that during the second rotation, the x' direction is the orientation of x after the first rotation. Finally, w_i'' will yield w_i''' by a rotation of φ_2 around the z'' direction. w_i''' are three unit vectors in crystal reference frame. Here the Euler angle notation is that of Bunge[38]. Using these three successive rotations, it is possible to construct one transformation matrix (g), which converts the laboratory coordinate system to the crystal coordinate system. A schematic of this is shown in Fig. 7.

$$g(\varphi_1,\Phi,\varphi_2) = \begin{pmatrix} \cos\varphi_1\cos\varphi_2 - \sin\varphi_1\sin\varphi_2\cos\Phi & \sin\varphi_1\cos\varphi_2 + \cos\varphi_1\sin\varphi_2\cos\Phi & \sin\varphi_2\sin\Phi \\ -\cos\varphi_1\sin\varphi_2 - \sin\varphi_1\cos\varphi_2\cos\Phi & -\sin\varphi_1\sin\varphi_2 + \cos\varphi_1\cos\varphi_2\cos\Phi & \cos\varphi_2\sin\Phi \\ \sin\varphi_1\sin\Phi & -\cos\varphi_1\sin\Phi & \cos\Phi \end{pmatrix} \quad (2.6)$$

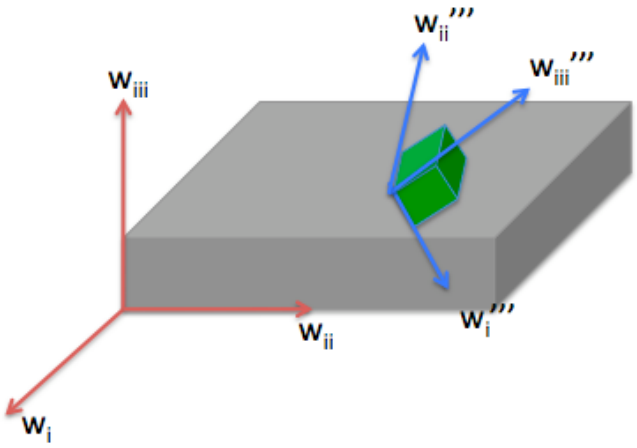

Figure 7. Illustration of the sample reference frame (red) and crystal reference frame (blue). w_i and w_i''' represent unit vectors in both sample and crystal reference frame.

2.3.2 Inverse Pole Figure

An inverse pole figure (IPF) shows the selected directions in the sample reference frame relative to the crystal reference frame. A pole figure, on the other hand, has only the symmetry of the sample reference frame and is therefore plotted on the complete stereographic projection of a hemisphere. A (100) IPF shows the crystallographic directions in a material that are parallel to the (100) sample direction. In a polycrystalline specimen, the distribution of these directions provides and an indication of the texture.

2.3.3 Texture

Texture is the non-uniform occurrence of an orientation, misorientation, or/and grain boundary plane nomal. Here the amount of texture is quantified in units of multiples of a random distribution (MRD). In this thesis, pole figures and inverse pole figures are

measured by EBSD mapping. They are then used to evaluate the texture of the coatings. The texture of the Al_2O_3 and TiC_xN_{1-x} coatings will be compared in Chapter 4.

2.3.4 Misorientation distributions in axis-angle space

One way to describe misorientation distributions is to use misorientation axis-angle pairs. Any misorientation can be defined by a transformation from a sample reference frame to the local reference frame of the crystalline lattice. The misorientation distribution describes the probability of the misorientation between two grains falling into a range $d\Delta g$ around a given misorientation Δg. Fig. 8, an example of misorientation distributions for TiC_xN_{1-x} boundaries is illustrated in axis-angle space. Each standard triangle contains the misorientation axis distributions at a specific misorientation angle.

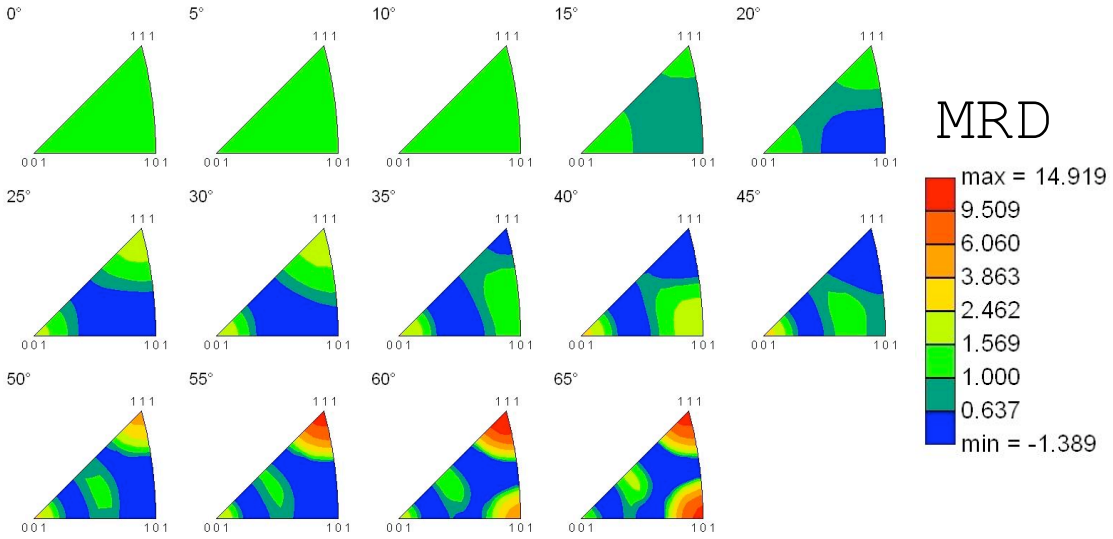

Figure 8. Example of misorientation distributions in axis-angle space of TiC_xN_{1-x}. Scales are multiples of a random distribution (MRD). The misorientation angle is specified at each section.

2.4 Mechanical behavior of Al_2O_3 and TiC_xN_{1-x} coatings

2.4.1 Stresses and strains

Stresses (σ_i) and strains (ε_j) are 2nd rank tensors. In the stress and strain tensors, the first subscript denotes the normal of the plane and the second subscript denotes the direction of force. Note that the stiffness tensor s_{ijkl} can also be represented as c_{ijkl}.

$$\sigma_{kl} = s_{ijkl}\,\varepsilon_{ij} \tag{2.7}$$

$$\sigma_{ij} = \begin{bmatrix} \sigma_{11} & \sigma_{12} & \sigma_{13} \\ \sigma_{21} & \sigma_{22} & \sigma_{23} \\ \sigma_{31} & \sigma_{32} & \sigma_{33} \end{bmatrix} \tag{2.8}$$

$$\varepsilon_{ij} = \begin{bmatrix} \varepsilon_{11} & \varepsilon_{12} & \varepsilon_{13} \\ \varepsilon_{21} & \varepsilon_{22} & \varepsilon_{23} \\ \varepsilon_{31} & \varepsilon_{32} & \varepsilon_{33} \end{bmatrix} \tag{2.9}$$

Any stress vector at any point can be transformed to "principal stress" by setting the non-diagonal components to be zero in the matrix. Any stress vector can be converted to a new coordinate system using the principal stress. For example, if t_i is the stress vector and n_j is the basis vector for the new coordinate system. t_i will be determined by:

$$t_i = \sigma_{ij} n_j = \begin{bmatrix} \sigma_1 & 0 & 0 \\ 0 & \sigma_2 & 0 \\ 0 & 0 & \sigma_3 \end{bmatrix} \begin{bmatrix} n_1{}' \\ n_2{}' \\ n_3{}' \end{bmatrix} \tag{2.10}$$

σ_1, σ_2, σ_3 are the principal stresses along 1, 2 and 3 principal stress directions. The stress invariants can also be determined by using these principal stresses.

$$I_1 = \sigma_1 + \sigma_2 + \sigma_3$$
$$I_2 = -(\sigma_1\sigma_2 + \sigma_2\sigma_3 + \sigma_3\sigma_1) \quad (2.11)$$
$$I_3 = \sigma_1\,\sigma_2\,\sigma_3$$

I_1, I_2, I_3 are the three stress invariant. The detailed description for deriving stress invariant can be found elsewhere[41,42]. Similarly, the strain invariant are given by:

$$I_1' = \varepsilon_1 + \varepsilon_2 + \varepsilon_3$$
$$I_2' = -(\varepsilon_1\varepsilon_2 + \varepsilon_2\varepsilon_3 + \varepsilon_3\varepsilon_1) \quad (2.12)$$
$$I_3' = \varepsilon_1\,\varepsilon_2\,\varepsilon_3$$

ε_1, ε_2, ε_3 are the principal strains along 1, 2, and 3 principal strain directions. In Chapter 6, the stress and strain trace distributions are presented for the analysis of the stress state in Al_2O_3 and TiC_xN_{1-x}.

2.4.2 Elastic Energy Density

The stored elastic strain energy is defined as the amount of work that can be stored in the material with respect to the external loading. It is also the area under the stress strain curve after a specified elongation in the elastic region. It is correlated with the failure criterion of a material and it influences the amount of external work that must be done to initiate failure by a brittle fracture mechanism. The stored elastic energy is calculated in the following way.

$$\mu = \frac{1}{2}\sum \sigma_{ij}\epsilon_{ij} \tag{2.13}$$

In this thesis, elastic energy density will be examined as a function of coating microstructure.

2.5 Hardness of Al_2O_3 and TiC_xN_{1-x} coatings

Hardness is a measure of the resistance to penetration or resistance to indentation when force is applied. The hardness and modulus can be determined using the standard practice for instrumented indentation testing. The definition of hardness is:

$$H = \frac{P_{max}}{A} \tag{2.14}$$

where P_{max} is the maximum load and A is the projected area of the impression made by the indenter. The hardness and Young's modulus of Al_2O_3 and TiN based coatings have been studied using nanoindentation techniques[18,43,44]. It was shown that the coating hardness changes with the texture, where highly (211) oriented TiN films exhibit a lower hardness compared to non-textured coatings. In alumina, $(10\bar{1}2)$ texture was found to exhibit the lowest hardness and modulus. Furthermore, multilayer coatings showed higher hardness and adhesion strength compared to monolayer coatings[45]. It was also shown that smaller grain size of the textured films causes a higher hardness and results in a better wear resistance[18].

2.6 Finite element models (FEM) for structural analysis

2.6.1 Object-oriented finite element (OOF) model

A comprehensive package for mechanical property calculation has been developed and continues to be improved by NIST (National Institute of Standards and Technology, Gaithersburg, MD). The name of this code, object oriented finite element analysis, second version (OOF2), derives from the object oriented programming language in which it is encoded (in this case, Python).

Based on the FEM, OOF is designed to calculate mechanical properties including the stress-strain state of complex microstructures under input boundary conditions. It discretizes the input domain into a set of finite elements with polygonal shapes that represent both the properties and the homogeneity of a corresponding local area. Due to its simplicity, triangles and rectangles are most frequently used element type in two-dimensional finite element analyses. The boundary conditions can be specified as either mechanical or thermal loads. OOF2 has the ability to calculate the stress-strain fields of complicated microstructures having more than several hundred grains. Another advantage of the OOF2 package is that specific materials properties (crystallographic orientations, stiffness, coefficient of thermal expansion, elastic constant, Young's modulus and Poisson's ratio) can be easily incorporated.

2.6.2 Previous Calculations of Thermal Stresses in Coatings Using OOF

The anisotropic characteristics of each material can be accounted for in the calculation of internal stress and strain. In the previous FEM model of Al_2O_3, it was found that textured samples have residual stresses that are lower and the stress distributions that are lower and narrower than in untextured samples[35]. However, the effect of crystallographic orientations and anisotropic characteristics of multilayer coatings have not been modeled. For instance, the Young's modulus and Poisson's ratio were used instead of anisotropic elastic constants (C_{11}, C_{12}, C_{13}, C_{33}, C_{44}) for alumina phase.

There are many papers that use FE modeling for calculating thermoelastic response[46-50]. Only a few papers report on residual stress calculations in coatings with OOF[49-50]. Residual stresses were also predicted for textured alumina. It was found that the thermal stress was 50 MPa for textured sample and 300 MPa for untextured samples. Moreover, textured samples have lower average thermal stress compare to the untextured samples. This information will be applied to the current work since four different Al_2O_3 coating films with variations in texture will be compared.

Hsueh et al.[50] modeled the residual stress in plasma-sprayed thermal barrier coating, where the thermal stress at the interface between two coating layers is simulated. They found high residual stresses up to 1 GPa at the interface regions. The bottom coatings always have higher stress than the top coatings due to its thin layer thickness. In this research work, coatings were studied without the emphasis on substrate effect.

Chapter 3

Microstructural Characterization and Simulation Methods

This chapter describes the methods used to characterize the microstructures and simulation methods used to calculate the thermal stresses in four coated tool inserts. Electron backscatter diffraction mapping (EBSD) has been used to measure the grain size and shapes, the distribution of grain orientations and the grain boundary misorientations of Al_2O_3 and TiC_xN_{1-x}. Nanoindentation was used to measure hardness and atomic force microscopy (AFM) was used to measure the lengths of cracks extending from the nanoindentation marks on Al_2O_3. The object oriented finite element (OOF) program was used to calculate the residual stress. The chapter begins with a description of the sample geometry. This is followed by descriptions of the measurement and simulation techniques used throughout this thesis.

3.1 Sample Geometry

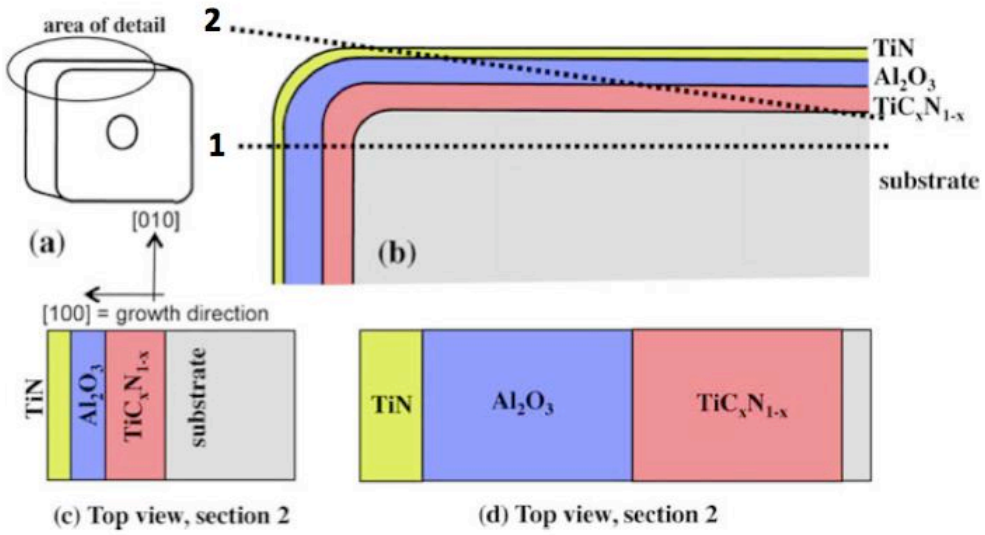

Figure 9. Schematics of the sample preparation method showing a) area of detail, b) two different methods of polishing, c) cross section view of the polishing method 1, and d) cross section view of the polishing method 2

Four tool inserts provided by Kennametal Inc. were ground and polished in two ways to allow both microstructural characterization and hardness measurements (see Fig. 9). The first section plane, labeled 1, creates a cross section of the insert so that each component of the multilayer coating can be observed perpendicular to the [100] growth direction. Each coating layer can be seen with respect to Fig. 9c. Because the coatingsare only few microns wide, to increase the area of interest for the nanoindentation experiment, a-second section plane was created. The section plane, labeled 2 in Fig. 9b, was polished at an approximate angle of 2° with respect to the surface of the coating so that when viewed from the top, extended regions of each layer are visible, as depicted in Fig. 9d. Both sections were prepared by first grinding with abrasives from 200 to 1600 grit size, then by

polishing with 3 μm and 0.5 μm alumina slurries. Note that Fig. 9c and 9d are not drawn to scale. An SEM image of the cross section of the insert is shown in Fig. 10. The reference frame for the image of the cross section, in Fig. 10 is rotate by 90°, with respect to Fig. 9c.

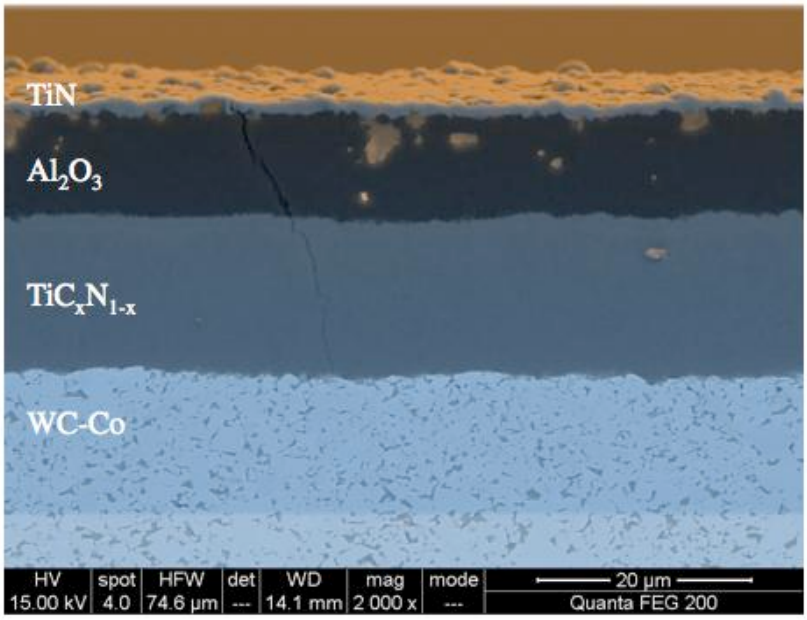

Figure 10. Scanning electron microscope (SEM) image of a sample cross section. Layered structure of the coatings and substrate can be observed. Note that the colors for each coating is artificial.

3.2 Microstructure and Property Characterization Method

3.2.1 Atomic force microscopy (AFM)

A Veeco Thermomicroscopes CP-II was used for all AFM imaging. Sharpened pyramidal Si_3N_4 probes (Thermomicroscopes ML06A-F) were used to obtain contact images. In this thesis, AFM was primarily used to image the cracks created by the indents. The field of view for each AFM image was selected based on the size of indent produced by

the MTS nanoindenter. Each indent has length and width equal to 15 μm. Thus the field of view for each AFM image was set to 25x25 μm^2 to capture the crack length from the nanoindentation experiment. In our experience, the vertical sensitivity of the AFM allows the surface topography in Al_2O_3 to be resolved more clearly than optical microscopy or scanning electron microscopy (SEM). This is particularly important for measuring the lengths of crack, which have widths much smaller than a micron.

3.2.2 Electron Backscatter Diffraction Mapping

In this work, the microstructure and grain orientations of four CVD deposited coatings were determined using two different OIM systems (TexSEM Laboratories, Inc.). One was incorporated in a Phillips XL40 FEG scanning electron microscope (SEM) and the other in a Quanta 200 SEM. These measurements were challenging because of charging. Without a conductive coating, the EBSD patterns were unsatisfactory for indexing. On the other hand, if the coating is too thick, the surface of interest is obscured. The ideal carbon coatings were deposited in a vacuum of $0.7x10^{-1}$ atm from a heated carbon filament. The carbon fiber was preheated with constant power for 1 sec, and then a pulsed signal was applied for 5 sec to deposit the coating.

The samples were tilted to an angle of 60° in the Phillips XL40 system and 70° in the Quanta 200 system with respect to the beam and patterns were recorded using an accelerating voltage of 20 kV. Orientation data were recorded at spatial intervals of 50 nm for samples 1 and 2 and 100 nm for samples 3 and 4. The data were processed and analyzed using OIM software version 5.1. The grain orientation data was processed to remove spurious observations using the 'grain dilation clean-up' procedure in the software.

In this process, the grain tolerance angle was fixed at 5° and the minimum grain size was set at 12 pixels. Finally, the orientations within each grain were averaged so that there was a single orientation per grain. To obtain suitable statistics for the texture analysis, multiple adjacent images were collected along the length of the exposed films and merged for average grain size and orientation calculations. The data sets for the TiC_xN_{1-x} layers were made up of at least 2000 grains. For the alumina layers, the data sets were made up of at least 560 grains. Data sets of this size are sufficient to determine the texture with greater than 90% confidence[51]. The crystallographic orientations of the Al_2O_3 and TiC_xN_{1-x} crystals were obtained by electron backscattered patterns (EBSPs), in the form of Euler angles (φ_1, Φ, φ_2).

3.2.3 Microstructural Analysis

The grain area and shape were analyzed using Image J, a program developed by National Institutes of Health[52]. In this analysis, grains from the OIM maps are fitted to ideal elliptical shapes and the geometric properties of these ellipses are then calculated to determine the average area and the average dimensions of the major and minor axes (see Fig. 11).

(a)

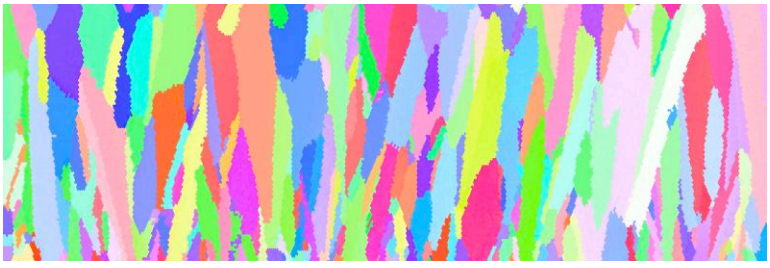

(b)

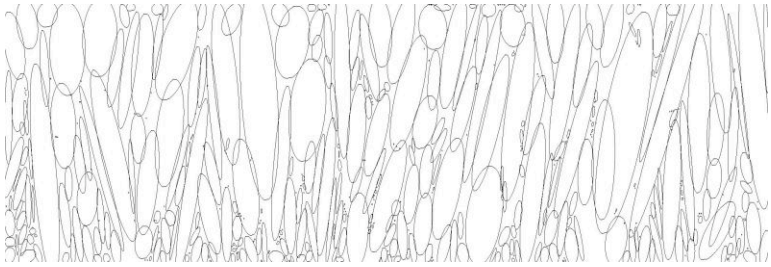

Figure 11. a) Sample OIM image of TiCxN1-x coating. b) Ellipse shaped image produced by ImageJ for grain shape information and grain area calculation.

The average texture and inverse pole figures can be calculated using OIM analysis software. This software was then used to extract more than 5000 boundary line traces from each TiC_xN_{1-x} layer. The grain boundary segments in each sample are classified in the following way. If the misorientation is within Brandon's[53] criterion (8.7°) of the ideal Σ3 misorientation (60° of disorientation about the [111] axis), and the surface trace of the boundary is within 10° of orientation of the coherent twin (both grains terminated by (111) planes), it is classified as a coherent twin. If the misorientation is within Brandon's criterion of the ideal Σ3 misorientation, but the surface trace of the boundary is more than 10° from the orientation of the coherent twin, then it is classified as an incoherent Σ3. If the boundary does not meet the Brandon criterion, it is considered a random boundary. It should be noted that some of the incoherent Σ3s have traces that are coincidentally within the 10° tolerance and will be incorrectly classified as coherent. This leads to a small overestimation of the coherent twin population and an underestimation of the incoherent Σ3 population.

3.2.4 Measurement of mechanical properties

Hardness measurements were made using a nanoindenter XP (MTS systems corporation) equipped with a Berkovich diamond tip. The diamond tip was calibrated using measurements on fused silica. The hardness and modulus were determined using the standard practice for instrumented indentation testing[54]. For all of the measurements, the indenter approach rate was 25 nm/s. Once the indenter contacted the surface, the load on the sample increased to a maximum of 10 mN within the time span of 25 s. The maximum load was then held constant for 10 s. Finally the indenter was withdrawn at twice the loading rate. The maximum depth of indentation was 2 μm. Indentations on coatings invariably probe both the top layer and the underlying layers. In an attempt to assess the influence of the underlayers, samples were polished at a 2° angle with respect to the substrate orientation. When moving laterally across the surface from the substrate to the top most layer, the sequential indents probe progressively thicker layers. At each position, 10–15 indents were made and the values reported are the means and standard deviations of these measurements.

3.3 Numerical models for structural analysis

Object-oriented finite element analysis (OOF) was developed at National Institute of Standards and Technology (NIST, Gaithersburg, MD). As described in Chapter 2, this program is designed to investigate the stress, strain and failure behavior in complex microstructures. The program performs two-dimensional thermo-elastic computations under mechanical and/or thermal loads. In this work, the responses to the combined loads

(mechanical + thermal) were calculated for the real Al_2O_3 and TiC_xN_{1-x} microstructures. Digital grain maps from orientation imaging microscopy (OIM) that were used from the previously described microstructural analysis procedures were used as input. Crystallographic orientations and elastic constants of Al_2O_3 and TiC_xN_{1-x} were incorporated (shown in Table 1) to model the anisotropic materials properties.

OOF2 also provides a way to simulate the effect of cracking. Artificial cracks can be created by modifying the input file and assigning the crack area as an additional material in the system. The "material" that represents the crack must be compliant so it is assigned a modulus that is 0.01% of that of the coating.

3.4 Simulation methods

3.4.1 Simulation Procedure and Input Material Properties

A typical procedure for OOF2 simulation is as follows:

The first step requires the user to input a micrograph. The micrograph could be any virtual image or experimental map from a microscope. To analyze the EBSD image, a grain text file from EBSD measurement is required as input. From the micrograph, specific materials can be associated with colors in the image, or groups of pixels can be selected to associate with a material. Properties can then be applied to the defined materials (e.g. orientations, elastic constants, thermal expansion coefficients, and surface energies).

From here the user can create and modify the finite elements that will represent the micorstructure. The finite elements can be either triangles or rectangles. The shapes of these elements can be modified. The user can now perform a virtual experiment with relevant boundary conditions. The simulation can be carried out under mechanical loads (tensile or compression) and/or thermal loads (quenching or annealing). OOF2 uses a finite element algorithm to approximate the stresses and strains in each element that would result from imposed loads and boundary conditions. The solutions are available as both images and text files.

In OOF2, crystallographic orientations and elastic constants of each phase were incorporated to model the anisotropic materials properties. The crystal orientations of the Al_2O_3 and $TiC_xN_{(1-x)}$ crystals were obtained by electron backscattered patterns in the form of Euler angles (φ_1, Φ, φ_2). Materials properties that are used in OOF simulations are listed in Table 1.

Table 1. Physical Properties of the Materials used for the Simulation (a) ref. [12], (b) ref. [55], (c) ref. [13], (d) ref. [56], (e) ref. [57] at 1100K, (f) refs. [58-59], (g) refs. [60-62]

Material	Young's Modulus (GPa)	Poisson's Ratio	Coefficient of Thermal Expansion ($x10^6$, K^{-1})	Elastic Constants (GPa)
TiN	-	-	9.35[a]	C_{11} = 625 C_{22} = 165 C_{44} = 163 A=0.709[b]
TiC	-	-	7.4[c]	C_{11} = 513 C_{12} = 106 C_{44} = 178 A=0.875[d]
Al_2O_3	-	-	α_{11} = 7.67, α_{33} = 8.52[e]	C_{11} = 497 C_{12} = 163 C_{13} = 116 C_{14} = 22 C_{33} = 501 C_{44} = 147[f]
WC	-	-	α_{11} = 5.2, α_{33} = 7.3[g]	C_{11} = 720 C_{12} = 254 C_{13} = 267 C_{33} = 972 C_{44} = 328[g]
Co	211[g]	0.31[g]	14.0[g]	-
Crack	1	0.11	0	-

3.4.2 Simulation Assumptions and Boundary Conditions

Three different calculations were performed: those to evaluate the misorientation related stresses in the alumina alone, those to evaluate the combined effects of the misorientation related stress in Al_2O_3 and TiC_xN_{1-x} stacked coatings, and those to evaluate the effect of cracking and the substrate related stress. In all cases, the properties in Table I were assigned to the corresponding phase in the model. The domain of the computation included more 10,000 finite elements. Some calculations were performed on the same model, but with finer and coarser levels of discretization. The results indicated that finer discretization did not alter the results.

To calculate the misorientation stresses, the alumina layers alone were cooled 800 K with free boundary conditions, as in reference[8]. Because the properties for TiC_xN_{1-x} are not known, we made the following approximations. Assuming x = 0.5, the CTE was taken as the average of the CTEs of TiC and TiN and the components of the stiffness matrix were also assumed to be averages of the components of each phase.

In the second case where misorientation stresses are evaluated, the macroscopic strain that results from the substrate was estimated and this was applied as a boundary condition on the left and right hand side of the sample[55]. To specify this boundary condition, we used the CTEs of WC and Co to estimate a composite CTE (6.6x10-6/K) and then assumed a -800 K change in temperature. The resulting strain is -0.0053 and half of this amount was applied to the left and right hand sides of the model. With these conditions, the stress and strain were calculated at each point within the microstructure.

In the case where the effect of channel cracks is evaluated, the coatings were supported by a homogeneous substrate. To simulate the shrinking of the substrate, the CTE

of homogeneous WC-Co substrate was assumed to be 0 while the CTE of the Al_2O_3 is estimated to be the difference between the CTE of Al_2O_3 and the CTE of WC-Co (a_{11} = $1.07x10^{-6}$, a_{33} = $1.92x10^{-6}$). The CTE of the TiC_xN_{1-x} was estimated to be the CTE of TiC_xN_{1-x} minus the CTE of WC-Co ($1.775x10^{-6}$). A -800K temperature change is also assumed. A restricted strain of 0 was applied to the left, right, and bottom sides of the model to ensure that the substrate does not move. With these conditions, stress and strain were calculated at each point within the microstructure.

3.4.3 Modification of the input file to create artificial cracks

A computer program was written to modify grain files or .ang files from EBSD measurements to add a crack as an additional phase in the system. The algorithm is:

(1) The user can identify an initial location for the crack and specify the width of the crack.

(2) A random number between 0 and 1 is generated.

(3) If the random number is between 0 and 0.33, the crack moves to the left by 0.1 microns as it advances downward. If the random number is between 0.33 and 0.66, the crack advances downward along the same path. If the random number is between 0.66 and 1, the crack moves to the right by 0.1 microns as it advances downward.

The program also assigns a zero value to all three Euler angles of the WC-Co region as it will be treated as homogeneous substrate. In OOF simulations, the materials properties used for the crack are listed in Table 1.

Chapter 4

Structure of the Coatings

This chapter describes the results of microstructure studies of Al_2O_3 and $TiC_xN_{(1-x)}$ coatings. The size and aspect ratio of the grains in Al_2O_3 and $TiC_xN_{(1-x)}$ were obtained through the EBSD maps. Texture information was obtained through IPFs derived from EBSD maps. Mechanical properties and the residual thermal stress calculations will be discussed in the later chapters.

4.1 Microstructure Findings

4.1.1 Crystal Orientations of TiC_xN_{1-x}

Inverse pole figure maps for the TiC_xN_{1-x} layers are shown in Fig. 12. Note that the growth direction is vertical along [100]. The grain colors correspond to the orientations defined in the key (within Fig 12d). Black areas and areas with speckled contrast at the tops and bottoms of the maps represent areas where patterns were not indexed. With a step size of 50 nm and a minimum grain size of 12 pixels, grains with diameters smaller than 200 nm cannot be detected, so the fine grained transition regions at the tops and bottoms appear black or as discrete speckled orientations. Within the bulk of the films, the grains are columnar in shape and are aligned along the growth axis.

Inverse pole figures for the TiC_xN_{1-x} layers are shown in Fig. 13. These figures are drawn with respect to the growth direction, [100]. Therefore, they show the relative

frequency of crystal plane normals that are parallel to the growth direction, in multiples of a random distribution (MRD) units. Samples 1 and 2 have textures that are relatively weak and all of the peaks indicate a preference for orientations that are perpendicular to the [111] direction, along the arc of the great circle that connects [112] to [101]. Sample 4 has the strongest texture with 3.51 MRD. In samples 1 and 2, there is a nearly continuous distribution along this arc. The texture in sample 3 is referred to as [111] and the texture in sample 4 is referred to as [101]. For simplicity, the textures in sample 1 and 2 are referred to as [112], the position of the maximum, even though there is actually a range of preferred orientations.

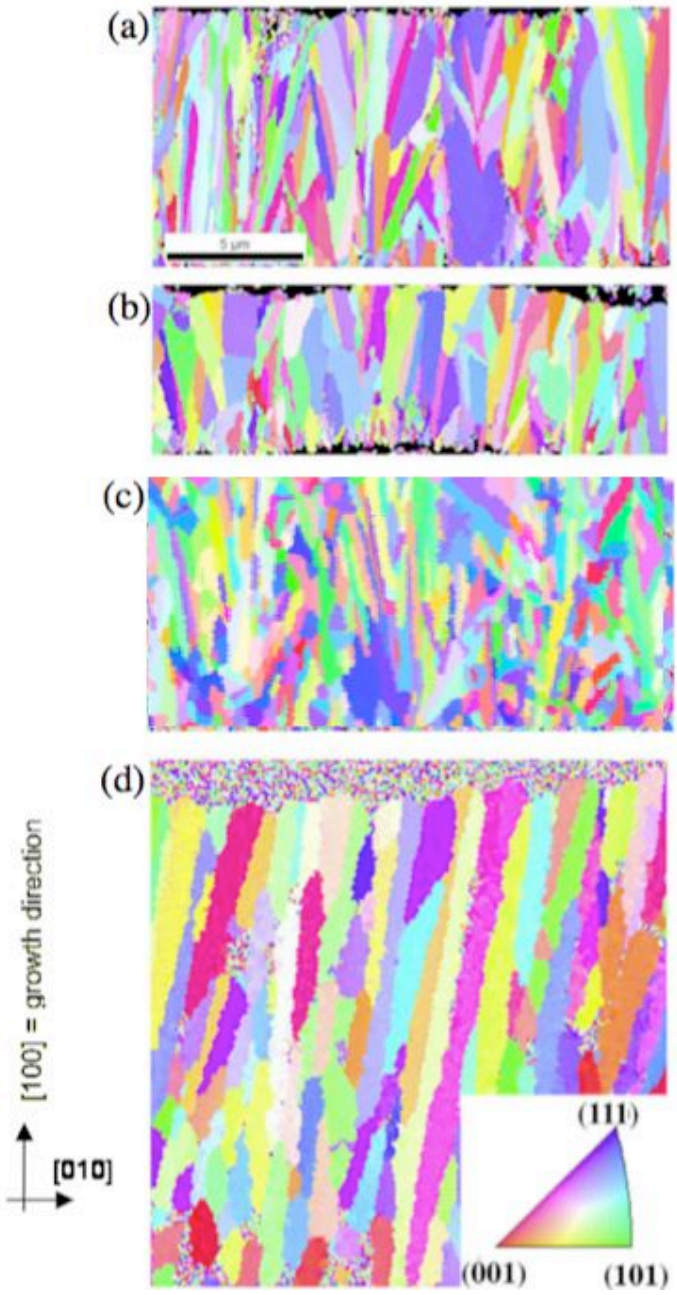

Figure 12. Inverse pole figure maps for the TiC_xN_{1-x} layers in (a) sample 1, (b) sample 2, (c) sample 3, and (d) sample 4. Each color corresponds to a crystal orientation, defined in the key in (d). The 5 μm scalebar in (a) is the same in all four maps.

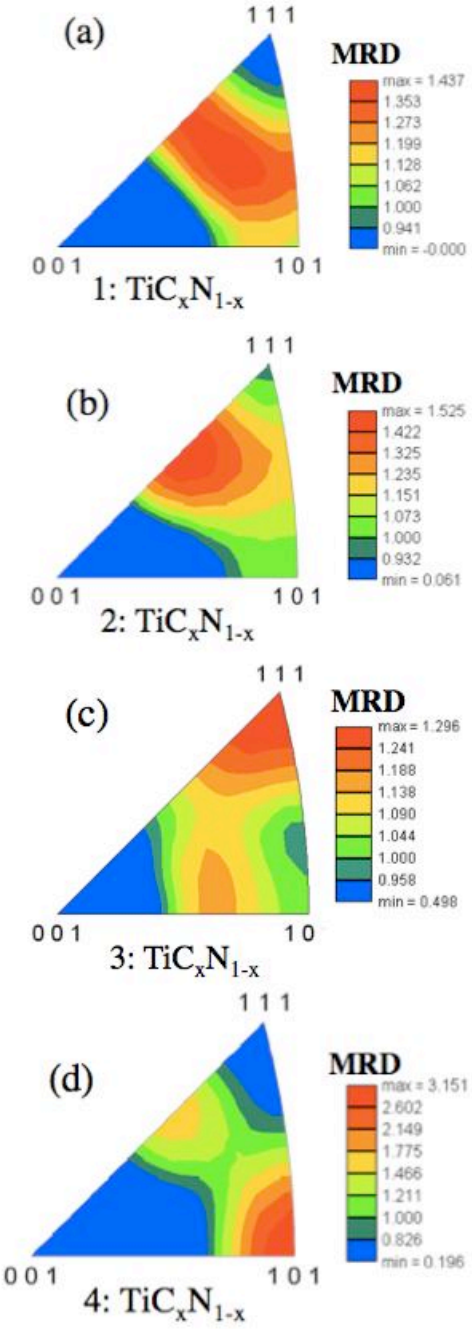

Figure 13. Inverse pole figures for the TiC_xN_{1-x} layers (a) sample 1, (b) sample 2, (c) sample 3, and (d) sample 4 with [100] (the growth direction) as the reference.

4.1.2 Crystal Orientations of Al_2O_3

Inverse pole figure maps for the α-Al_2O_3 layers are shown in Fig. 14. Once again, the grains are columnar in shape and are aligned along the growth axis. The aspect ratios of these grains are smaller than those in the TiC_xN_{1-x} layer. Sample 1 has the highest aspect ratio (~7) and Sample 3 has the lowest (~4). However, it should be noted that the minor elliptical axis is essentially the same in samples 1 and 2; the greater aspect ratio of the grains in sample 1 derives from the fact that the coating is thicker and, therefore, the average major elliptical axis is longer. The grains in sample 1 appear to be the most columnar and have higher aspect ratios, while those in sample 2 are the most equiaxed. The one common feature among these coatings is the apparent texture. Based on the grain coloring, there is an obvious preference for prismatic grain orientations in samples 1,2, and 4.

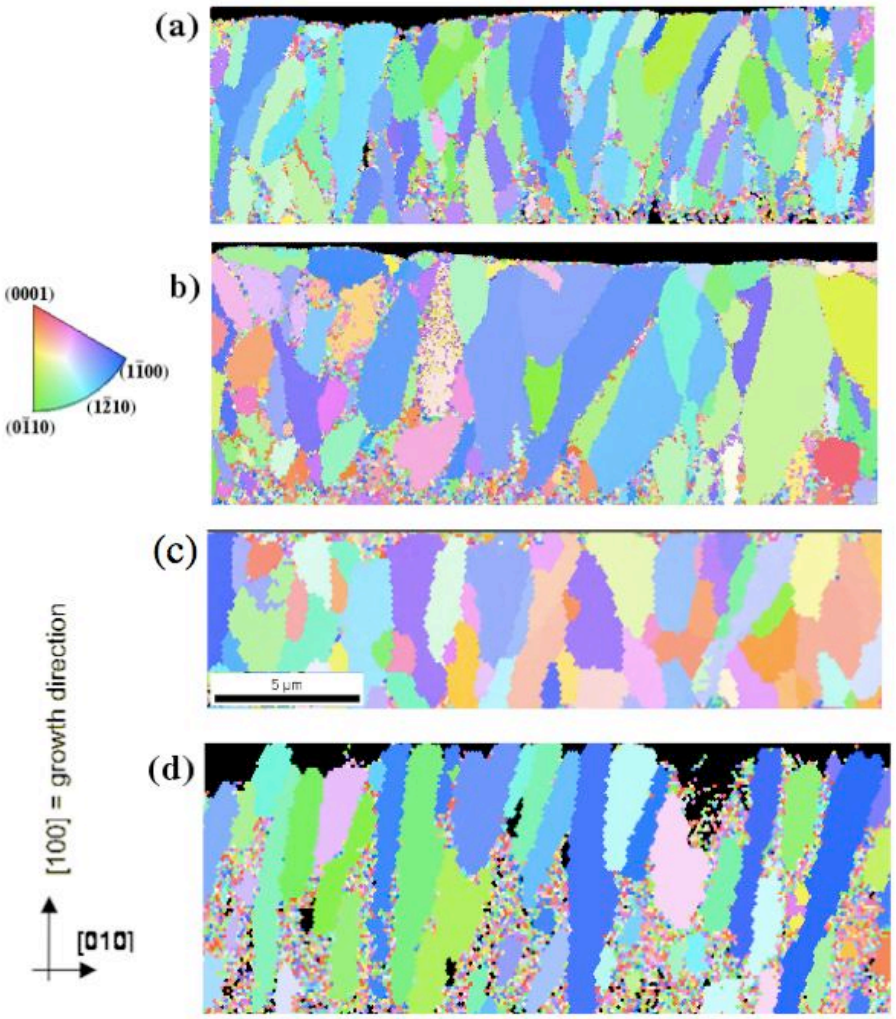

Figure 14. Inverse pole figure maps for the Al_2O_3 layers in (a) sample 1, (b) sample 2, (c) sample 3, and (d) sample 4. Each color corresponds to a crystal orientation on the left. The scale in (c) is the same in all four maps.

The inverse pole figures for the alumina layers in Fig. 15 show relatively strong textures. Once again, these figures are plotted with reference to the growth direction and indicate that the [0001] crystal axis is approximately aligned with the growth direction. For samples 1 and 2, the peak of the distribution is actually inclined with respect to [0001] and is more accurately described as [10$\bar{1}$4]. X-ray diffraction measurements of sample 1 were consistent with this assignment (although it should be mentioned that the angle

between [0001] and [10$\bar{1}$4] is approximately 5°). On the other hand, for samples 3 and 4, the preferred orientation is [10$\bar{1}$2] and [0001]. Furthermore, it should be noted that the intensity of texture differs in the different specimens. Sample 1 has the strongest texture, sample 2 has the weakest texture, and samples 3 and 4 have intermediate values.

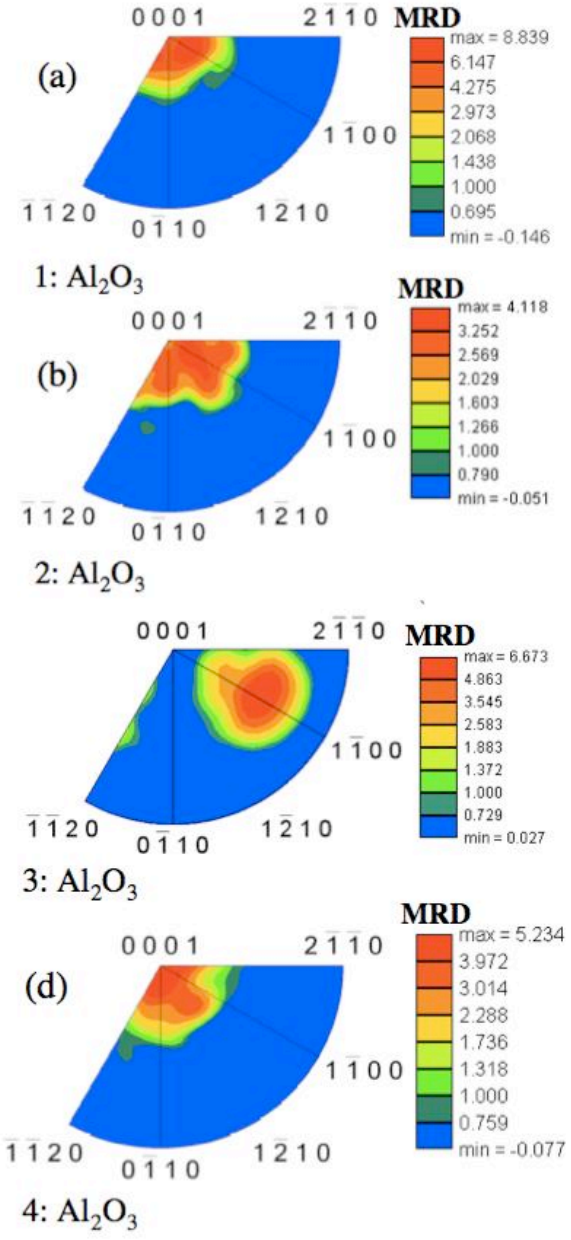

Figure 15. Inverse pole figures for the Al_2O_3 layers (a) sample 1, (b) sample 2, (c) sample 3, and (d) sample 4 with [100] (the growth direction) as the reference.

4.1.3 Twin Structures in TiC_xN_{1-x}

The greatest number of line segments (22,420) were extracted from sample 1 and these were used to calculate the grain boundary plane distribution for the Σ3 misorientation using a procedure described previously[65]. It should be noted that while the data set is not extensive enough to determine the grain boundary plane distribution at all misorientations, there are more than 3400 traces from Σ3 grain boundaries so the plane distribution at this particular misorientation is reliable.

Inspection of the misorientation distribution function for the TiC_xN_{1-x} coatings (shown in Fig. 16) revealed a strong peak for the misorientation of 60° about the [111] axis. In coincident site lattice notation, this is a Σ3 grain boundary. In the case that both planes on either side of the grain boundary are (111), this is a coherent twin. The image in Fig. 17a shows the microstructure of sample 1 (these are the same data as in Fig. 12a), where the contrast corresponds to the image quality associated with the EBSD patterns. Therefore, there is relatively lighter contrast within the grains and darker contrast at the grain boundaries. Those grain boundaries that have a Σ3 misorientation are marked by red lines. More often than not, these lines are straight. 28% of all the grain boundary length is of the Σ3 type and that 20% of all grain boundary length has both the Σ3 misorientation and has trace orientations that are consistent with the coherent twin. This is reflected in the distribution of grain boundary planes illustrated in Fig. 17b. The peak at the (111) position (of 700 MRD) shows that there are many more twins than one would expect if grain boundaries occurred randomly. The twin content, as a fraction of grain boundary length, is

higher in sample 1 than in the other samples. The twin population in each of the samples was analyzed and the results are summarized in Table 2. Grain size, shape data, and hardness are included in the section 5.1

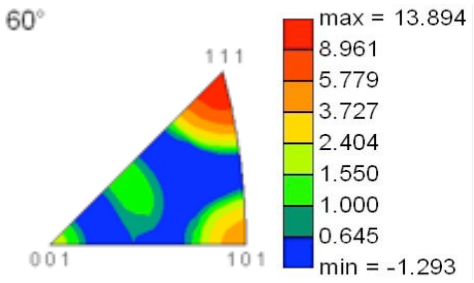

Figure 16. Misorientation distribution function for the TiC_xN_{1-x} coatings with misorientation of 60° about the [111] axis.

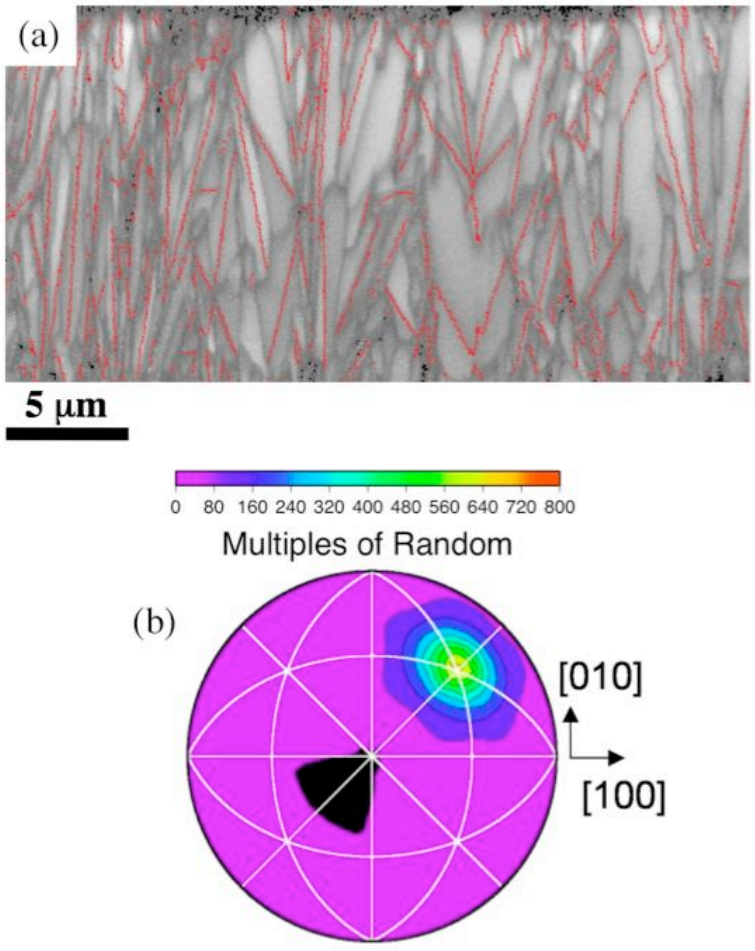

Figure 17. (a) Image quality map of the TiC_xN_{1-x} layer in sample 1. Dark contrast corresponds to poor image quality that is characteristic of patterns recorded at grain boundaries. The red lines denote Σ3 type grain boundaries. (b) The distribution of grain boundary planes for the Σ3 grain boundaries. The distribution is plotted on a stereographic projection. The peak is at the position of the misorientation axis, [111], indicates a high fraction of pure twist grain boundaries with (111) planes on either side of the boundary. This geometry corresponds to the coherent twin

Table 2. Twin Populations in TiC_xN_{1-x} coatings

	Number Statistics, %			Length Statistics, %		
sample	Non-Σ3	Σ3	twins	Non- Σ3	Σ3	twins
1	84	15	6	72	28	20
2	86	14	7	75	25	19
3	84	16	7	80	20	13
4	83	16	5	77	23	13

The coatings examined in this work have a range of microstructural characteristics and this variability makes it possible to test ideas about the links between coating structure and coating properties. One interesting feature of the microstructure of the TiC_xN_{1-x} layers is the high density of twins. This observation is consistent with the TEM results reported earlier[7]. The scope of the current measurements allows us to quantify the twin content of different films. This analysis reveals an inverse correlation between the fractional length of the twins and the strength of the texture; the strength of the texture is highest in sample 4, which also has the fewest twins. Twins tend to randomize the texture because if one grain takes the preferred orientation, the twinned grain is necessarily misoriented by 60°.

There is an interesting relationship between the twinning and the spreading of the preferred orientations along the [111] zone. Because most of the twin boundaries are parallel to the growth direction, and these boundaries have (111) orientations in the crystal reference frame, the adjoining crystal orientations with respect to the growth direction must be perpendicular to [111], which places them in the [111] zone. This

suggests a reason for the spreading of orientations along the [111] zone, especially in samples 1 and 2. It also suggests that the crystals must originally nucleate with orientations in the [111] zone, such as [101] or [112], and that twins grow from these nuclei.

4.2 X-Ray Diffraction

XRD theta-2theta patterns are presented in Fig. 18. The results show a superposition for patterns from the Al_2O_3 layer and the capping TiN layer. In Fig. 18, all the peaks that are labeled blue are Al_2O_3, whereas the peaks labeled in red are TiN. The three unindexed peaks could be TiC_xN_{1-x} and they are not of interest because TiC_xN_{1-x} was found to have weak or no texture in the studies of EBSD. For now, all the peaks that are indexed for Al_2O_3 for the trigonal systems. The intensity of the (104) or $(10\bar{1}4)$ peak in sample 1 is significantly higher than other samples, which corresponds to the findings from the EBSD maps. Samples 2 and 4 have the highest (012) or $(01\bar{1}2)$ and (024) or $(02\bar{2}4)$ peaks, which does not correspond to the IPFs in section 4.1.2. The difference in texture could be because the EBSD maps were obtained from a specific region although the number of grains collected for analysis was up to 2500 for sample 2. Also the X-ray diffraction pattern was obtained by scanning the outer layers of the sample, meaning that it depends on the thickness of the capping TiN coating for each sample, which could vary and influence the intensities of the underlying alumina peaks. Although there are a number of issues that affect these intensities, the ratios of the intensities should be a good measure of the texture. There are no basal reflections in these patterns.

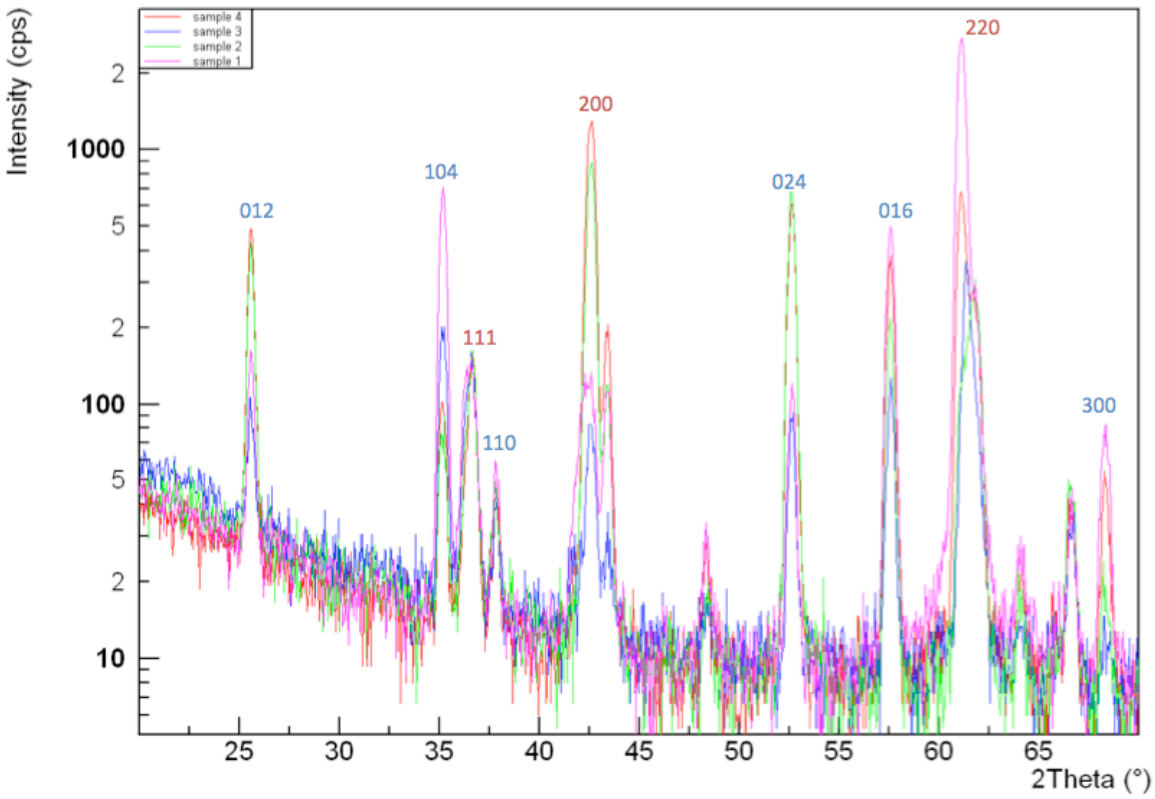

Figure 18. XRD diffraction pattern of the experimental coatings for sample 1 (purple), sample 2 (green), sample 3 (blue), sample 4 (red). The Al_2O_3 peaks are labeled in blue and the TiN peaks are labeled in red.

4.3 Residual Stress and Texture

A second microstructural characteristic that can influence hardness is the texture. For example, the effective elastic modulus is different along different directions. If the material is textured with soft or stiff directions perpendicular the growth surface, the hardness of the film will be influenced. For materials with anisotropic thermal expansion, such as alumina, thermal stresses are sensitive to the texture and such stresses can also influence the hardness of coatings. In general, increased texture leads to a reduction in the level of

thermal stresses[26,50]. Therefore, both the strength of the texture and the orientation are potentially important parameters. In the data presented here, there is no apparent correlation between the strength of the texture and the hardness. Instead, the notable trend appears to be with the type of texture. For the TiC_xN_{1-x} layer, the softest layer is the one exhibiting [101] texture and the harder ones have [112] textures. For the alumina layers, the two layers with $[10\bar{1}4]$ texture are harder than the other two. It is noteworthy that in previous work, this was the texture that was found to exhibit superior wear resistance[7].

Finally, it is worth commenting on the possible role of twins in the microstructure. Twin grain boundaries have compact atomic structures and very low energies. Therefore, they are expected to resist grain boundary fracture more than general boundaries and this may lead to higher hardness. While once again there is no distinct trend, the hardest TiC_xN_{1-x} layer has the highest twin density and the softest TiC_xN_{1-x} layer has the lowest twin density. Therefore, it is possible that the twins make a positive contribution to the coating hardness. If so, there is an interesting parallel with FCC structured metals and alloys where it has been demonstrated that higher densities of twins leads to improved resistance to corrosion and mechanical damage[11].

4.4 Summary

The microstructures of four CVD deposited coatings have been comprehensively characterized. The TiC_xN_{1-x} layers are highly twinned, with coherent twins making up 13%–20% of the grain boundary length. The alumina layers have $[10\bar{1}4]$, $[10\bar{1}2]$ or [0001]

textures that are 4.2–8.8 times random. The TiC_xN_{1-x} layers have weak texture except for sample 4, where as the [101] texture is 3.1 times random.

Chapter 5

Hardness and Cracking

This chapter describes the results of hardness measurements across coatings. The indentation marks were characterized by AFM. Cracks were observed to originate at the corners of the indentation and their lengths were measured. Furthermore, channel cracks on cross sections were manually counted to calculate the average crack spacing for each sample.

5.1 Hardness

Hardness measurements were conducted on samples polished at a 2° angle, as illustrated in Fig. 7d, and the results are shown in Fig. 19. The image at the top of the figure is a montage of optical micrographs of sample 1, recorded after the hardness measurements. Each phase in the coating has a distinct appearance and the location of the indent confirms the origin of the hardness data. Here we will attempt to interpret only the data from the TiC_xN_{1-x} layer (positions 4, 5, and 6) and the Al_2O_3 layer (positions 8, 9 and 10). The values at each of these two sets of positions were averaged to determine the mean values of hardness reported in the final column of Table 3. With few exceptions, mean hardness values from comparable positions on different coatings do not differ by more

than a standard deviation. However, there are clear trends in the mean values that appear to be significant. For example, the hardness values for the alumina layer of sample 1 are always larger than those of samples 3 and 4.

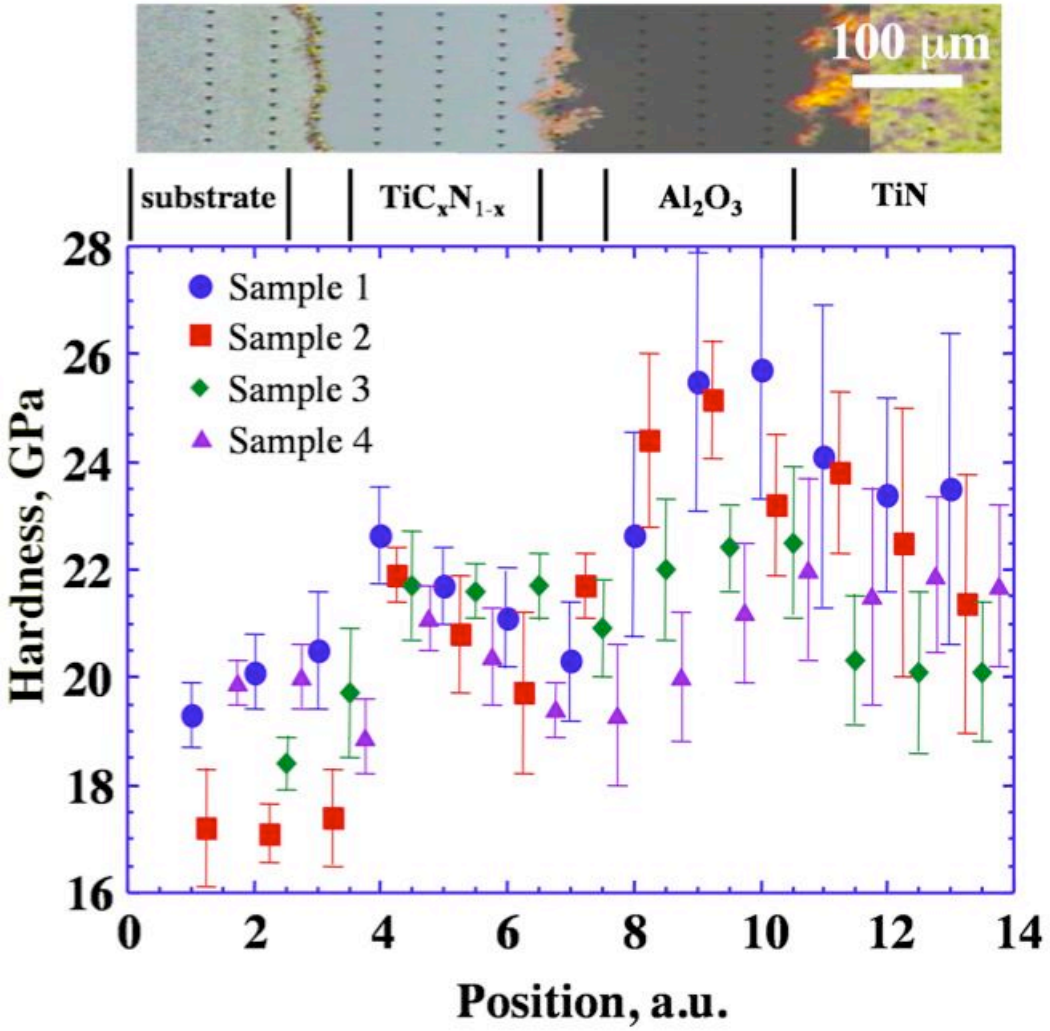

Figure 19. Measured hardness values across section 2 as a function of position (see Fig. 1d) for sample 1 (circles), sample 2 (squares), sample 3 (diamonds), and sample 4 (triangles). Each data set is offset along the x-axis by 0.25 to minimize overlap of the data. The symbols represent mean values and the bars show ± one standard deviation. Above the graph is a montage of optical micrographs showing the location of the indents in sample 1. The vertical rows of black spots are the multiple indents used to determine the mean and standard deviation of the hardness and the different regions are labeled.

Table 3. Summary of microstructural characteristics and hardness for coatings.

Layer	Sample	Grains	Grain area, μm^2	Major axis, μm	Minor axis, μm	Texture, orientation/ MRD	Mean hardness, GPa
TiC_xN_{1-x}	1	5538	2.1	4.85	0.67	{112} 1.4	21.8 (0.8)
	2	1112	1.6	3.46	0.69	{112} 1.5	20.8 (0.7)
	3	2611	1.13	2.59	0.62	{112} 1.3	21.7 (0.7)
	4	2050	3.34	5.03	0.79	{101} 3.1	20.3 (0.7)
Al_2O_3	1	950	2.05	3.08	0.84	{10-14} 8.8	24.6 (2.2)
	2	2567	3.9	3.36	1.36	{10-14} 4.2	24.2 (1.3)
	3	801	1.96	2.60	0.96	{10-12} 3.39	22.3 (1.2)
	4	568	3.89	4.34	1.07	{0001} 5.2	21.1 (1.4)

5.2 Cracking

Figure 20 shows two AFM error images that were taken on indent marks on Al_2O_3. Error images are also called deflection images which are the difference between the tip's actual deflection and the set point deflection. Black contrast corresponds to deflection below the set point (a negative slope on the surface), white contrast corresponds to deflection greater than the set point (a positive slope on the surface), and gray contrast corresponds to the set point deflection (a flat surface). The deflection image is valuable for this study because it simultaneously reveals large topographic features (the indent) and

small features (cracks). Differential polishing of the alumina during preparation of the sample reveals some of the grain boundaries. The cracks, highlighted by red lines, appear as sharp changes in contrast. The indent on the image results from the hardness measurement. Cracks are usually observed to extend from the triangular corner of the indent marks. Because the cracks vary in length, 15 images were taken on each indent mark for all four samples and the values reported in Table 4 are the means and standard deviations of these measurements. Because all the coatings exhibit vertical cracks that form on cooling to relieve thermal stress, it is worth noting here that only the cracks that extend out from the triangular indents are recorded. Thermal cracks that pre-exist in the coatings are not included in the crack length measurement.

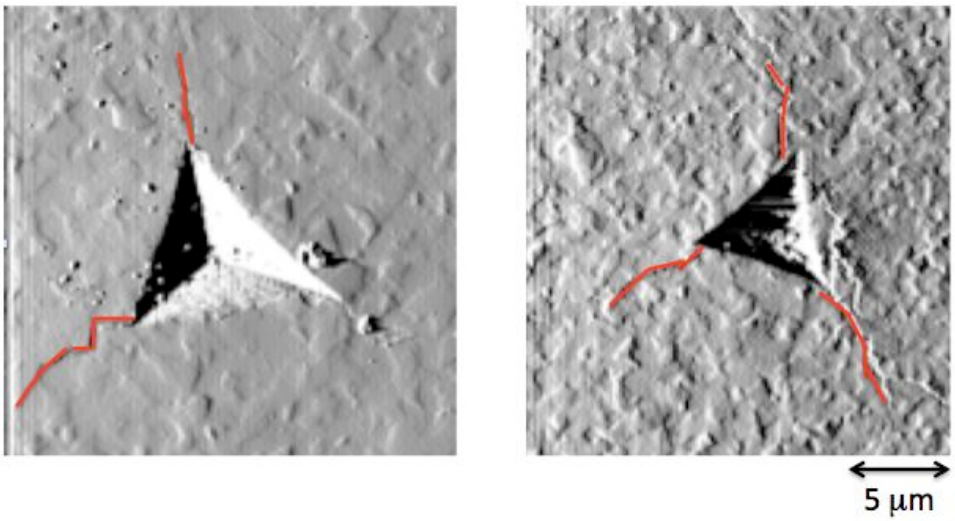

Figure 20. Atomic Force Microscopy deflection images of cracks that extend from the nanoindentation marks. Cracks are highlighted by the red lines.

Table 4. Average crack length and average hardness (Fig 9) of Al_2O_3 for the 4 samples.

	Average Crack Length (μm)	Average Hardness (GPa)
Sample 1	4.27 (1.51)	24.6 (2.2)
Sample 2	4.67 (1.60)	24.2 (1.3)
Sample 3	5.42 (2.31)	22.3 (1.2)
Sample 4	7.33 (2.43)	21.1 (1.4)

The number of cracks along the sample length and width were counted manually for each sample (shown in Fig. 21 and Fig. 22). The results are reported in Table 5. Note that only the cracks that went through both TiC_xN_{1-x} and Al_2O_3 are counted. In later sections describing the thermal stress calculation, the width of the simulations will be based on the average crack spacing calculated by the width of the sample (fixed) divided by the number of crack counted along sample width.

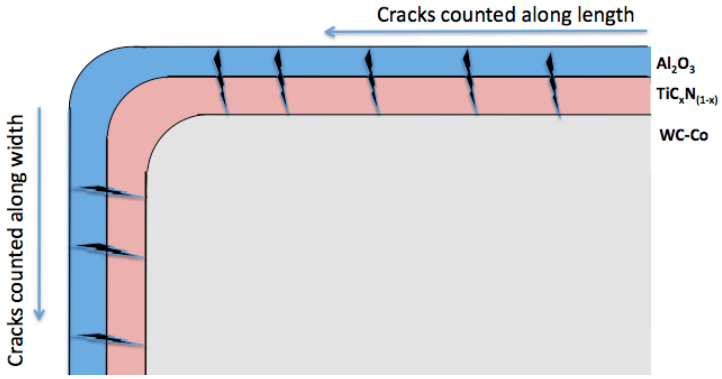

Figure 21. Schematics of cracks counted along sample length and sample width.

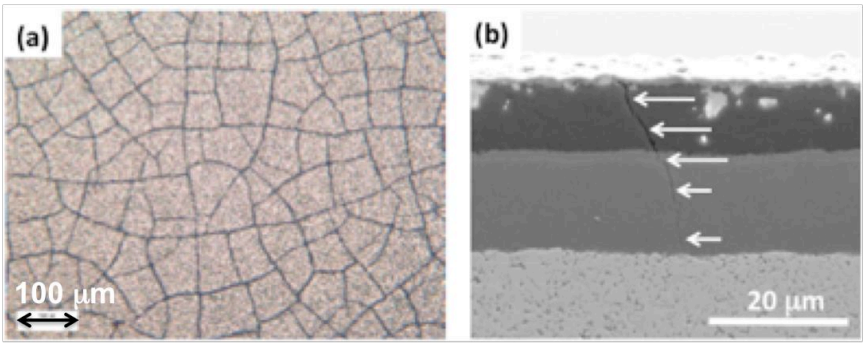

Figure 22. Images of the channel cracks in CVD deposited coatings. (a) plan view optical image of the pattern of cracks. (b) SEM image of a transverse section of a coating. The position of the crack is highlighted by the arrows.

Table 5. Number of cracks counted manually along the sample width and length.

Sample	Number of crack along width	Number of crack along length	Average crack spacing along width(μm)	Average crack spacing along length (μm)
1	50	117	84	143
2	79	197	53	85
3	49	89	86	188
4	67	187	63	89

5.3 Fracture Toughness

The geometric and mechanical characteristics of the coatings are listed in Table 2. The hardness and modulus were determined from the previously reported indentation data in Table 6. The calculated values of the fracture toughness are consistent with measurements of bulk materials, for which values vary between 2 GPa•$m^{1/2}$ (for single crystals) to close to 7 GPa•$m^{1/2}$ (for some ceramic samples)[67]. In the present case, the measurements may be influenced by the thickness of the layers. For example, the modulus of the alumina layer is the smallest in coating 4, which is also the thinnest and may, therefore, be influenced the most by the underlying layers.

Table 6. Summary of Measured Properties of the Coatings. Values in parentheses are standard deviations of measured quantities.

		Sample 1	Sample 2	Sample 3	Sample 4
Coating	Average channel crack spacing, μm	129	81	131	96
TiC_xN_{1-x}	Thickness, μm	18.2	6.8	15	5.82
	Modulus, GPa	497 (33)	467 (18)	486 (24)	463 (27)
	Hardness, GPa	21.8 (0.8)	20.8 (1.0)	21.7 (0.7)	20.3 (0.7)
a-Al_2O_3	Thickness, μm	11.8	9.2	9.9	1.3
	Modulus, GPa	521 (39)	486 (25)	428 (20)	412 (20)
	Hardness, GPa	24.6 (2.2)	24.2 (1.3)	22.3 (1.2)	21.1 (1.4)
	Indenter Crack Length, μm	4.3 (1.5)	4.7 (1.6)	5.4 (2.3)	7.3 (2.4)
	Fracture toughness, GPa $m^{1/2}$	7.5 (1.6)	6.2 (0.9)	4.6 (0.3)	2.8 (0.5)

5.4 Correlation between Microstructure and Hardness

One issue in evaluating the hardness of the different layers is that the underlying substrate and other layers necessarily influence the measurement. In the measurements presented in Fig. 19, the coating has a different thickness at each location. For example, at position 4, the TiC_xN_{1-x} layer is the thinnest and will be most strongly influenced by the substrate. At position 6, on the other hand, the layer is the thickest and the least influenced by the substrate. In all cases, the substrate has a lower hardness than the TiC_xN_{1-x}, so it is interesting that the hardness rises to its highest value when the layer is thin and decreases as the TiC_xN_{1-x} layer gets thicker at positions 5 and 6. A plausible reason for this is that the grains in the thinner region are smaller than those in the thicker region and, therefore, the film is harder. The grains are obviously smaller along the major elliptical axis, because part of the coating has been removed. They are also smaller along the minor elliptical axis because the grains are smaller in the nucleation layer and generally become wider as the film gets thicker (see Fig. 19). To test this idea, Fig. 23 shows the microstructure of the TiC_xN_{1-x} layer of sample 1 that is divided into three layers of equal thickness and ellipses were fit to the grain in each of these sub layers.

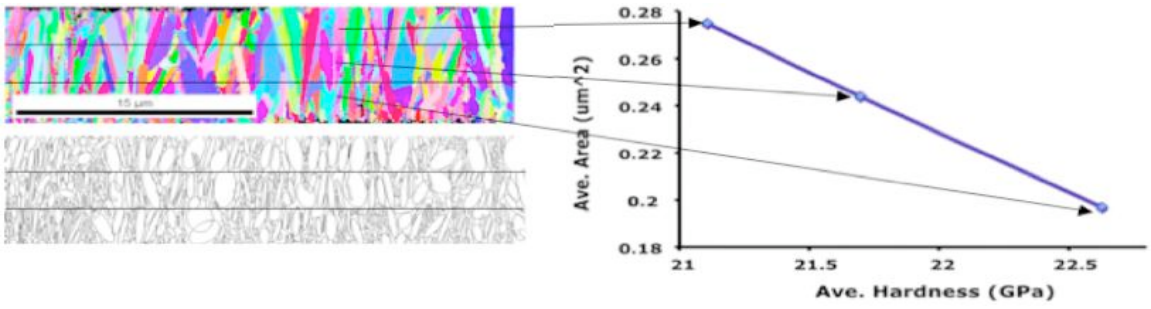

Figure 23. Average area of the three divided regions in TiC_xN_{1-x} layer versus the average hardness of position 4, 5, 6 in Fig. 19.

For the portion closest to the substrate, where the hardness is the highest (22.6 GPa), the average grain area was 0.2 μm^2. For the middle region it was 0.24 μm^2 and for the region furthest from the substrate, where the hardness was the lowest (21.1 GPa), it was 0.27 μm^2. The hardness tends to increase with thickness in the alumina layer (positions 8 through 10 in Fig. 19), as one would expect for a hard layer on a relatively softer layer. Note that the stress state of the film is changed when the material is removed and this may affect the hardness result.

One of the microstructural characteristics that can be expected to influence the hardness of the coatings is the grain size, by the well-known Hall-Petch effect. Because these coatings are columnar, the average length of the major elliptical axis is principally determined by the thickness of the coating. As there is no obvious relationship between the thickness of the film and its hardness, we assume that it is the dimension of the minor elliptical axis that is important. For the TiC_xN_{1-x} layer, the coating with the largest minor axis (4) does have the lowest mean hardness. However, the coating with the smallest average minor axis (3) has a hardness comparable to sample 1, which has a somewhat larger grain size. It should be noted that the variation in the TiC_xN_{1-x} hardness among the coatings is not as great as the thickness dependence within a single coating. For the alumina layer, the differences in the hardness of the coatings are more significant. Once again, the hardest coating has the smallest grain size, but only three of the four observations follow the expected correlation between grain size and hardness (shown in Table 5). As all four samples have different coating thickness, the stress state for each indent is different during the hardness measurement. Typically, thicker coatings have less

residual stress that give rise to high hardness. However, it was found that the sensitivity of the hardness to grain size is not significantly different from the uncertainty over the range of grain sizes explored. These observations suggest that there are factors other than the grain size that are influencing the hardness of these coatings.

5.5 Correlation Between Indenter Crack Length and Hardness

Other than microstructure parameters and texture, cracks in the coatings will influence the thermal stress. Two different kinds of cracks are discussed in this thesis, one is the crack that relieves the internal thermal stress (channel cracks), and the other one is the crack formed by the indentation measurement (indentation cracks). Here we are comparing the hardness and the lengths of cracks produced by indentation.

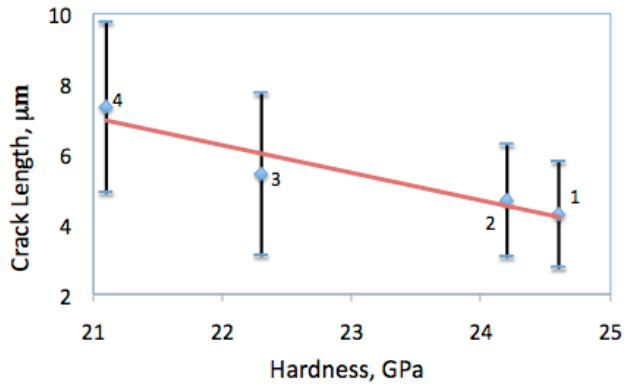

Figure 24. Average crack length for each sample versus the average hardness for each sample.

Figure 24 shows the plot of the average crack length versus hardness for all 4 samples. Here, the linear relationship shows the hardness in each material is inversely

proportional to the crack length it induced. Harder material, like sample 1, produces shorter cracks when indented.

More cracks in the sample means more thermal stress relieved in the sample and the average crack spacing is small. From Table 6, crack spacing and the hardness are not correlated. This is because the effect of thermal stress on crack spacing is also correlated to the coating thickness. In thicker coatings, fewer cracks are required to relieve the same amount of thermal stress. From Table 5 in Chapter 5.3, Samples 2 and 4 have the most channel cracks along the width and length, so the average crack spacings are smaller in comparison to samples 1 and 3.

5.6 Summary

The hardest coatings consist of highly twinned TiC_xN_{1-x} layers with weak [112] texture and α-Al_2O_3 with strong $[10\bar{1}4]$ texture. Al_2O_3 is harder than TiC_xN_{1-x} and the differences in the hardnesses of Al_2O_3 coatings are more significant. Hardness is not correlated to the grain size from the range of grain sizes explored. There is no obvious relationship between the thickness of the film and its hardness. However, there is a linear relationship between the hardness in each material and the crack length induced by the indentation crack. Harder material produces shorter cracks and it has higher fracture toughness.

Chapter 6

Residual stresses

This chapter describes the thermal stress calculations of Al_2O_3 and TiC_xN_{1-x}. The residual thermal stresses were obtained through the finite element method (FEM). EBSD maps have been used as input files for the residual thermal stress calculations. Furthermore, the original input files for OOF were modified to include a crack in the coating and the dimensions of the model were adjusted to reproduce the measured average crack spacing.

6.1 Effect of misorientation related stresses in the alumina with free boundary conditions.

Plots of the stored elastic energy for alumina coatings in each sample are shown in Fig. 25. The calculation simulates a temperature change of -800 °C with free boundary conditions. These maps provide visual comparison of the results while the histograms in Fig. 26 provide a more quantitative description of the elastic energy and stresses in the material. The visual impression from Fig. 26 is that samples 1 and 4 have more elements with low elastic energy than samples 2 and 3 and fewer elements with high elastic energy. This is verified by the histogram in Fig. 26(a). The stresses in these samples (shown in Fig. 26(b)) are both tensile and compressive and mostly lie in the range of ± 100 MPa. Note that the distribution of thermal stresses in samples 1 and 4 is narrower than in samples 2 and 3.

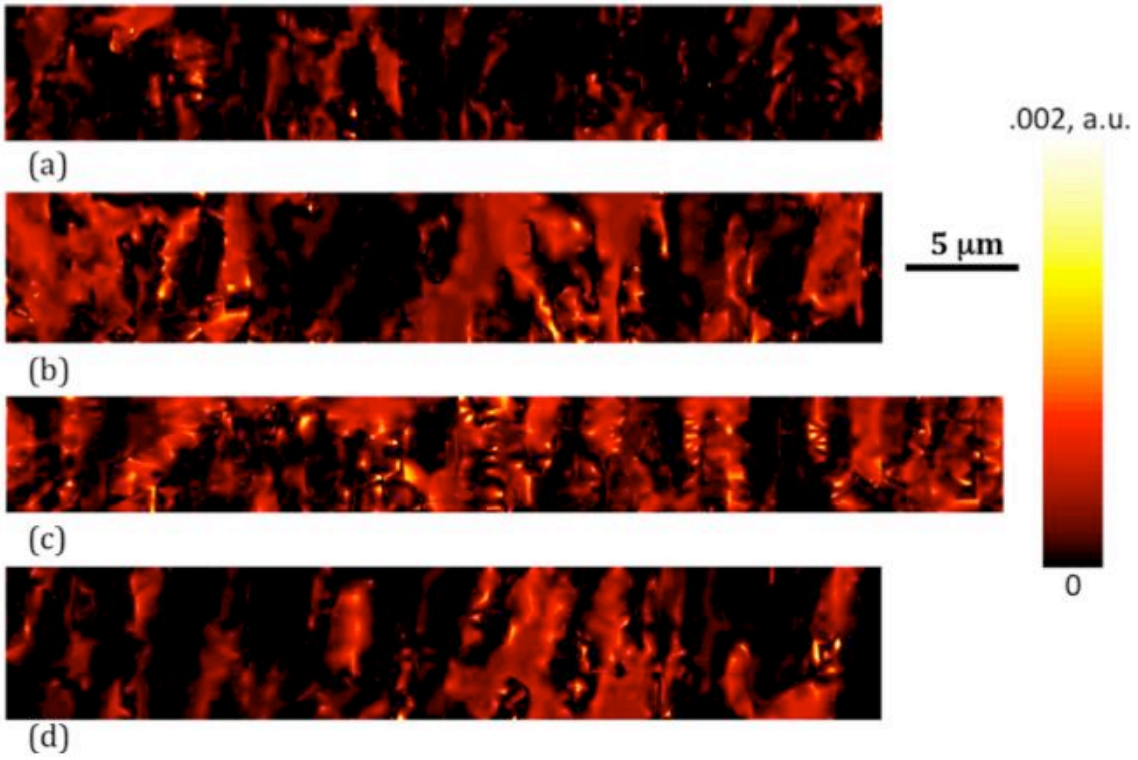

Figure 25. The stored elastic energy distributions for the four alumina layers computed for ΔT = -800 K and free boundary conditions. The intensity (relative) is indicated by the shading of the figure. (a), (b), (c), and (d) are for sample 1, 2, 3, and 4, respectively.

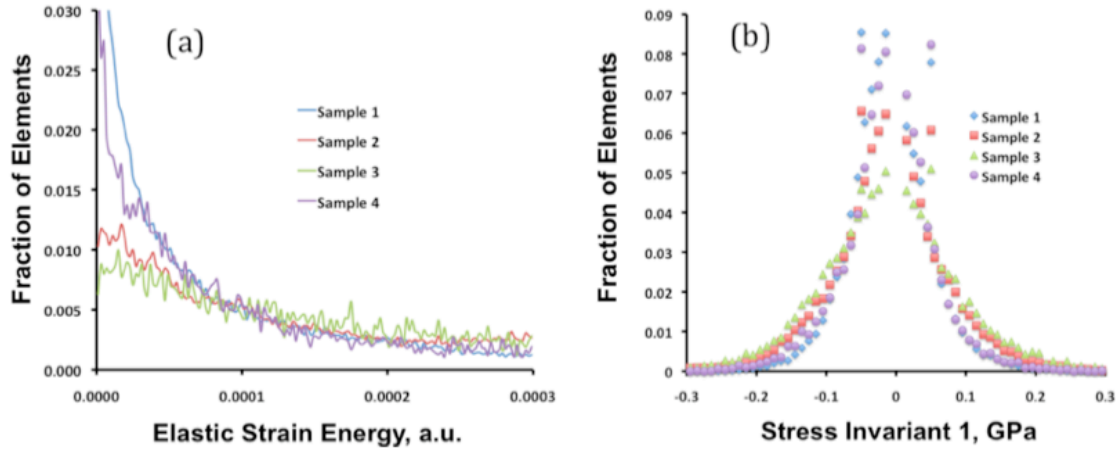

Figure 26. (a) Histogram of the values of the elastic energy in each element for the four alumina layers computed with free boundary conditions and ΔT = -800 K. (b) Histogram of the values of the stress invariant 1 (trace of the stress tensor) in each element.

The calculations demonstrate that texture has two important and potentially beneficial impacts on the thermal stresses. First, because alumina has uniaxial symmetry, the alignment of the [0001] axes reduces the misorientation stresses. This is illustrated in Figs. 25 and 26. The samples with the strongest (0001) texture (1 and 4) have a narrower distribution of misorientation stresses than samples 2 and 3. Furthermore, sample 3, with $(10\bar{1}0)$ texture, has the highest stresses. While the strength of the texture is about the same as sample 2, the texture does not promote alignment of the unique [0001] axis and, as a result, is not as effective in reducing the misorientation stresses. The results are similar to the findings by Vedula et al[35], where textured samples have lower stresses and the stress distributions were narrower.

6.2 Elastic Energies and Strains in Al_2O_3 and $TiC_xN_{(1-x)}$

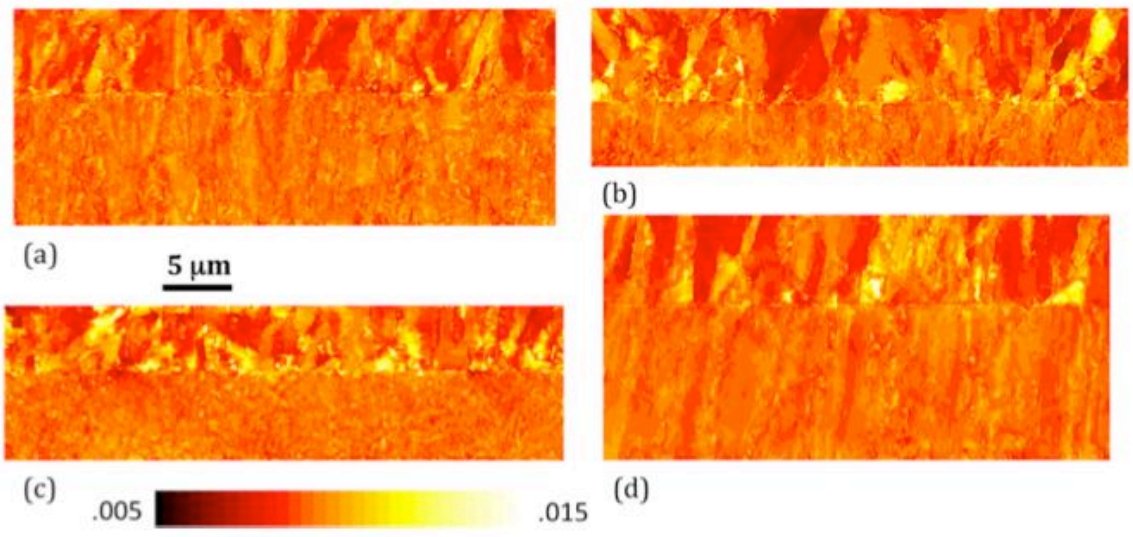

Figure 27. The stored elastic energy distributions for the coatings computed for ΔT = -800 K and strained lateral boundary conditions. The intensity (relative) is indicated by the shading of the figure. (a), (b), (c), and (d) are for sample 1, 2, 3, and 4, respectively.

The stored elastic energy distribution in the four coatings (with strained lateral boundaries to simulate the shrinking of the substrate) are shown in Fig. 27. The boundary conditions used for this simulation are different from the previous section. The CTEs of WC and Co are used to estimate a composite CTE (6.6x10-6/K) and then an -800 K change in temperature is assumed. The resulting strain is -0.0053 and half of this amount was applied to the left and right hand sides of the model. The images show that there is a broader range of stored elastic energy in the alumina layer and that the elastic energy varies with the sample microstructure. The main component of the strain in the coatings is in the lateral direction, ε_{xx}. This is the component of the strain imposed by the substrate and is tensile. The spatial distribution of strains in the coatings is illustrated in Fig. 28. The strains are all tensile. From these images, it is clear that the largest of the tensile strains is in the alumina layer. Furthermore, the distribution of strains in the alumina layers is much wider than in the TiC_xN_{1-x} layers and the width of the distribution varies in the different coatings. The distributions of strains and elastic energy densities are quantified through the histograms in Fig. 29. The strain in the direction parallel to the substrate (ε_{xx}) in samples 1 and 4 clearly has a lower average than samples 2 and 3. This same trend is reflected in the values of the stored elastic energy (Fig. 26(b)). The extreme (maximum) values for samples 2 and 3 exceed those of samples 1 and 4.

It is believed that the extreme values of stored elastic energy are the most important because these are potential fracture initiations sites [25, 26, 50, 63]. The maximum values occur

consistently in the α-Al_2O_3 layer as opposed to the TiC_xN_{1-x} layer, and for this reason it is concluded that the microstructure of the alumina layer is more important than the TiC_xN_{1-x} layer. The larger variations in the stored elastic energy in α-Al_2O_3 occur because it is trigonal, while TiC_xN_{1-x} is cubic. For this reason, the texture of the α-Al_2O_3 layer is important in determining the residual thermal stresses.

Strain and elastic energy density is lower for coatings with more intense (0001) texture. In this case, the thermal expansion anisotropy is the source of the reduced strain and stored energy. Alumina contracts more in the [0001] direction than any of the perpendicular directions. Therefore, the best match to the substrate can be obtained by orienting the low CTE directions parallel to the substrate and the high CTE direction perpendicular to the substrate so that the larger dimensional change occurs perpendicular to the free boundaries. Based on these calculations, strong (0001) texture acts to reduce thermal stresses resulting from both local misorientation and conformation to the substrate. In at least one case, coatings with this texture have been observed to have improved resistance to wear during cutting[66]. However, because there are many factors that affect wear processes during cutting, and the relative role of residual stress is not clear, it is not currently possible to directly relate the texture to coating performance.

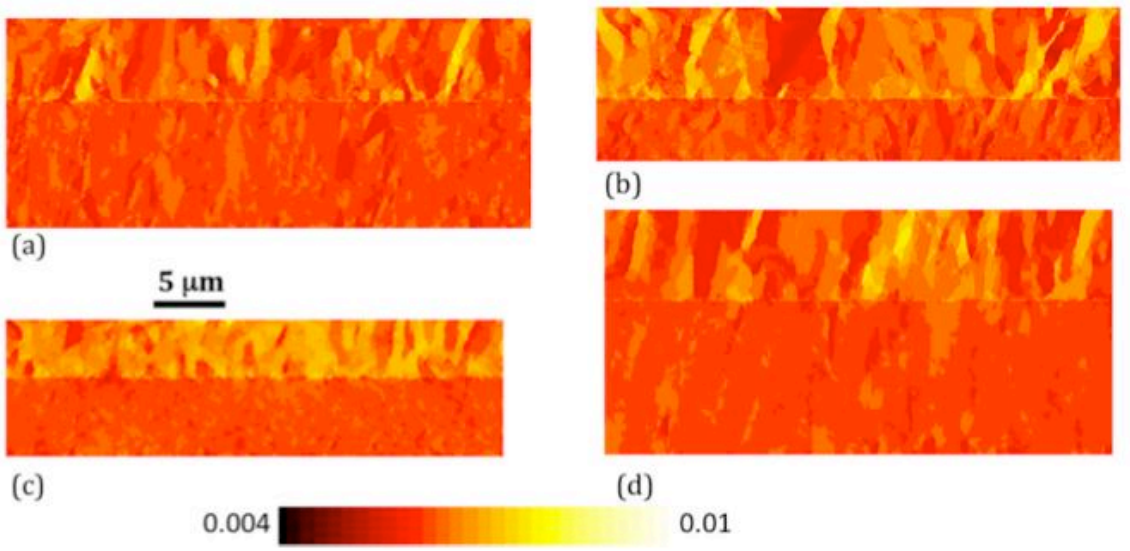

Figure 28. The horizontal component of the strain (εxx) for the four samples. The magnitude of the strain is indicated by the color. (a), (b), (c), and (d) are for sample 1, 2, 3, and 4, respectively.

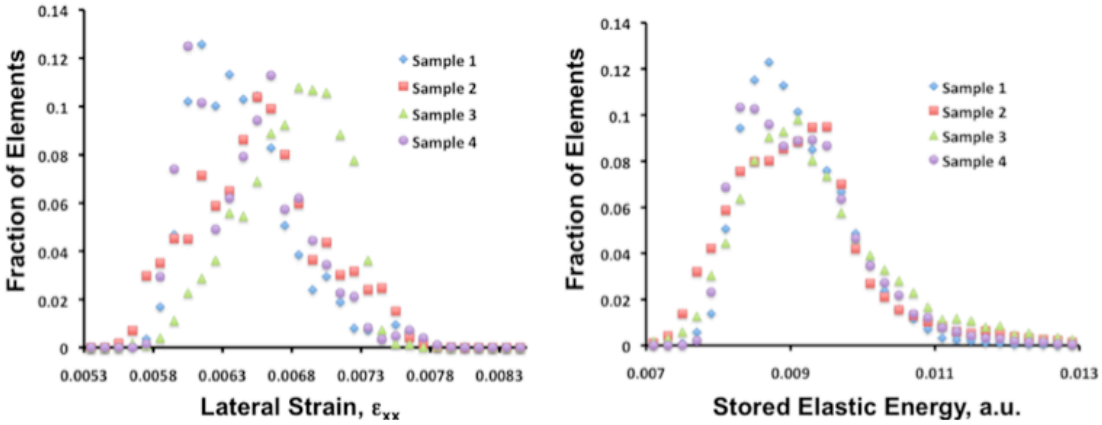

Figure 29. (a) Histogram of the horizontal component of the strain (ε_{xx}) for the four samples, based on the data in Fig. 27. (b) Histogram of the stored elastic energy of the four samples, based on the data in Fig. 26.

6.3 Effect of Cracks on Elastic Energies and Stress Distributions

6.3.1 Boundary Conditions and Materials Property Input

The simulations in the last section were simplified to isolate the influences of the

misorientation and the bilayer combination. The model presented in this section is intended to provide an accurate simulation of thermal stresses in real coatings. The thermal and elastic properties of each phase were assigned according to the data in Table 1. The properties of the TiC_xN_{1-x}, were estimated based on the properties of the pure phases. Because x is approximately 0.5, the coefficient of thermal expansion (CTE) for TiC_xN_{1-x} is assumed to be the average of TiN and TiC, which is 8.375 x 10^6 K^{-1}. Each of the elastic constants was also averaged (by averaging the individual components of the stiffness matrix that are listed in Table 1).

The boundary conditions of the simulation were set based on the assumption that the coating must conform to the substrate. Therefore, the CTE of the substrate was taken to be zero and the CTEs for the α-Al_2O_3 and TiC_xN_{1-x} were reduced by the CTE of the substrate. The left, right, and bottom of the model were assigned zero displacement and zero force boundary conditions. The system was then cooled by 800°C and the resulting stress and strain were calculated in each element. The domain of the computation ranges from 13,000 to 25,000 elements depending on the size of the image. Calculations based on the same models with 50 % more or 50 % fewer elements yielded the same results. The sizes of the models were adjusted so that the lateral dimension was equal to the average crack spacing.

6.3.2 Effect of Cracking in Al_2O_3 and TiC_xN_{1-x}

The distributions of stresses in the horizontal direction for each material are shown in Fig. 30. In each case, there are abrupt changes in the stresses between the substrate

(bottom), TiC_xN_{1-x} (middle), and α-Al_2O_3 (top) layers. In general, there is more stress in the TiC_xN_{1-x} layer than in the α-Al_2O_3 layer. This is because the thermal expansion mismatch between the coating and the substrate is largest in the TiC_xN_{1-x} layer. The thermal stress in sample 1 clearly has a lower average than samples 2, 3, and 4 for Al_2O_3 (shown in Fig. 31). This same trend is reflected in the thermal stress plot for TiC_xN_{1-x} in Fig. 32. The magnitudes of the calculated stresses in Al_2O_3 are consistent with measurements similar coatings by X-ray diffraction[59]. Both the microstructure of the sample and the cracks introduce heterogeneity in the distribution of stresses. The stresses in the parts of the coating closest to the crack are able to relax and the material furthest from the substrate can relax the most. Therefore, the overall stress relaxation is greater in the thicker coatings. However, there is an opposite effect on the substrate. Large tensile stresses are localized at the crack tip in the substrate and the thicker the film, the larger the extent of the stressed region.

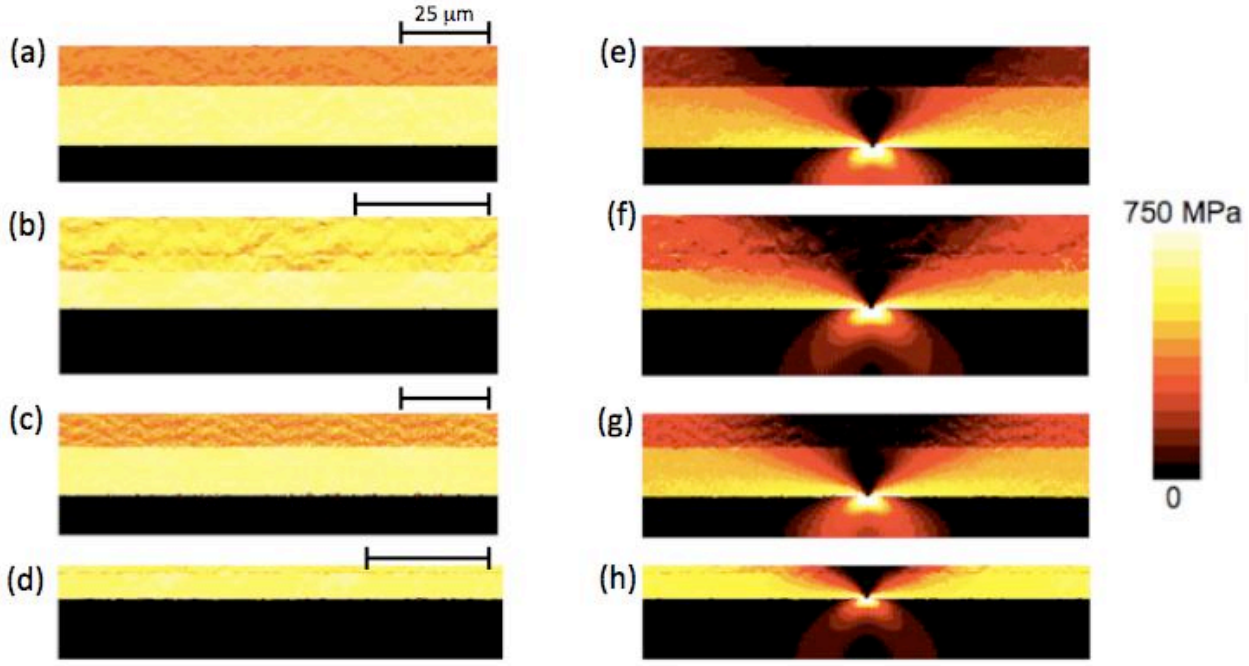

Figure 30. The thermal stress distribution along the x direction for the samples without cracks (a-d) and the same samples with a crack (e-h). All of the figures have the same stress scale, but have different lateral scales.

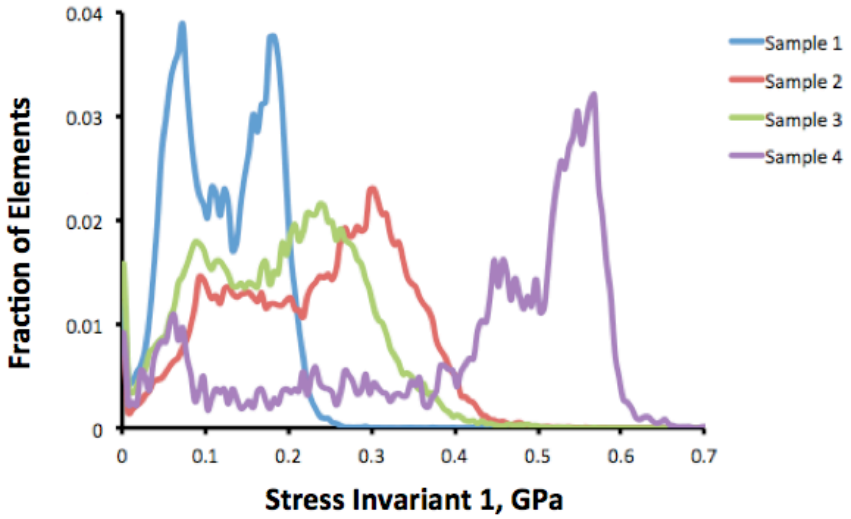

Figure 31. Histogram of the values of the stress invariant 1 in Al_2O_3 (trace of the stress tensor) in each element for the four samples, based on the data in Fig. 30 (e-h).

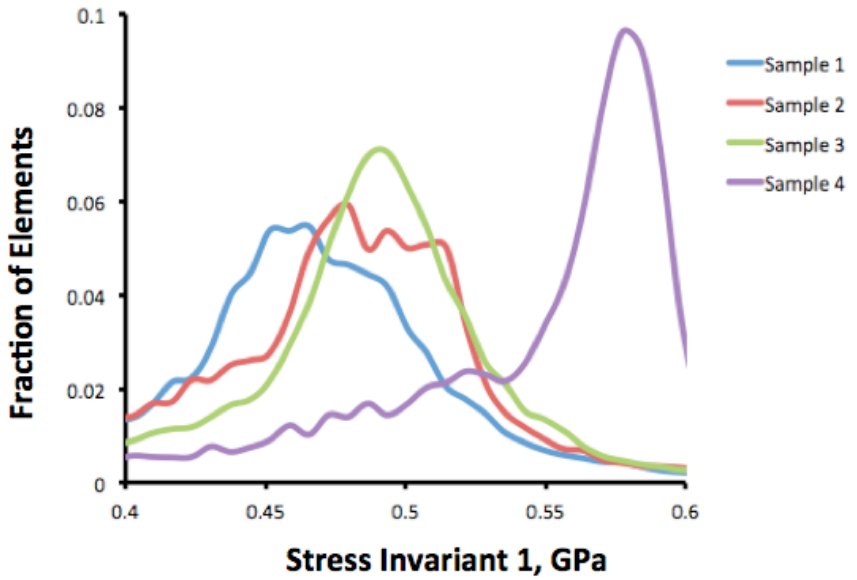

Figure 32. Histogram of the values of the stress invariant 1 in TiC_xN_{1-x} (trace of the stress tensor) in each element for the four samples, based on the data in Fig. 30 (e-h).

The distribution of the elastic energy density is shown in Figure 33. The trends evident in these plots are similar to what is observed in the plots of the stresses. Throughout most of the coating, the cracks reduce the amount of stored energy. However, in the region of the coating near the interface with the substrate, the elastic energy density is actually larger than before the crack. So, in this localized region, the crack increases the stored elastic energy. Similar to the case of the stresses, the crack is more effective in reducing the average elastic energies in the thicker films. However, the high energy density region in the substrate and near the interface is larger in the thicker films.

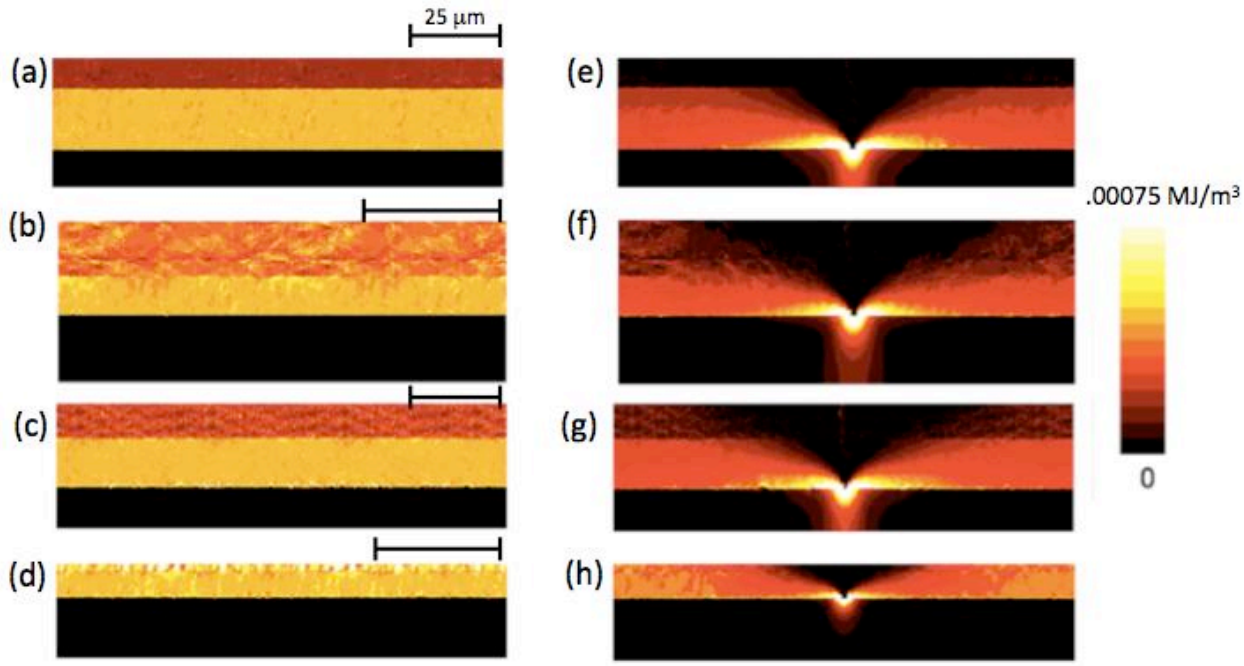

Figure 33. The elastic energy density distribution for all for samples without cracks (a-d) and with a single crack in the center (e-h). All of the figures have the same elastic energy scale, but different lateral scales.

These images provide a visual explanation to the effect of cracking on thermal stresses in the system. The first impression is that cracking decreases stress, strain, as well as elastic energy density. In Fig. 33, the amount of elastic energy density relieved in the Al_2O_3 region was not significant compared to the $TiC_xN_{(1-x)}$ region. An explanation for this effect could be the mismatch stresses between the $TiC_xN_{(1-x)}$ and the substrate are much higher than the mismatch stresses between the Al_2O_3 and the TiC_xN_{1-x}. It should also be recognized that the misorientation part of the strain in alumina is not relaxed by the crack, only the mismatch strain. $TiC_xN_{(1-x)}$ does not have misorientaion stresses, because it is cubic and thermally isotropic.

One interesting observation from Fig. 30 is the high stress state produced by the crack in the substrate region. This demonstrates that the crack has potential impacts on the substrate / tool failure when the coatings are partially worn off during machining. As the cracking width increases, the stress state in the substrate tends to become higher until the film wears off. Cracks will initiate at the very high stress state at the interface and propagate through substrate to relieve the stress and induce tool failure.

6.4 Correlation Between Hardness and Calculated Residual Stress

Fig. 34 shows the schematic image of how coating thickness and stress affect the crack density. All of the coatings have similar stress states, even though they have different crack spacing. Because cracks relieve less stress in thinner coatings, more cracks form to reach the same state. When the stresses fall below the coating's strength, no more cracks form.

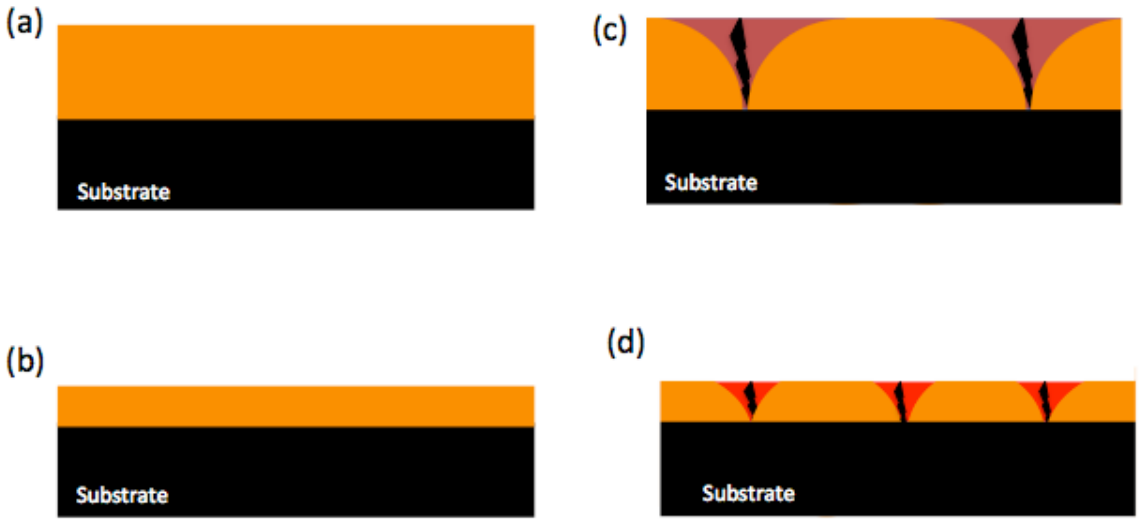

Figure 34. Schematics of thermal stress of coatings with different thickness before and after crack formation. The bottom black color represents the substrate whereas the orange color represents

stress in the coating. Red color shows the amount of thermal stress relieved. Darker red color means more stress relieved.

In Fig. 35, one of the clearest results from the calculations is that stress relaxation from the cracks increases with the film thickness for Al_2O_3 and TiC_xN_{1-x}. More thermal stress are relieved for Al_2O_3 than TiC_xN_{1-x}. The mean stresses in each layer are plotted as a function of film thickness. Although there is a very wide distribution of stresses, from the completely relaxed to completely unrelaxed states, here we consider the mean value as the representative quantity. The lower thermal stresses in the thicker films occurs because material further from the coating-substrate interface can relax more completely.

The main hypothesis of this work was that the calculated thermal stresses could be correlated to coating properties such as hardness. In general, coating hardness can be correlated with coating performance. This correlation is demonstrated in Fig. 36, which shows that the thermal stress is lower in coatings with higher hardness. The calculated fracture toughness is directly correlated to the hardness, so is not an independent variable. The correlation between calculated thermal stresses and hardness will be used to seek for improved coatings.

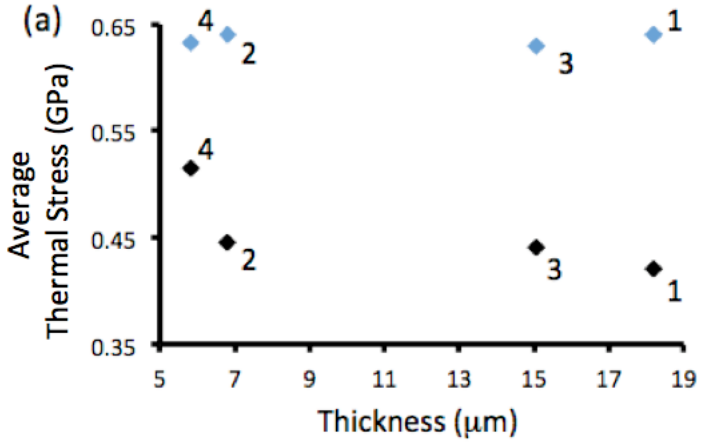

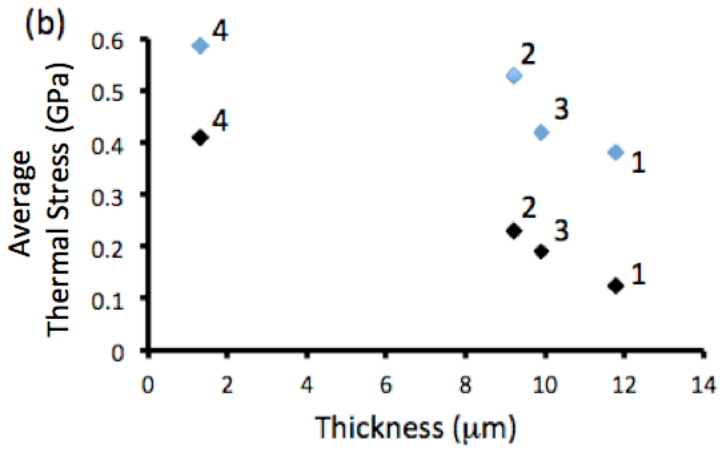

Figure 35. (a) Coating Thickness Versus Thermal Residual Stress for TiC_xN_{1-x}. (b) Coating Thickness versus Residual Thermal Stress for α-Al_2O_3. In each case, the numbers refer to the sample coating. Blue data points refer to the coatings without cracking and black data points refer to the coatings with cracking.

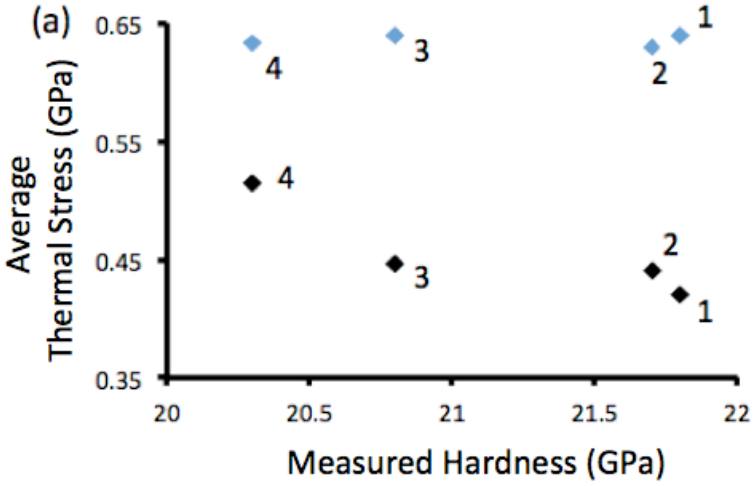

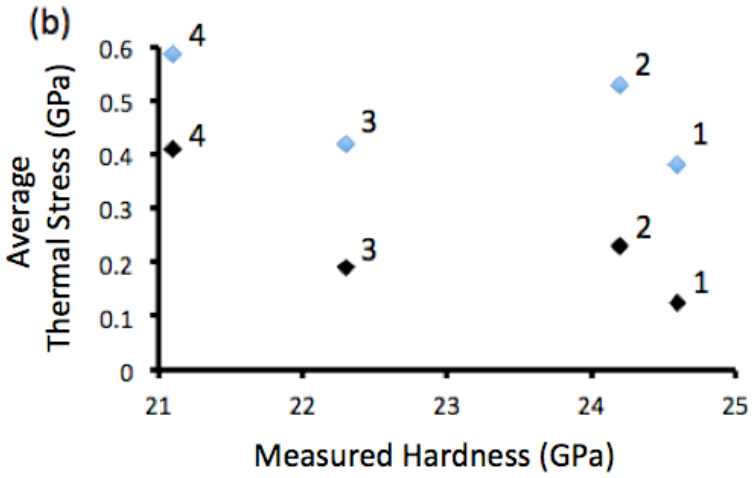

Figure 36. (a) Hardness Versus Thermal Residual Stress for TiC_xN_{1-x}. (b) Hardness Versus Residual Thermal Stress for a-Al_2O_3. In each case, the numbers refer to the sample coating.

The results show that channel cracking in the coating relieves the thermal stresses and this is thought to be responsible for the improved hardness. At some point, however, the cracks are also expected to have a negative impact on performance. If there are too many cracks, one would expect the coating to lack mechanical integrity. For example, if the regions of high elastic energy density at the coating-substrate interface in Fig. 33 begin to overlap, the cohesion of the coating and the substrate would be affected. Second it is clear that the cracks create tensile stresses in the substrate and this may promote cracking within the bulk of the tool. However, the extent of cracking in the present samples appears to still be in the region where it is beneficial, because the reduction of the thermal stresses by the cracks is correlated with increases in the hardness.

6.5 Summary

Realistic, microstructure based models of multilayer coatings on WC-Co substrates have been used to compute the thermal stress distribution. Channel cracks relieve stress in the coatings and this stress relief is more effective in thicker coatings. The residual thermal stresses are determined by the texture, thickness, and average crack spacing of the coating. The residual thermal stresses in the coating are inversely related to the hardness of the coating. This relationship provides guidance in the search for improved coatings.

Chapter 7

Thermal Stresses in Hypothetical Coating Structures

With the observation that increased coating hardness correlates with decreasing calculated residual thermal stress, the calculated residual thermal stresses of hypothetical structures were used to investigate effects of microstructural features on hardness. The purpose of this work is to understand how the microstructural characteristics of the Al_2O_3 and TiC_xN_{1-x} coating affect their hardness. By simulating the thermo-mechanical response of hypothetical microstructures, the effects of microstructural parameters such as grain aspect ratio, the composition of the cobalt-enriched region, coating thickness, and the stoichiometry (x) of TiC_xN_{1-x} can be independently evaluated. The substitution of AlON for Al_2O_3 is also explored. These microstructures were created to independently vary particular microstructure characteristics while keeping the others as constant as possible, so that each parameter's influence on the hardness could be independently determined.

7.1 Coating Thickness

In Fig. 37, three hypothetical structures with different coating thickness are illustrated. These microstructures were designed to have different coating thickness ranging from 2 μm to 6 μm while maintaining the average crack spacing, materials properties, and grain aspect ratio. The original microstructure was created by merging a

6 μm TiC_xN_{1-x} coating with homogeneous substrate. The coating layer was then cropped to create 2 μm and 4 μm TiC_xN_{1-x} coating structure. The crack was added as an additional phase (see Section 3.4.3). The materials properties used were listed in Table 1 and the boundary conditions used here were described in Section 6.3.1.

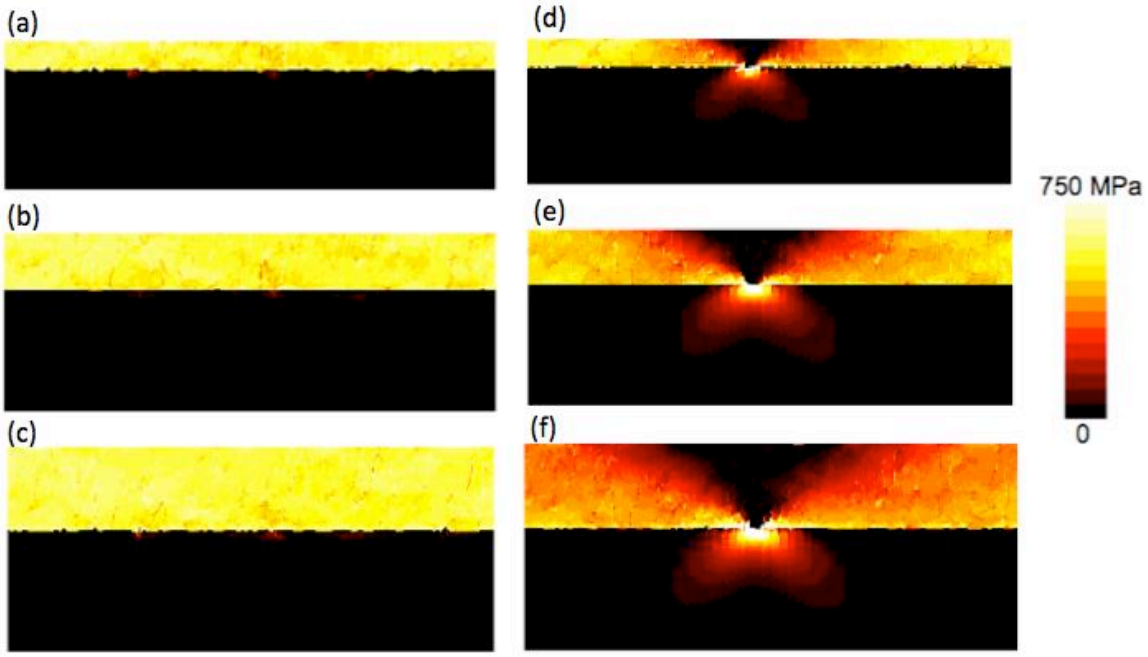

Figure 37. Stress distributions in hypothetical microstructures. Simulation is performed on TiCN coatings with 2 μm, 4 μm, and 6 μm thickness without cracks (a-c) and with a single crack in the center (d-f). All the figures have the same scale.

Fig. 37 (a) ~ (c) shows the stress of the TiC_xN_{1-x} coating without any cracking. It is apparent that stresses are the same despite the thickness effect. Whereas in Fig. 37 (d) ~ (f) the stress decreases as the coating thickness increases. The effect of cracking becomes more obvious with the thicker coatings as the amount of the stress relieved increases with the increasing length of the crack. The trend is also found in the data in Fig. 38. The figure

shows the average stress of the TiC_xN_{1-x} with and without cracking with different coating thickness. It is found that the stress state for all the coatings without cracks is the same despite the coating thickness. With cracks, the observation shows that increased coating thickness correlates with decreasing average thermal stress. Thicker coatings with cracks have more thermal stress relieved compared to thinner coatings with cracks. Using the correlation shown in Fig. 36, hardness can be increased by as much as a 9% when coating thickness increases from 2 μm to 6 μm, if the crack spacing remains constant.

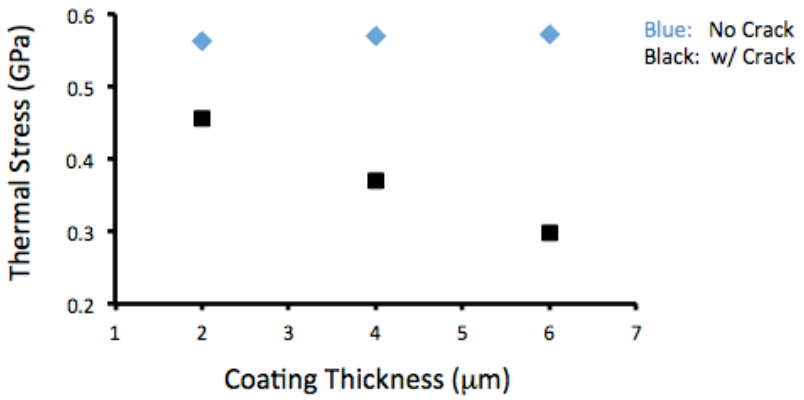

Figure 38. Average stress of the TiC_xN_{1-x} coating with different thicknesses. Stress decreases as coating thickness increases when the crack is added. Blue data points refer to simulations with no crack whereas black data points refer to simulations with a crack.

7.2 Thermal Stresses in Hypothetical AlON coatings

Aluminum oxynitride (AlON) is a ceramic material which could replace Al_2O_3 in a variety of applications[68], especially where optical transparency is important. The stoichiometry of aluminum oxynitride is Al_3O_3N. AlON is isotropic, single phase polycrystalline and has a cubic structure. Although AlON, to our knowledge, has not been

used as a tool coating, the crystal structure and the materials properties have potential to be considered as a replacement for Al_2O_3 [69-71]. In this section, the calculated thermal stresses in the Al_2O_3 are going to be compared with AlON.

In. Fig. 39, two hypothetical structures with different input materials properties are illustrated. The same Al_2O_3 microstructure is used for the thermal stress calculations in AlON and Al_2O_3. In these two simulations, the microstructure characteristics, thickness, and the width of the coating are fixed. The only difference is the input materials properties. Table 7 lists all the materials properties input for AlON and Al_2O_3. AlON has CTE nearly the same as Al_2O_3 but the modulus is less than Al_2O_3. Cracks were added in as additional phase (see Section 3.4.3) to investigate the effect of cracking. The boundary condition used here were described in Section 6.3.1.

Table 7. The materials properties input for the AlON and Al_2O_3 in hypothetical simulation. (a) Ref 70, (b) Ref 71.

Material	Young's Modulus (GPa)	Poisson's Ratio	Coefficient of Thermal Expansion ($x10^6$, K^{-1})	Elastic Constants (GPa)
AlON	207[a]	0.251[a]	7.8[b]	-
Al_2O_3	-	-	a_{11} = 7.67, a_{33} = 8.52[e]	C_{11} = 497 C_{12} = 163 C_{13} = 116 C_{14} = 22 C_{33} = 501 C_{44} = 147[f]

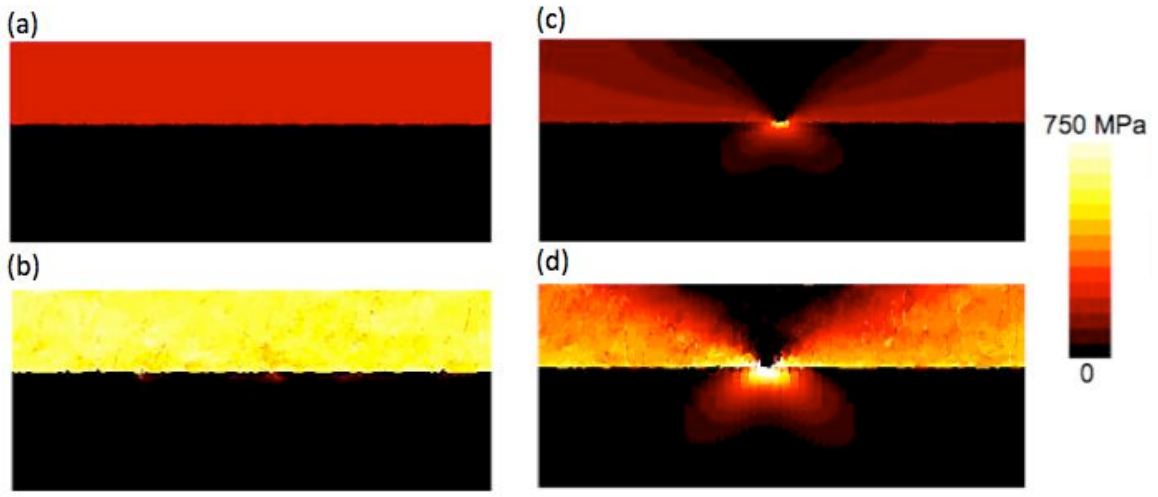

Figure 39. (a) and (b) show stress distribution in the AlON and Al_2O_3 without crack. (c) and (d) shows the stress distribution in AlON and Al_2O_3 with cracks.

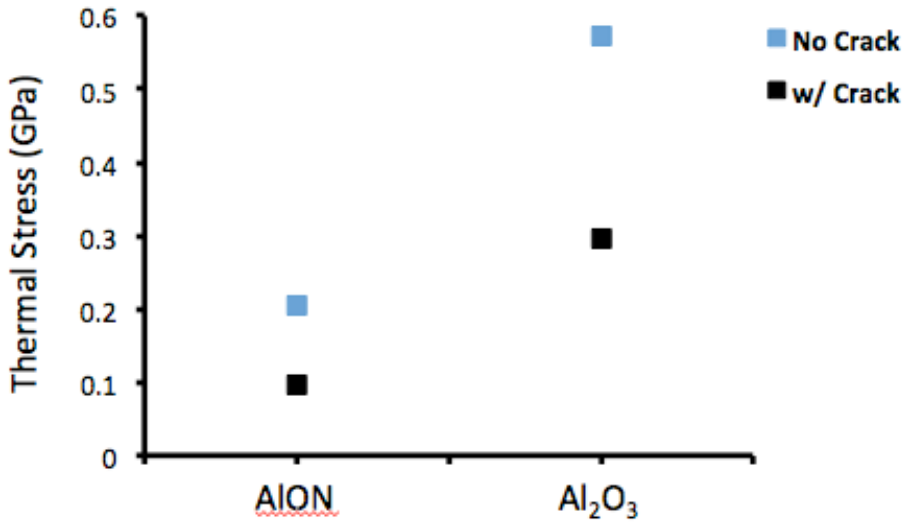

Figure 40. Average thermal stress in AlON and Al_2O_3 coatings. Blue data points refer to simulations with no cracks whereas black data points refer to simulations with cracks.

Without a crack built-in, the average thermal stress in AlON is two to three times less than in Al_2O_3. With a built-in crack, the average stress in AlON is decreased by 54% to 100 MPa and the average stress in Al_2O_3 is decreased by 48% to 300 MPa. The thermal stresses in AlON are lower because the modulus of AlON is lower. From the literature

reviews, AlON has an average hardness of 17.82 GPa with standard deviation of 1.4 GPa[68]. As predicted from the models built for TiC_xN_{1-x} and Al_2O_3, the thermal stresses decreases with increasing hardness. A relaxed AlON film is expected to follow the trend and have higher hardness. However, note that the bulk hardness of AlON is lower than alumina, so even though it has reduced thermal stress, coatings produced from this material might not be as hard.

7.3 Cobalt Enriched Substrate

The cobalt-enriched surface zone usually ranges from 10 to 40 μm thick and it provides superior edge strength while maintaining the wear resistance of the coating layer. Commercial WC-Co typically contains 3 to 25 wt% cobalt in the cobalt-enriched zone. For machining purpose, 3 to 12 wt% cobalt in the enriched zone is a common practice.

In this section, the effect of a cobalt enriched substrate was explored through three hypothetical substrates with different cobalt contents. The input materials properties used for each cobalt enriched zone are calculated based on the original properties of WC and Co shown in Table 8. The microstructural characteristics, coating thickness and width are all kept the same. Cracks were added as additional phase (see Section 3.4.3) to investigate the effect of cracking. The boundary conditions were described in Section 6.3.

Table 8. The materials properties input for the cobalt-enriched substrate. The materials properties for the cobalt enriched regions are calculated from the original WC and Co materials properties. Note that the wt% is changed to volume % for the calculations of different Co-enriched content.

Material	Young's Modulus (GPa)	Poisson's Ratio	Coefficient of Thermal Expansion (x10^6, K^{-1})	Elastic Constants (GPa)
WC	641.9	0.243	a_{11} = 5.2, a_{33} = 7.3[g]	-
Co	211[g]	0.31[g]	14.0[g]	-
3% WC-Co	628.9	0.245	7.4	-
12% WC-Co	590.2	0.25	6.24	-
25% WC-Co	531.2	0.26	5.46	-

In. Fig. 41, four hypothetical structures with different cobalt-enriched substrates are illustrated. All have a 3 wt% Co layer on the bottom. Fig. 41(a) shows a model with both 25 wt% and 12 wt% cobalt enriched layers whereas (b) shows a model with a 25 wt% cobalt enriched layer above the 3 wt% layer and (c) shows a 12 wt% cobalt enriched layer above the 3 wt% layer. In general, the maps show that the layers that are more highly enriched in Co have more stress than the regions without Co enrichment. This is illustrated, for example, by comparing Figs. 41 (a) and (d).

The effect of cobalt enriched regions on the stresses in TiC_xN_{1-x} can be found in Fig. 42 where the average thermal stress for the TiC_xN_{1-x} is shown for each case. The average thermal stress in TiC_xN_{1-x} with a 25 wt% cobalt enriched substrate is lower than in a 12 wt% cobalt enriched substrate. Likewise the average thermal stress in TiC_xN_{1-x} with a 12 wt% cobalt enriched substrate is lower with a 3 wt% cobalt enriched substrate.

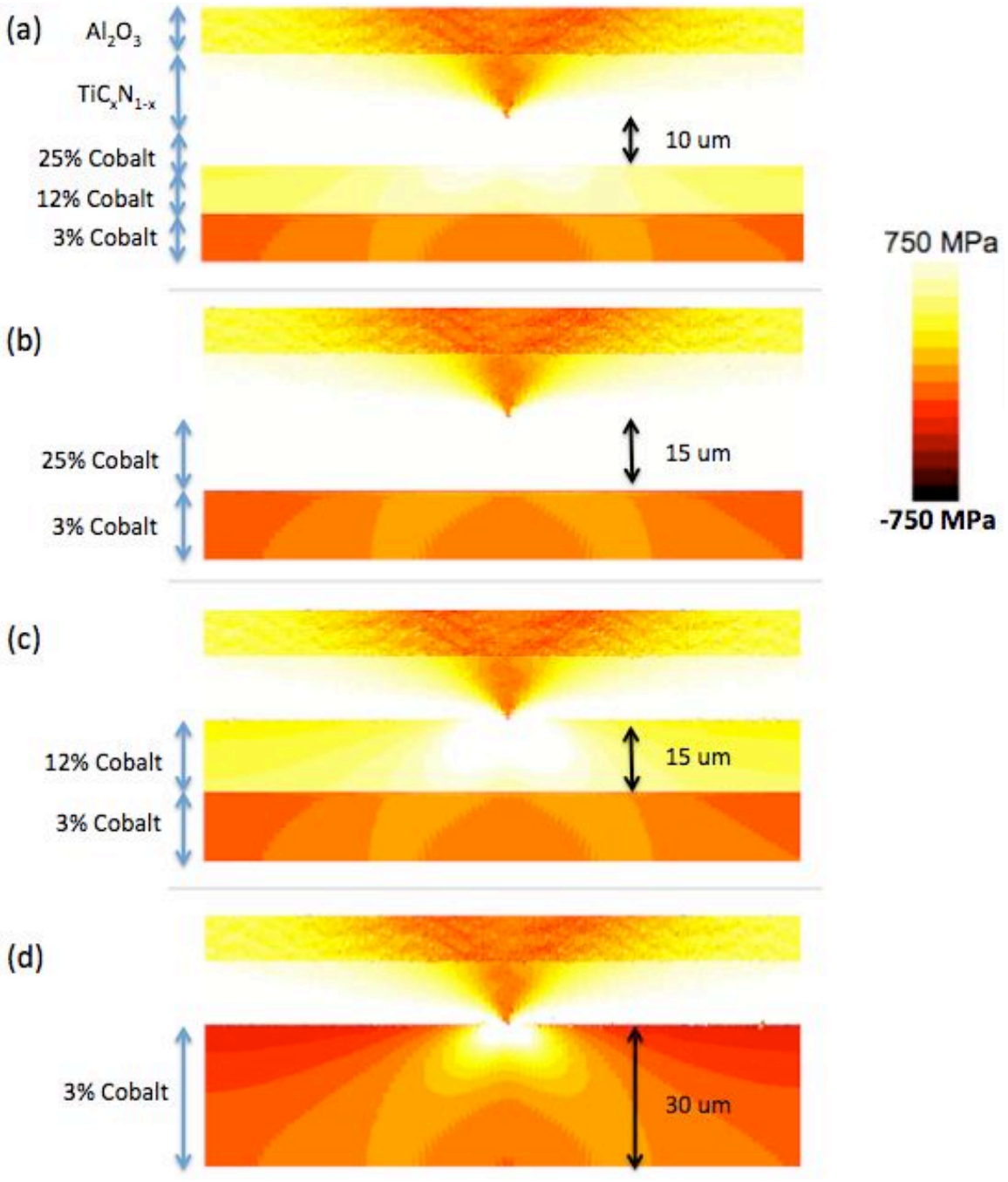

Figure 41. Thermal Stress for Al_2O_3 and TiC_xN_{1-x} on different cobalt-enriched substrates. (a) shows the effect of having two (25%, and 12%) cobalt enriched layers on top of 3%WC-Co. (b) shows a 25% cobalt enriched substrate. (c) shows a 12% cobalt enriched substrate, and (d) shows only the

uniform 3% cobalt content WC-Co. Note the scale ranges from 750 MPa to -750 MPa which is different from the other simulations.

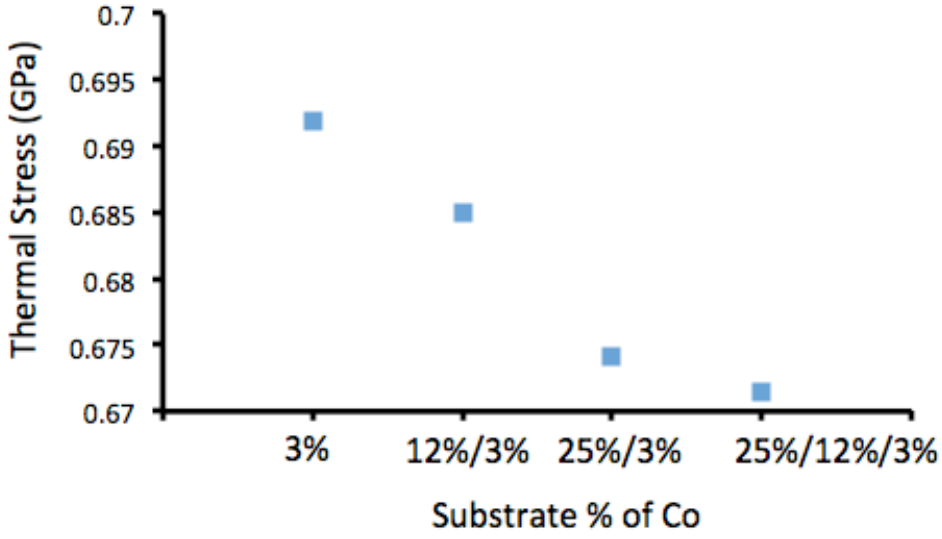

Figure 42. Average thermal stress in TiC_xN_{1-x} coating with different cobalt enrichment. Higher cobalt-enriched regions have smaller thermal stress.

The thermal stress is smaller for TiC_xN_{1-x} for substrates that are more highly enriched in Co. The coatings have less thermal stress with two Co-enriched layers compared to one Co-enriched layer. This is because of the small difference in CTE between the coating and the Co-enriched region. Substrates with higher cobalt content have smaller CTEs that are close to the coating's CTE and the thermal stress in the coating is minimized. The higher cobalt content in the cobalt enriched region can decrease the thermal stress by 2 ~ 3%, which would have only a small potential impact on the hardness (~1.2%) using the correlation in Fig. 36.

7.4 TiC_xN_{1-x} with different compositions

Previous simulations for the four materials use TiC_xN_{1-x} with x = 0.5 (see section 6.3.2). Tool manufacturers use the combination of TiC and TiN, attempting to combine the hardness of TiC and wear resistance of TiN. It was of great interest to adjust the composition (x value) in TiC_xN_{1-x} and see the effect of different TiC/TiN composition on thermal stress. With the composition changing, the effective materials properties such as the elastic constants and CTE have to be recalculated. Table 9 shows the recalculated materials properties with x ranging from 0.1, 0.3, 0.5, 0.7 to 0.9. The recalculated materials properties are based on a linear interpolation of the values of TiC and TiN.

In Fig. 43 Stress distributions for different compositions with and without cracks are illustrated. Cracks were added as an additional phase (see Section 3.4.3) to investigate the effect of cracking on different compositions of TiC_xN_{1-x}. The boundary conditions of the simulation were described in Section 6.3.1.

Table 9. The materials properties input for TiC_xN_{1-x}. The materials properties for the different TiC_xN_{1-x} are calculated from the original TiC and TiN materials properties.

Material	Young's Modulus (GPa)	Poisson's Ratio	Coefficient of Thermal Expansion ($x10^6$, K^{-1})	Elastic Constants (GPa)
TiN	-	-	9.35[a]	C_{11} = 625 C_{22} = 165 C_{44} = 163 A=0.709[b]
TiC	-	-	7.4[c]	C_{11} = 513 C_{12} = 106 C_{44} = 178 A=0.875[d]
$TiC_{0.1}N_{0.9}$	-	-	9.12	C_{11} = 524 C_{22} = 111.9 C_{44} = 176 A=0.858[b]
$TiC_{0.3}N_{0.7}$	-	-	8.77	C_{11} = 546 C_{22} = 123 C_{44} = 173 A=0.825[b]
$TiC_{0.5}N_{0.5}$	-	-	8.38	C_{11} = 569 C_{22} = 136 C_{44} = 170 A=0.792[b]
$TiC_{0.7}N_{0.3}$	-	-	7.98	C_{11} = 591 C_{22} = 147 C_{44} = 168 A=0.759[b]
$TiC_{0.9}N_{0.1}$	-	-	7.6	C_{11} = 625 C_{22} = 165 C_{44} = 165 A=0.726[b]

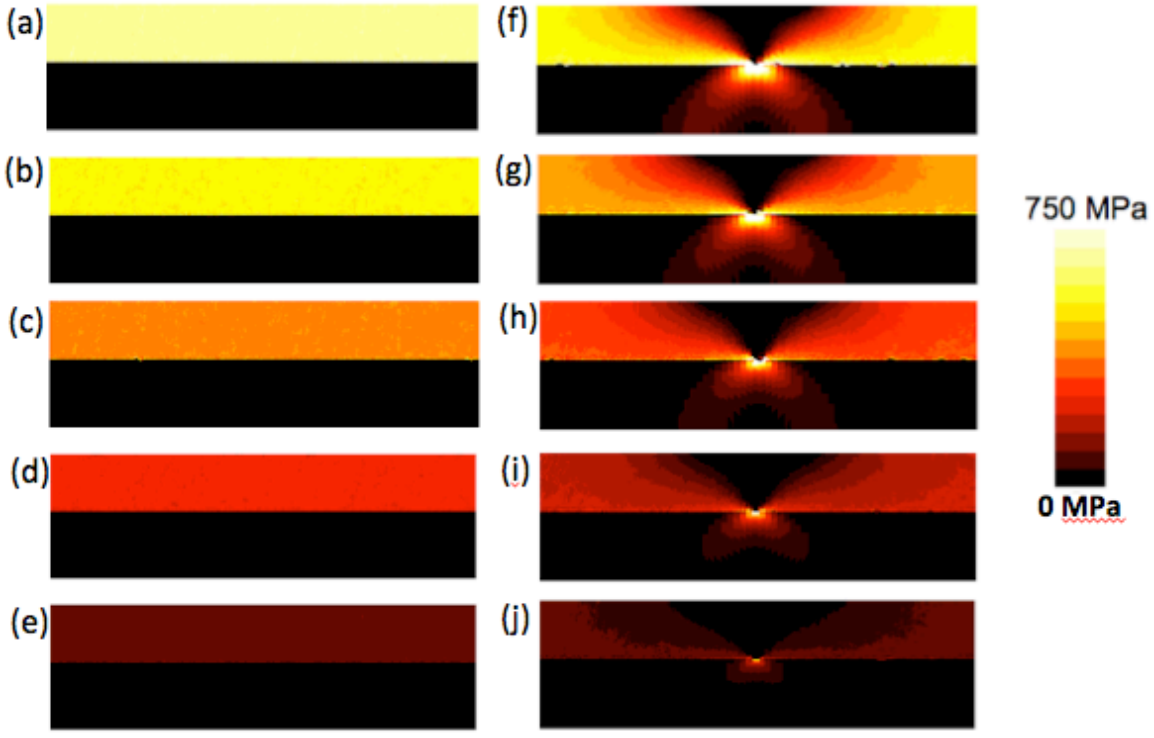

Figure 43. Stress distributions in coatings with different compositions. Simulation is performed on TiC_xN_{1-x} coatings with x = 0.1, 0.3, 0.5, 0.7, 0.9 for (a) ~ (e) and x = 0.1, 0.3, 0.5, 0.7, 0.9 with cracks in (f-j). All the figures have the same scale.

Fig. 44 shows the trend of the compositions in TiC_xN_{1-x} versus thermal stress. The thermal stress in the TiC_xN_{1-x} decreases as the carbon content of TiC increases. The difference in thermal stress is minimized at x equals 0.9. In another word, the effect of cracks on TiC_xN_{1-x} is minimized with increased carbon content. The result also implies that TiC has much lower stress compared to TiN and the effect of cracking in TiC is not obvious. One possible cause of this result is the materials properties of TiC. The elastic constant increases and the CTE decreases as the fraction of TiC increases. With a larger fraction of TiC in TiC_xN_{1-x}, the difference in the elastic constant and the CTE between TiC_xN_{1-x} and WC-Co becomes smaller and the thermal stress in the coating is minimized. Because TiC is harder than TiN, both the thermal stresses and the intrinsic properties favor an increased hardness. At the same time, some wear resistance may be sacrificed.

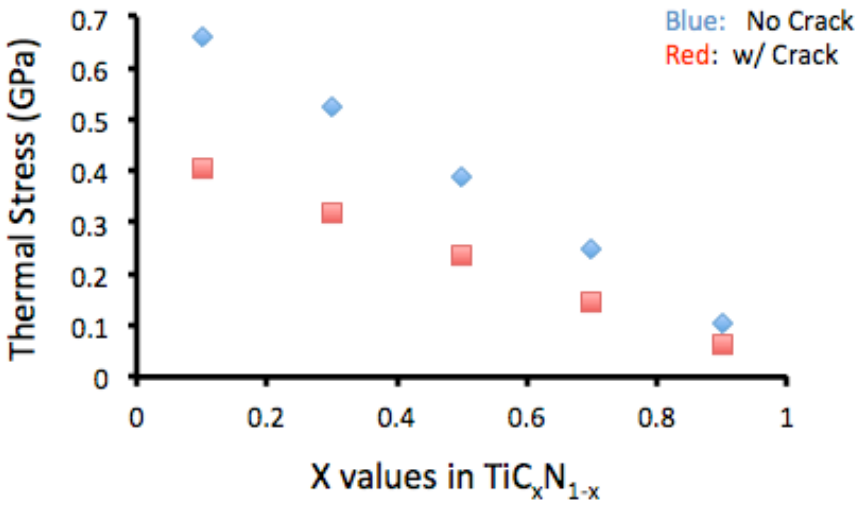

Figure 44. Thermal stress of TiC_xN_{1-x} coating with different compositions. The thermal stress decreases with increasing x value. Blue data points refer to those simulations without cracks and red points refer to the simulations with cracks.

7.5 Crack Spacing

In this part of the hypothetical structure simulation, the thermal stresses in coatings with different crack spacing were simulated. There are two cracks in the structure and the coating thickness and width are fixed. This is used to study the effect of crack spacing with a limited amount of cracks. In Section 6.3.2, the average crack spacing was fixed for each sample.

Five simulations were designed to test the effect of average crack spacing in TiC_xN_{1-x} on the calculated thermal stress in TiC_xN_{1-x}. The crack spacing ranges from 10 μm, 30 μm, 50 μm, 70 μm, and 90 μm. The effects were compared with two different coating thicknesses. Fig. 46 shows the effect of crack spacing on 4 μm TiC_xN_x film where as Fig. 46 shows the effect of crack spacing on 8 μm TiC_xN_x film. In Fig. 38, it was shown that with the crack built-in, the thermal stress in the coating decreases as the thickness of the coating increases. Similar results are observed here as the average thermal stress is lower for the 8 μm TiC_xN_{1-x} coatings.

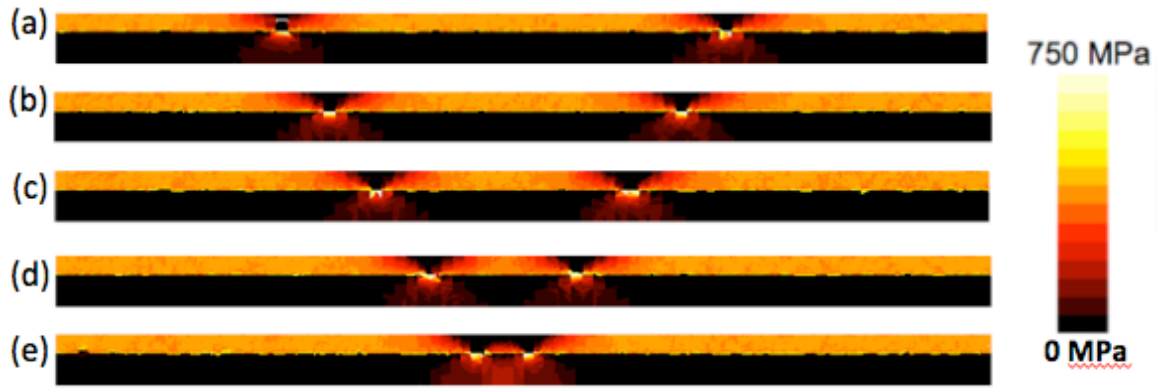

Figure 45. Stress distribution as a function of crack spacing. Simulations are performed on 4 μm TiC_xN_{1-x} coatings with crack spacing decreasing from 90 μm, 70 μm, 50 μm, 30 μm, to 10 μm shown in (a) to (e).

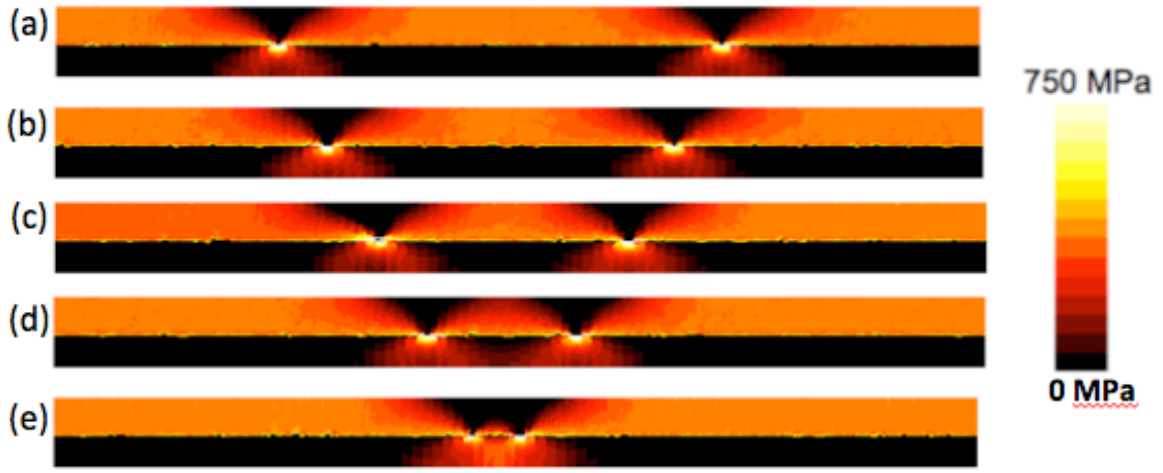

Figure 46. Stress distribution as a function of crack spacing. Simulations are performed on 8 μm TiC_xN_{1-x} coatings with crack spacing decreasing from 90 μm, 70 μm, 50 μm, 30 μm, to 10 μm shown in (a) to (e).

The trend of the crack spacing versus thermal stress can be observed in Fig. 47. The average thermal stress in samples with a 10 μm crack spacing is the highest because of the overlap in the stress-relieving region. The overlap region means that both cracks are relieving stresses in the same area. In another words, the cracks are now relieving thermal

stresses in smaller areas in the coating and this leads to a higher average stress. When the average crack spacing reaches to 50 μm, the thermal stress reaches to the smallest value meaning that moving the cracks closer together will not further reduce the stress. Interestingly, the thermal stress increases again when the crack spacing reaches to 70 μm or 90 μm. As the cracks get further apart, more unrelaxed material is placed between the cracks, and this is what raises the average calculated stress. Because there are no overlapping stress relieving regions at 70 μm or 90 μm cracking spacing, the maximum stress relief has already been achieved. Therefore the stress is increased again when the crack spacing exceeds 50 μm.

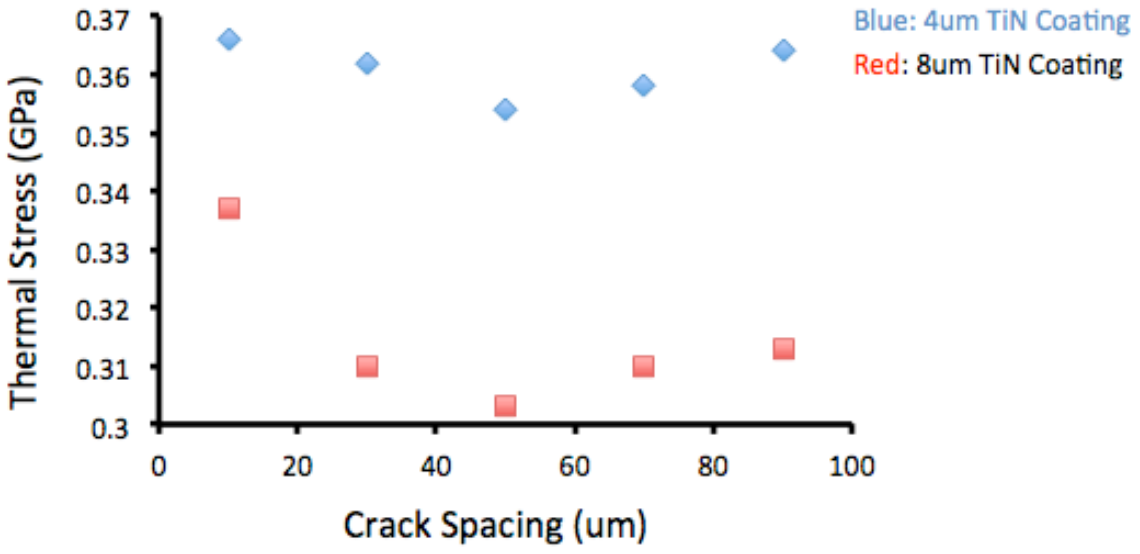

Figure 47. Average thermal stress of TiC_xN_{1-x} coatings with different crack spacing. Smaller crack spacings result in higher thermal stresses. The lowest thermal stress occurs for the 50 μm crack spacing.

7.6 Grain Aspect Ratio

In section 4.1, the microstructures the four samples were characterized and the grain aspect ratio was reported in Table 3. However, the correlation between grain aspect ratio and the thermal stress was not obvious because other parameters in the system were not constant. In this section, the effect of different grain aspect ratios in Al_2O_3 was explored through five hypothetical structures with the same texture. 20 grains were randomly selected from the four Al_2O_3 structures that were studied. The grains were modified to have different rectangular shapes to study the effect of grain aspect ratio. The boundary conditions are the same as the ones used in section 6.3.1 and the materials properties are for a TiC_xN_{1-x} layer on top of a homogeneous substrate.

Fig. 48 shows the microstructure used to calculate the thermal stress with different grain aspect ratios. Two other microstructures were built from stacked grains that have different aspect ratios. These structures have fixed coating width and different thickness. The effect of coating thickness does not affect the overall thermal stress in the coatings as shown in Fig. 37.

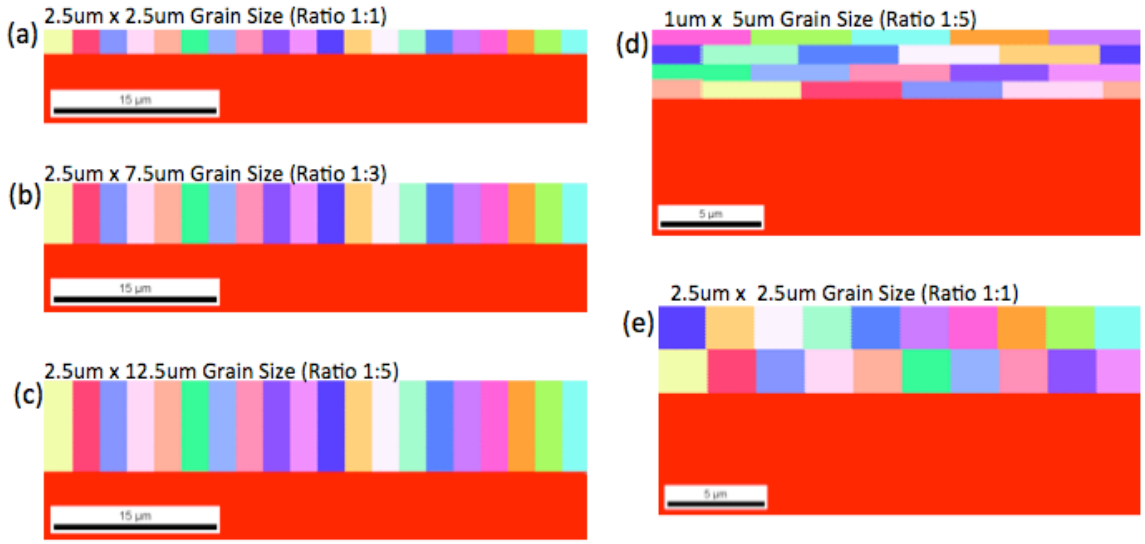

Figure 48. Microstructures used to measure the thermal stress with different gain aspect ratio shown in (a) to (c). Hypothetical grains with different aspect ratios are stacked in (d) and (e).

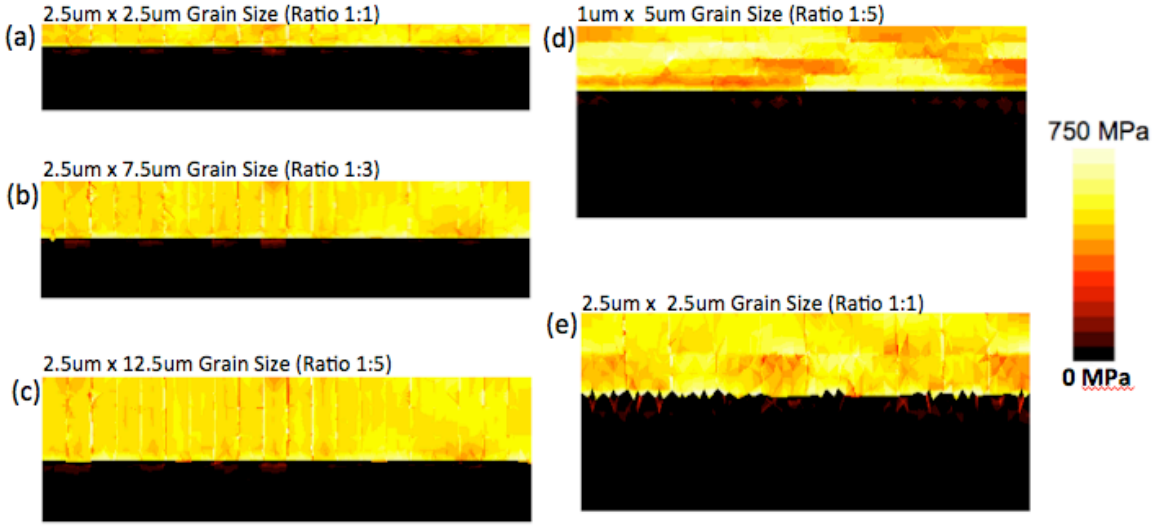

Figure 49. Stress distributions in hypothetical microstructures. The average stress decreases as the grain aspect ratio increases. The grains that are stacked (d) ~ (e) have thermal stresses that depends on the texture.

Fig. 50 shows the average thermal stress for each hypothetical structure. When the grains are aligned vertically, it was observed that a higher grain aspect ratio leads to lower

residual thermal stress in the coating. For horizontal grain arrangements, the smaller grain aspect ratios had the smaller stress. It should also be noted that the variations in stress are relatively small.

Some grains have lower thermal stresses from the visual observation in Fig. 49(d). By matching with the original microstructure in Fig. 48(d), it was observed that the c-axis oriented grains have less thermal stress. Similar to what was observed in section 6.2, Al_2O_3 contracts more in the c-axis direction than any other directions. Overall, the effect of grain aspect ratio on thermal stress is small because increasing the aspect ratio changes the thermal stress by only 1 ~ 2%.

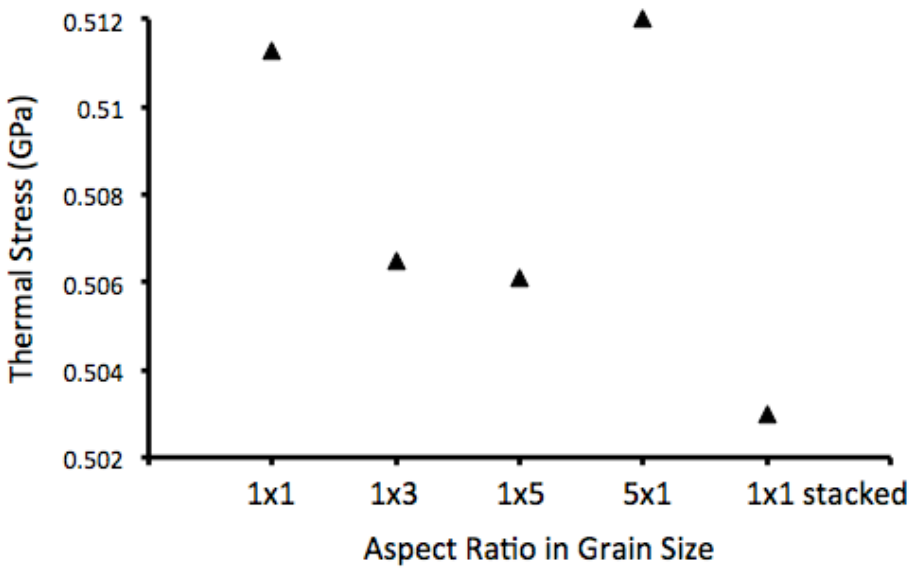

Figure 50. Average thermal stress of Al_2O_3 coatings with grain size that has different aspect ratio. When grains are aligned vertically, higher grain aspect ratios result in lower thermal stress. Lowest average thermal stress occurs when the grains are stacked and the grain aspect ratio is the smallest.

Chapter 8

Summary

This thesis focused on microstructure-property relationships in CVD deposited Al_2O_3 and TiC_xN_{1-x} coatings and had three main components: quantitative microstructural measurements, measurements of the mechanical properties, and the development of a model to predict hardness. Four different specimens consisting of TiC_xN_{1-x} ||α-Al_2O_3||TiN coatings deposited on WC-Co substrate, where 0.3<x<0.5, were used throughout this work.

Orientation imaging microscopy was used to characterize the microstructures of these specimens. Both coatings have columnar grains structures aligned with the film growth direction. The TiC_xN_{1-x} layers are highly twinned, with coherent twins making up 13% to 20 % of the grain boundary length. The TiC_xN_{1-x} layers have weak [112] or [101] textures in the growth direction. The Al_2O_3 layers have $[10\bar{1}4]$ or [0001] textures in the growth direction that are 4.2 to 8.8 times random.

Hardness measurements were made using a nanoindenter. The Al_2O_3 layers have hardnesses ranging from 18 GPa to 28 GPa and the TiC_xN_{1-x} layers have harness ranging from 19 GPa to 23 GPa. The hardest alumina coatings have $[10\bar{1}4]$ orientation texture and small grain sizes. The hardest TiC_xN_{1-x} coatings have a small grain sizes, [112] texture, and a high density of twins. No dominant correlations between the hardness and the grain size or the hardness and microtexture could be established for these four samples. An atomic force microscope (AFM) was used to image the indents, and it was found that cracks frequently

extended from the corners of the triangular indents. The hardness of the alumina layer in each material was found to be inversely proportional to the crack length.

The thermal stresses in the Al_2O_3 and TiC_xN_{1-x} coatings have been calculated using a two-dimensional finite element method (FEM) simulation. Orientation maps of the microstructures of the α-Al_2O_3 and TiC_xN_{1-x} multilayer coatings were used to create realistic models for input to finite element calculations of residual thermal stresses. The Al_2O_3 coating has calculated thermal stresses ranging from 300 MPa to 500 MPa and the isotropic TiC_xN_{1-x} coatings have an approximate thermal stress of 600 MPa. The mean value and distribution of stored elastic energy is influenced by the texture in the alumina layer. Increased (0001) texture leads to narrower distributions of stored elastic energy and the lateral thermal strain. The thermal expansion perpendicular to [0001] is less than the thermal expansion parallel to [0001] and, therefore, the thermal expansion mismatch between the alumina coating and the substrate is minimized when grains are oriented with [0001] perpendicular to the substrate.

Cracks were incorporated into the thermal stress calculations as an additional phase. The calculations show that channel cracks in the coatings relieve thermal stresses and that the amount of stress relieved increases with film thickness. The hardness and fracture toughness of the coatings are inversely correlated to the calculated mean thermal stress, where the hardest sample has the smallest mean thermal stress. With this correlation, hypothetical microstructures were examined to investigate the effects of individual microstructural features on the hardness of the coatings. In Fig. 51, the effects of microstructural features on the hardness are schematically illustrated. Here, the magnitudes of arrows indicate the extent of the effect on the hardness. The most important

is the composition of the TiC_xN_{1-x} layer. AlON has lower thermal stress than alumina, but its lower intrinsic hardness makes its application as a hard coating questionable. The coating thickness and cobalt enrichment are the next most important parameters. It is predicted that the hardness can be increased by as much as a 9% by increasing the coating thickness from 2 μm to 6 μm. The effects of cobalt enrichment in the substrate, the average crack spacing, and grain aspect ratio on hardness were also studied. It was found that a high cobalt content in the cobalt enriched region does not dramatically influence the thermal stresses and, presumably, the hardness.

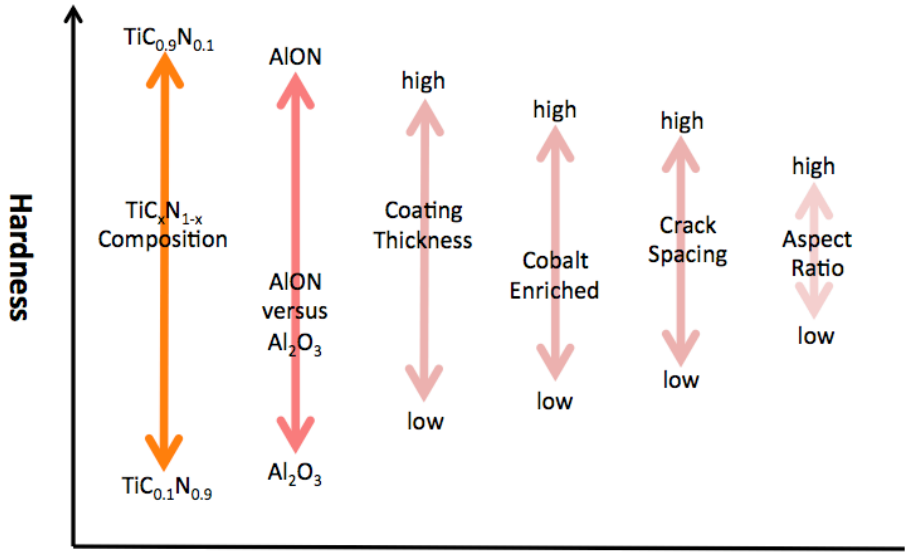

Figure 51. Schematic illustration of the effects of microstructural features and coating geometry, and composition on the hardness.

References:

[1] KL Choy, "Chemical vapour deposition of coatings," *Progress in Materials Science* 48, no. 2 (2003): 57-170.

[2] HE Rebenne, DG Bhat, "Review of CVD TiN Coatings for Wear-Resistant Applications – Deposition Processes, Properties and Performance." *Surface and Coating Technology* 63 (1994) 1-13

[3]DR Peterson, "Method of forming thin oxide films." (1964) U.S. Pat. No. 3,306,768

[4] RF Stroupe, WH Clingman, and RC Post, "Method of Forming Adherent Carbide Coatings on Metal or Composite Substrate." (1972) U.S. Pat. No. 3,684,585

[5] TE Hale, "Coated Cemented Carbide Product." (1973) U.S. Pat. No. 3,736,107

[6] RC Post, M Ferris, and M Dalla, "Article Coated with Titanium Carbide and Titanium Nitride." (1973) U.S. Pat. No. 3,874,900

[7] M Fallqvist, M Olsson, and S Ruppi, "Abrasive wear of texture-controlled CVD alpha-Al2O3 coatings," *Surface and Coating Technology* 202, no. 4-7 (2007): 837-843.
ffjria
[8] S Ruppi, "Wear characteristics of TiC, Ti(C,N), TiN and Al_2O_3 coatings in the turning of conventional and Ca-treated steels," *International Journal of Refractory & Hard Materials* 16, no. 4-6 (1998): 353-368.

[9] MH Staia, B Lewis, J Cawley, T Hudson, "Chemical Vapour Deposition of TiN on Stainless Steel," *Surface & Coating Technology* 76, no. 1-3 (1995): 231-236.

[10] M Fallqvist, M Olsson, S Ruppi "Abrasive Wear of Multilauer kappa-Al_2O_3 – Ti(C,N) CVD coatings on cemented carbide" *Wear* 263 no. 1 (2007):74-80

[11] H Chien, MC Gao, HM Miller, GS Rohrer, ZG Ban, P Prichard, YX Liu, "Microtexture and Hardness of CVD Deposited Coatings" *International. Journal of Refractory Metal.* **27** Vol 2, (2009): 458-464

[12] ROE Vijen, "Mechanical Measurement of the Residual Stress in Thin PVD Films," *Thin Solid Films* 270, no. 1-2 (1995): 264-269

[13] WD Kingery, *Introduction to Ceramics*, 2nd Ed., John Wiley and Sons, New York. (1976):595

[14] J.B. Wachtman,Jr., T.G. Scuderi, and G.W. Creek, "Linear thermal expansion of aluminum oxide and thorium oxide from 100-degree-K to 1100-degree-K"*Journal of American Ceramic Society*, 45, no. 7 (1962) 319-323

[15] PA Dearnley, "Rake and Flank Wear Mechanics of Coated and Uncoated Cemented Carbides," *Journal of Engineering Materials and Technology - Transactions of the ASME* 107, no. 1 (1985): 68-82.

[16] HG Prengel, WR Pfouts, and AT Santhanam, "State of the art in hard coatings for carbide cutting tools," *Surface & Coating Technology* 102, no. 3 (1998): 183-190.

[17] S Kudapa K Narasimhan, P Boppana, WC Russel, "Characterization and properties of MTCVD TiCN and MTCVD ZrCN coatings," *Surface & Coating Technology* 120 (1999): 259-264.

[18] S Ruppi, A Larsson, and A Flink, "Nanoindentation hardness, texture and microstructure of alpha-Al2O3 and kappa-Al2O3 coatings," *Thin Solid Films* 516, no. 18 (2008): 5959-5966.

[19] J Gurland, "New Scientific Approaches to Development of Tool Materials" *International Material Review.* 33 (1988) 151-166

[20] HE Exner "Physical and Chemical Nature of Cemented Carbides" *International Material Review.* 4 (1979) 149-173

[21] MU Farooq and U Klement, "EBSD Characterization of Carbide-carbide Boundaries in WC-Co Composites," *J. of Microscopy-Oxford* 213 (2004): 306-312.

[22] V Kumar, ZGZ Fang, SI Wright, MM Nowell "An analysis of grain boundaries and grain growth in cemented tungsten carbide using orientation imaging microscopy," *Metallurgical and Materials Transaction- A Physical Metallurgy and Materials Science* 37A, no. 3 (2006): 599-607.

[23] KP Mingard and MG Gee, "EBSD examination of worn WC/Co hardmetal surfaces," *WEAR* 263, no. Part. 1 Sp. Issue (2007): 643-652.

[24] CS Kim and GS Rohrer, "Geometric and Crystallographic Characterization of WC Surfaces and Grain Boundaries in WC-Co composites," *Interface Science* 12, no. 1 (2004): 19-27.

[25] CS Kim, TR Massa, and GS Rohrer, "Modeling the relationship between microstructural features and the strength of WC-Co composites," *International Journal of Refractory Metal & Hard Materials* 24, no. 1-2 (2006): 89-100.

[26] CS Kim, TR Massa, GS Rohrer, "Modeling the Influence of Orientation Texture on the Strength of WC-Co Composites"., *Jounral of American Ceramic Society* 90 (2007): 199-204

[27]ASM Handbook "Powder Metal Technologies and Applications" Sec. Ceramics and Intermetallics 3-17-3 (2002)

[28] P Hansson, M Halvarsson, and S Vuorinen, "Characterisation of the kappa-Al2O3-alpha-Al2O3 transformation in different single layer coatings of CVD kappa-Al2O3," *Surface & Coating Technology* 76, no. 1-3 (1995): 255-264.

[29] J Skogsmo, M Halvarsson, and S Vourinen, "Microstructural Study of the kappa-AL_2O_3 - alpha-AL_2O_3 Transformation in CVD kappa-AL_2O_3," *Surface & Coating Technology* 54, no. 1-3 (1992): 186-192.

[30] S Ruppi, A Larsson, and A Flink, "Nanoindentation hardness, texture and microstructure of alpha-Al2O3 and kappa-Al2O3 coatings," *Thin Solid Films* 516, no. 18 (2008): 5959-5966.

[31] S Ruppi, "Enhanced performance of alpha-Al2O3 coatings by control of crystal orientation," *Surface & Coating Technology* 202, no. 17 (2008): 4257-4269.

[32] Y Iwai, T Miyajima, A Mizuno, T Honda, T Itou, S Hogmark "Micro-Slurry-jet Erosion (MSE) testing of CVD TiC/TiN and TiC coatings," *WEAR* 267, no. Part 1 Sp. Iss SI (2009): 264-269.

[33] A Larsson and S Ruppi, "Microstructure and properties of Ti(C,N) coatings produced by moderate temperature chemical vapour deposition," *Thin Solid Films* 402, no. 1-2 (2002): 203-210.

[34] Q Ma, LC Liang, DR Clarke, JW Hutchinson, "Mechanics of the Push-Out Process From In Situ Measurement of the Stress Distribution Along Embedded Sapphire Fibers", Acta Metallurgica et Materialia, 24, 10, (1994) 3299-3308

[35] VR Vedula, S Glass, D Saylor, G. Rohrer, W Carter, S Langer, E Fuller, "Residual-stress predictions in polycrystalline alumina," *Journal of the American Ceramic Society* 84, no. 12 (2001): 2947-2954.

[36] J Hutchinson and Z Suo, "Mixed Mode Cracking in Layered Materials" *Advances in Applied Mechanics* 29, (1992) : 63-191

[37] A Evans and J Hutchinson, "The Thermomechanical Integrety of Thin Films and Multilayers", *Acta Metall. Mater.* 43, no. 7 (1995): 2507-2530

[38] J Beuth, "Cracking of Thin Bonded Films in Residual Tension" *International Journal of Solids and Structures,* 29, No. 13 (1992): 1657-1675

[39] T Nakamura and S Kamath, "3-Dimensional Effects in Thin-Film Fracture-Mechanics" 13, No. 1 (1992):67-77

[40] V Randle and L Engler, *Introduction to Texture Analysis*, 1st ed. (Taylor & Francis Ltd, 2002).

[41] GE Dieter, *Mechanical Metallurgy*, 2nd ed. (McGraw-Hill, Inc, 2000).

[42] TH Courtney, *Mechanical Behavior of Materials*, 2nd ed. (McGraw-Hill, Inc, 2000).

[43] WC Oliver and GM Pharr, "Measurement of Thin-Film Mechanical Properties using Nanoindentation," *Journal of Materials Science* 17, no. 7 (1992): 28-33.

[44] J Wagner, V Edlmayr, M Penoy, C Michotte, C Mitterer, M Kathrein, "Deposition of Ti-Al-N coatings by thermal CVD," *International Journal of Refractory Metals & Hard Materials* 26, no. 6 (2008): 563-568.

[45] DK Lee, SH Lee, and JJ Lee, "The structure and mechanical properties of multilayer TiN/(Ti0.5Al0.5)N coatings deposited by plasma enhanced chemical vapor deposition," *Surface & Coating Technology* 169 (2003): 433-437.

[46] Y Sun, A Bloyce, T Bell, "Finite element analysis of plastic deformation of various TiN coatings/substrate systems under normal contact with a rigid sphere" *Thin Solid Films* 271, (1995):122-131

[47] KA Khor, YW Gu, "Effects of residual stress on the performance of plasma sprayed functionally graded ZrO2/NiCoCrAlY coatings", *Materials Science and Engineering* 227 (2000):64-76

[48] J Cheng, EH Jordan, B Barber, M Gell, "Thermal/Residual stress in an electron beam physical vapor deposited thermal barrier coating system", *Acta Mater* 46 (1998):5839-5850

[49] YC Yen A Jain, P Chigurupati, W Wu, T Altan, "Computer simulation of orthogonal cutting using a tool with multiple coatings," *Machining Science and Technology* 8, no. 2 (2004): 305-326.v

[50] C Hseuh, J Haynes, M Lance, P Becher, M Ferber, E Fuller, S Langer, W Carter, W Cannon, "Effects of Interface Roughness on Residual Stresses in Thermal Barrier Coatings," *Journal of American Ceramics*, 82, no. 4 (1999): 1073-1075

[51] JE Blendell, M Vaudin, E Fuller, "Determination of texture from individual grain orientation measurements" *Journal of American Ceramic Society* 82, (1999): 3217–20.

[52] The program can be downloaded at: http://rsb.info.nih.gov/ij/

[53] DG Brandon, "The structure of high angle grain boundaries" *Acta Meta* Vol 4, (1966): 1479- 84.

[54] TestWorks 4 Software for Nanoindentation Systems Manual.

[55] J.O. Kim, J.D. Achenbach, P.B. Mirkarimi, M. Shinn, and S.A. Barnett, *Journal of Appied Physics.* **72** [5], (1992):1805-1811

[56] D. Maouche , L. Louail , P. Ruterana , M. Maamach, "Formation and stability of di-transition-metal carbides TixZr1-xC, TixHf1-xC and HfxZr1-xC "*Computational Materials Science* 44 [2], (2008): 347-350

[57] J.B. Wachtman,Jr., T.G. Scuderi, and G.W. Creek, "Linear Thermal Expansion of Aluminum

Oxide and Thorium Oxide From 100-Degree-K to 1100 Degree-K", *Journal of American Ceramic Society* 45 [7], (1962):319-323

[58] J.R. Gladden, J.H. So, J.D. Maynard, P.W. Saxe, and Y. Le Page, "Reconciliation of ab initio theory and experimental elastic properties of Al_2O_3" *Applied Physics Letter* **85** [3], (2004):392- 395

[59] D.B. Hovis, A. Reddy, and A.H. Heuer, "X-ray elastic constants for alpha-Al_2O_3" *Applied Physics Letter* **88** [13], (2006):1310-19

[60] M. Lee, R.S. Gilmore, "Single-Crystal Elastic Constants of Tungsten Monocarbide", *Journal of Materials Science* **17** [9], (1982):2657-60

[61] A. Kelly, G.W. Groves, Crystallography and Crystal Defects, pp. N, Longman, London, (1973)

[62] W.M. Stoll, A.T. Santhanam, *Kirk-Othmer Encyclopedia of Chemical Technology. 4th ed*, John Wiley and Sons, (1992):861

[63] DM Saylor, BS El-Dasher, BL Adams, GS Rohrer, "Measuring the five parameter grain boundary distribution from observations of planar sections" *Metal and Materials Transaction* Vol 35A (2004): 1981-89.

[64] GS Rohrer, DM Saylor, B El-Dasher, BL Adams, AD Rollett, P Wynblatt, "The distribution of internal interfaces in polycrystals" Vol 95, *Zeitschrift Fur Metallkunde* (2004): 197-214.

[65] G. Galal Yousef, J. Rödel, E.R. Fuller Jr., A. Zimmerman, "Microcrack evolution in alumina ceramics: Experiment and simulation" B.S. El-Dasher, *Journal of American Ceramic Society.*, **88** [10], (2005): 2809-16

[66] S. Ruppi, "Enhanced performance of alpha-Al2O3 coatings by control of crystal orientation" *Surface and Coating Technology*, 202, 17 (2008) 4257-4269

[67] S. S. Smith, B. J. Pletka, "Indentation Fracture of Single Crystal and Polycrystalline Aluminum Oxide" *Fracture Mechanics of Ceramics,* 6 (1983) 189-209

[68] N.D. Corbin "Aluminum Oxynitride Spinel: A Review" *Journal of the European Ceramic Society*, 5 (1989) 143 - 154

[69] D.P. Dandekar, B.A.M. Vaughan, W.G.Proud "Shear Strength of Aluminum Oxynitride" *Shock Compression of Condensed Matter*, 955 (2007) 505 – 508

[70] W. Xiao, X. Jiang "Optical and Mechanical Properties of Nanocrystalline Aluminum Oxynitride Films Prepared by Electron Cyclotron Resonance Plasma Enhanced Chemical Vapor Deposition" *Journal of Crystal Growth*, 264 (2004) 165 - 171

[71] W.Kollenberg, J. Margalit "Thermal Expansion of AlON and γ-Al_2O_3 "*Journal of Materials Science Letters*, 11 (1992) 991 - 993

Appendix A

OOF2 Tutorial Guide

After you run the OOF2 program, you will first come to the “welcome menu”. You can get more information from http://www.ctcms.nist.gov/~langer/oof2man for the definition of what each button means.

In this tutorial I will be showing how to calculate the stress along x direction from a simple image with 2 different colors.

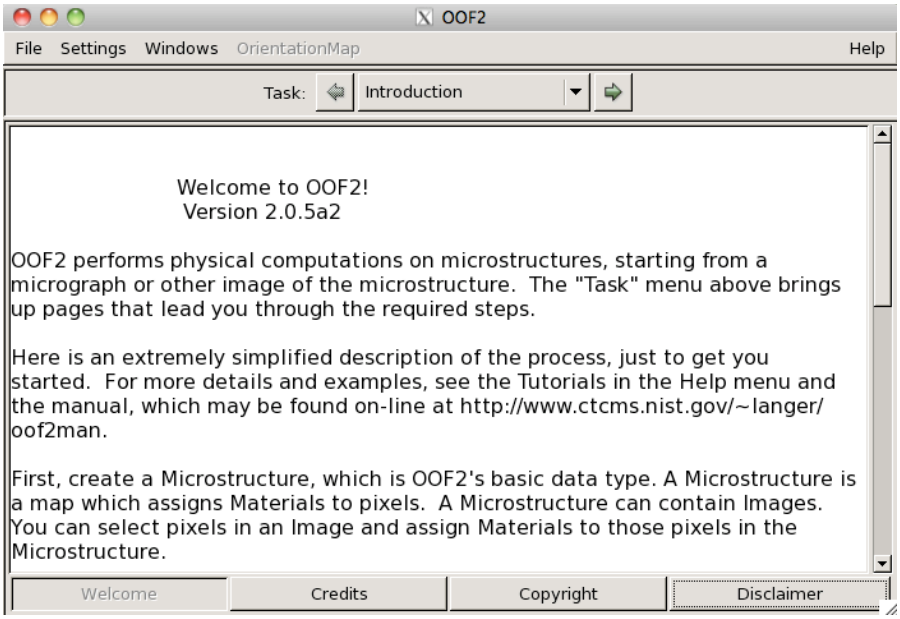

First, click on the ‘Task’ menu and select “Microstructure”

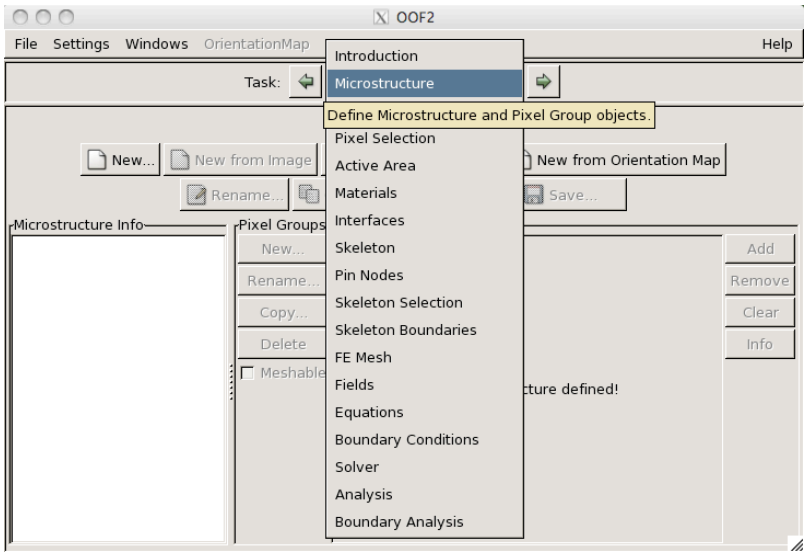
OOF2
File
Settings
Windows
OrientationMap
Help
Task:
Introduction
Microstructure
Define Microstructure and Pixel Group objects.
Pixel Selection
Active Area
Materials
Interfaces
Skeleton
Pin Nodes
Skeleton Selection
Skeleton Boundaries
FE Mesh
Fields
Equations
Boundary Conditions
Solver
Analysis
Boundary Analysis
New...
New from Image
New from Orientation Map
Rename...
Save...
Microstructure Info
Pixel Groups
New...
Rename...
Copy...
Delete
Meshable
Add
Remove
Clear
Info

Here you can choose your input file types. If you have an output grain file from EBSD map. You should click on “New from Orientation Map”. In this tutorial, we are going to work on a simple image I created from powerpoint.

In this case, we want to click on the button “New from Image File.

Next, select the image from your directory

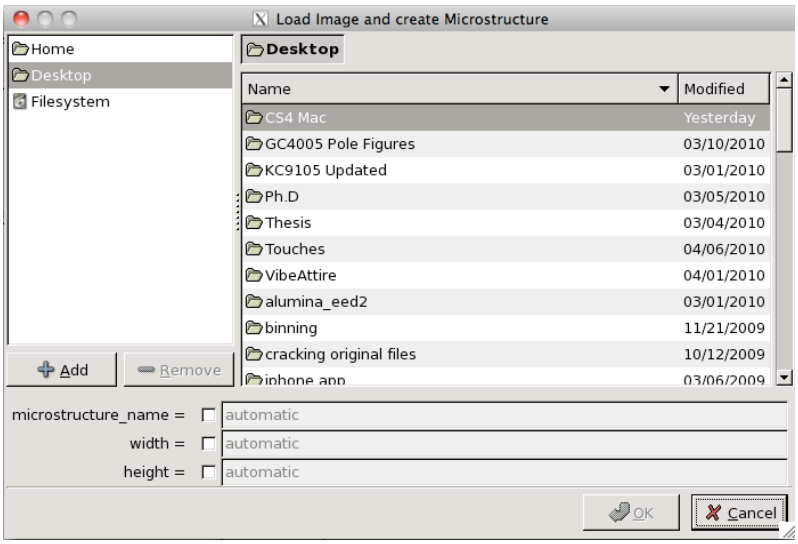

Once you have selected the image. You will see the microstructure info. on the left

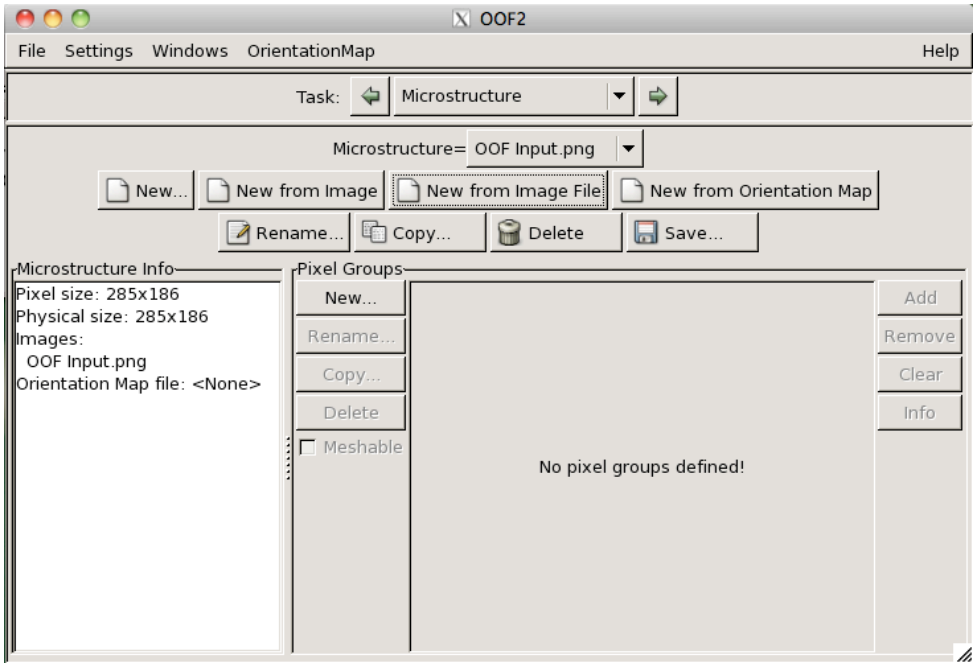

From now you can click on Windows > Graphics > New to see the image you have uploaded in OOF2 in a new window

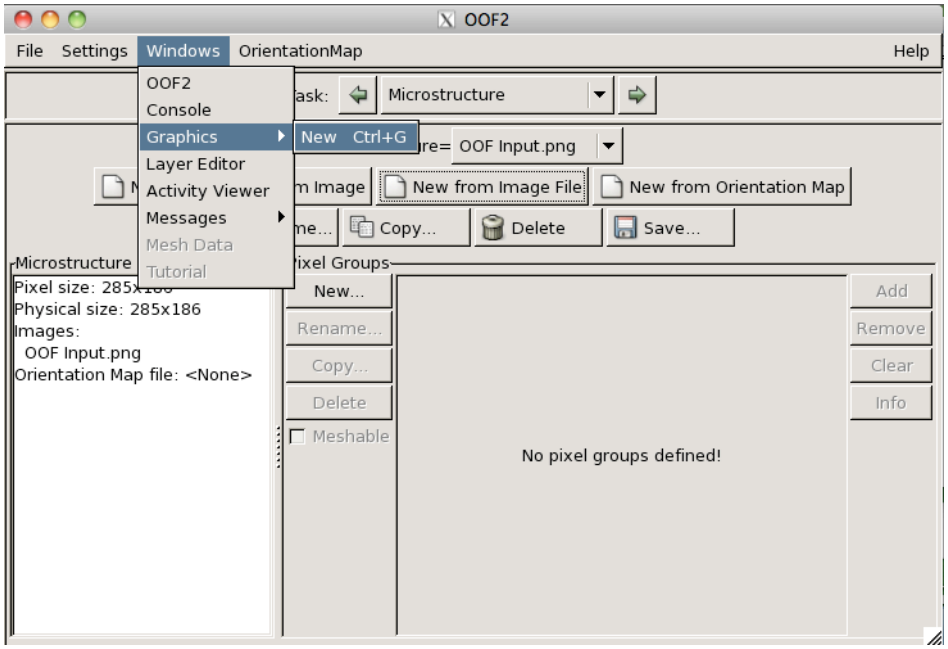

You will be able to see all the working progress in this graphics window throughout the procedure, You will need to keep this window open to see the result of each step.

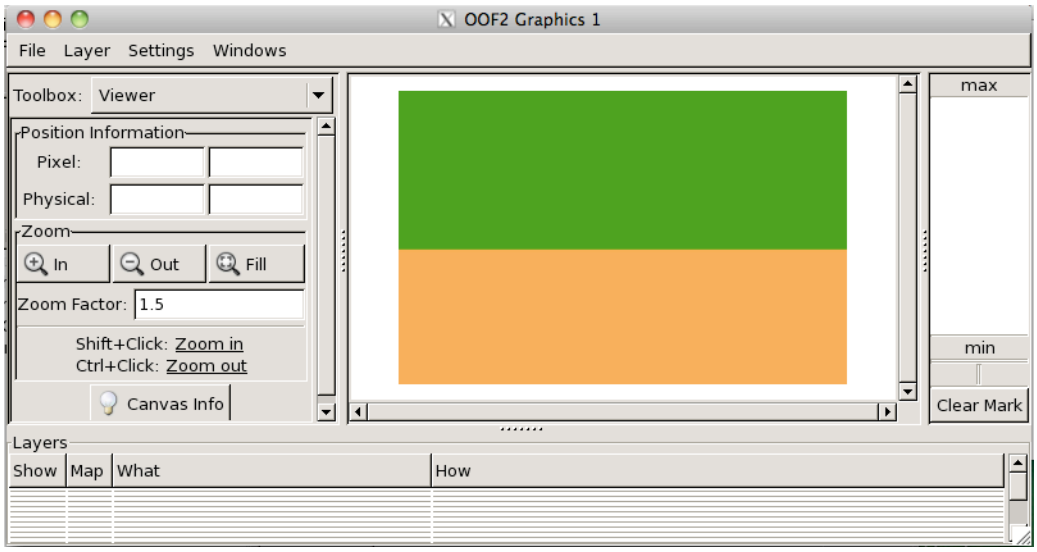

Now, go back to the main menu under “Microstructure” task - From the pixel group - select “New” and give a name called ‘top’.

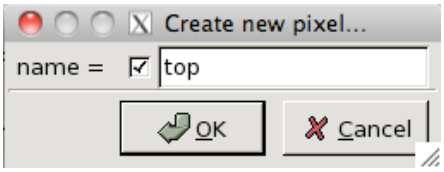

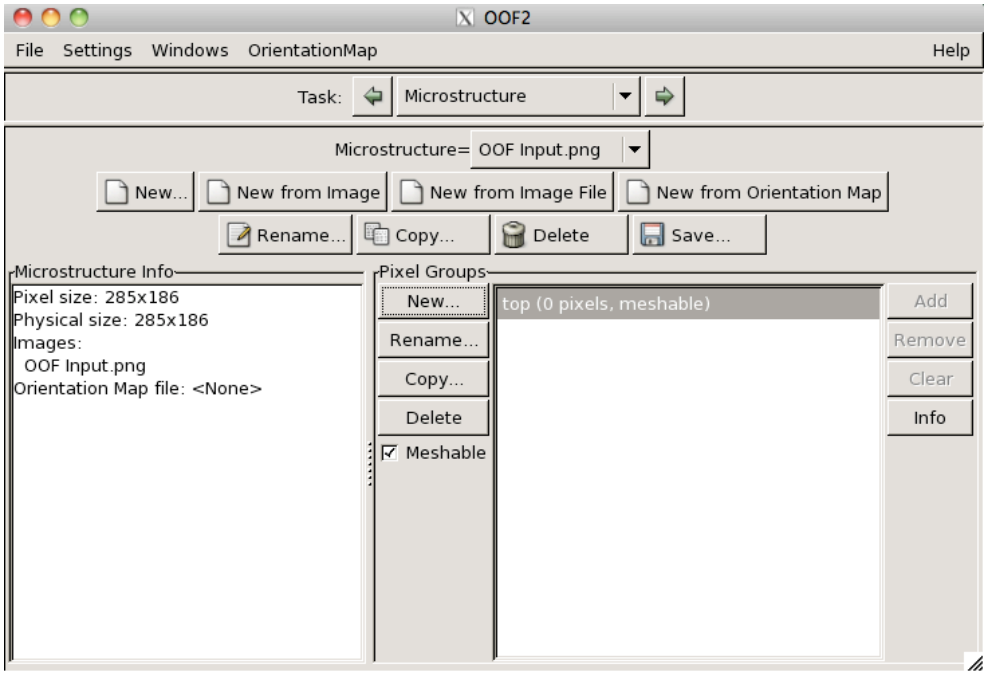

It says no pixels have been added so far. Because we have not assigned any pixel values to the “top” pixel groups yet. Now we want to create another pixel group called “bottom”. Click on “New” again and give it a name called “bottom”

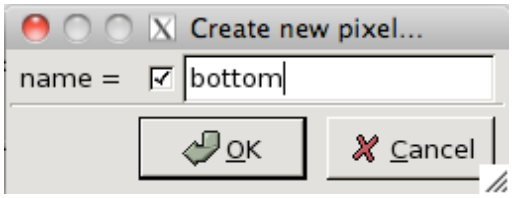

Now we will go back to the graphics menu. From the Toolbox, select “Pixel Selection”

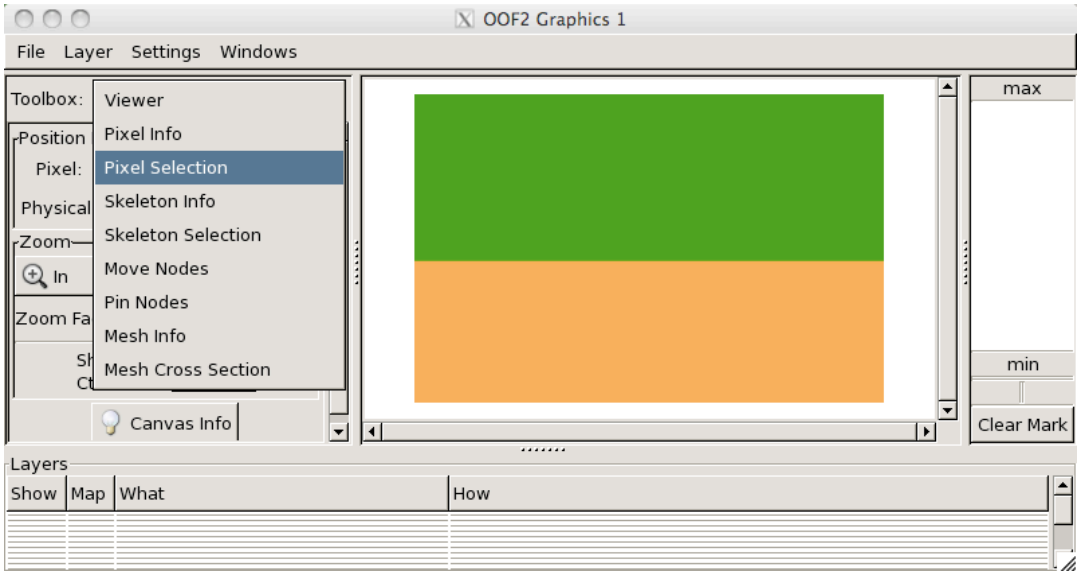

From the method menu, click on “Burn”.

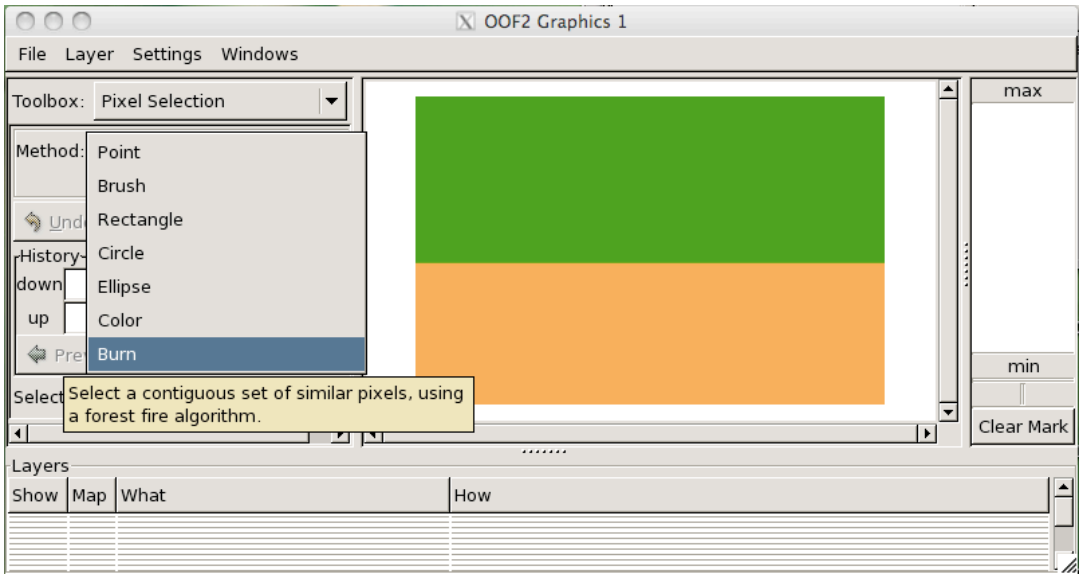

You can try other method to play around with it. “Burn” method simple let you select all pixels of the same kind with a single mouse click.

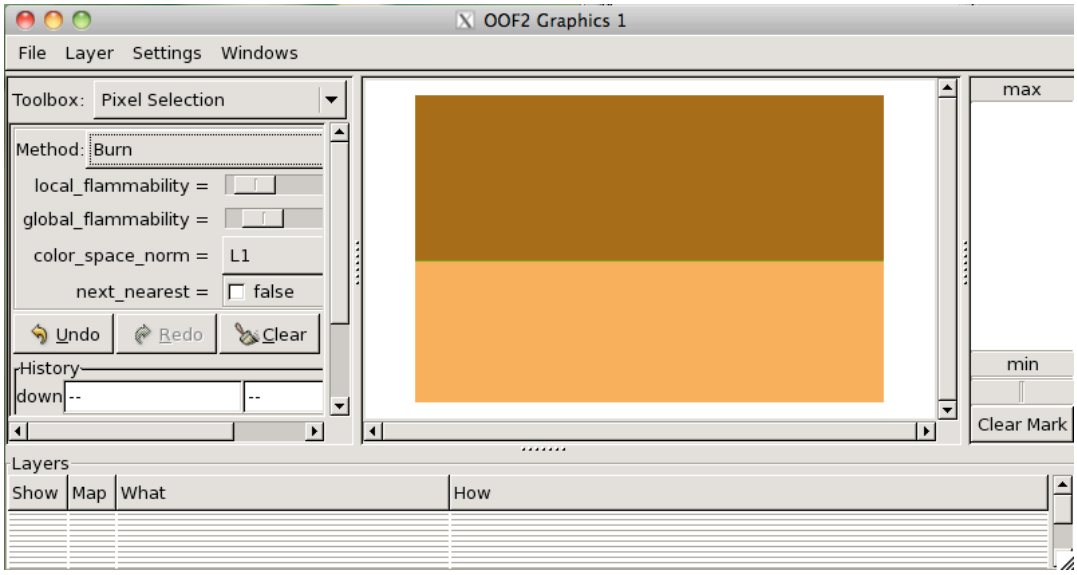

If you click on the green image on top, the color will change - indicating that you have selected all the pixels in green. Now go back to the main window and click on “top” pixel

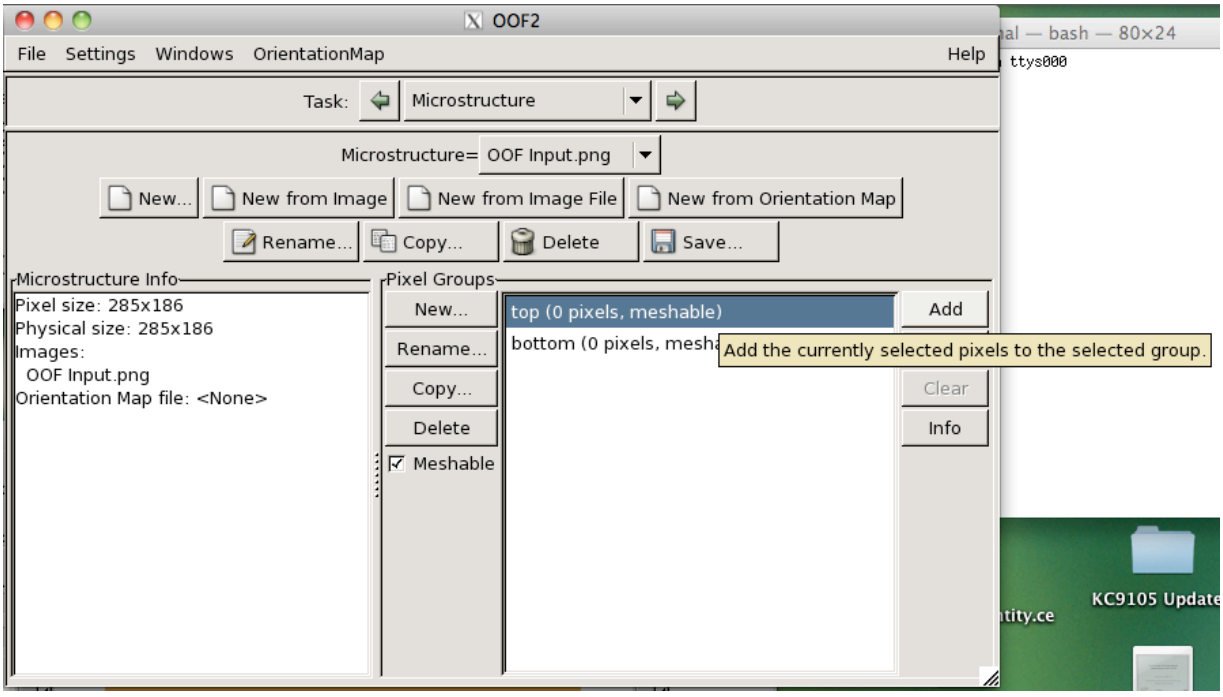

group to highlight it and click “Add” in the right hand side.

You will notice that now we have 28500 pixels in the “top” pixel group. Now we want to do the sample for the “bottom” pixel group.

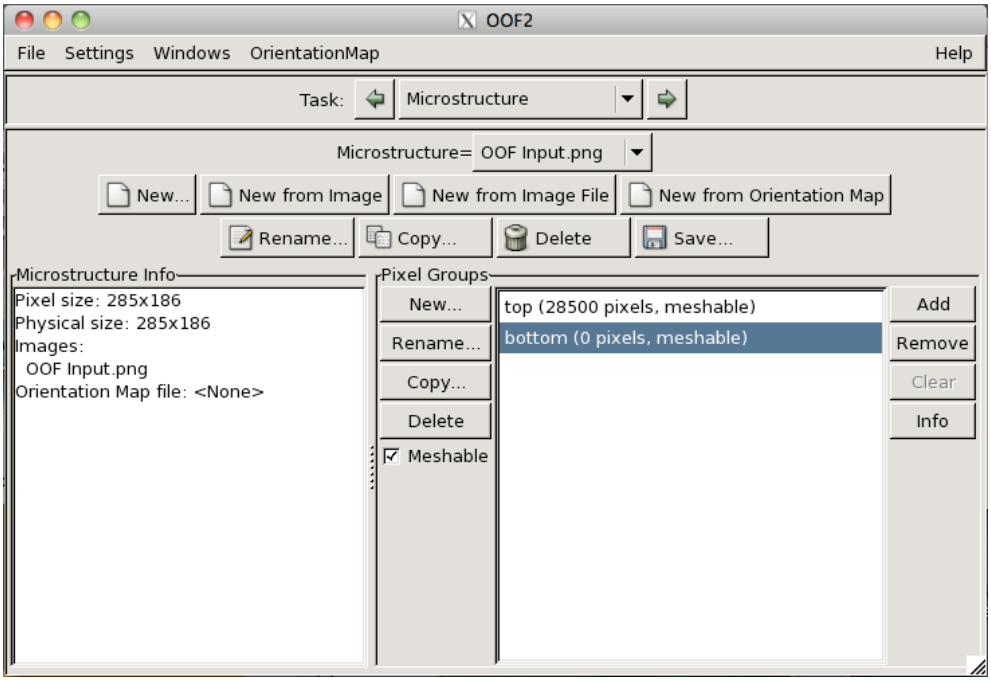

Go back to the graphics menu and click on the bottom orange image to highlight it.

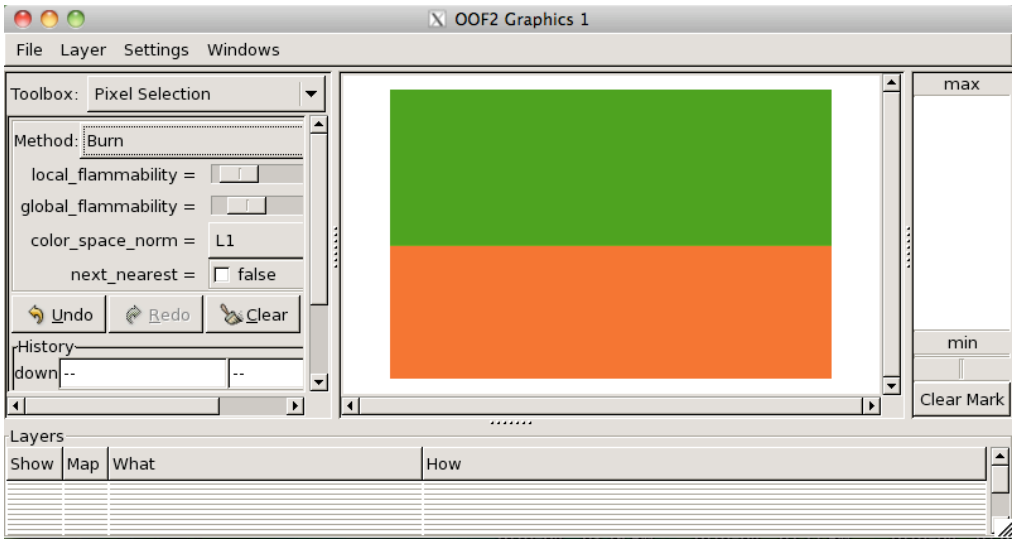

Go back to the main menu and click on the “bottom” pixel group to highlight it. Click on “Add” again to add pixels to the “bottom” pixel group.

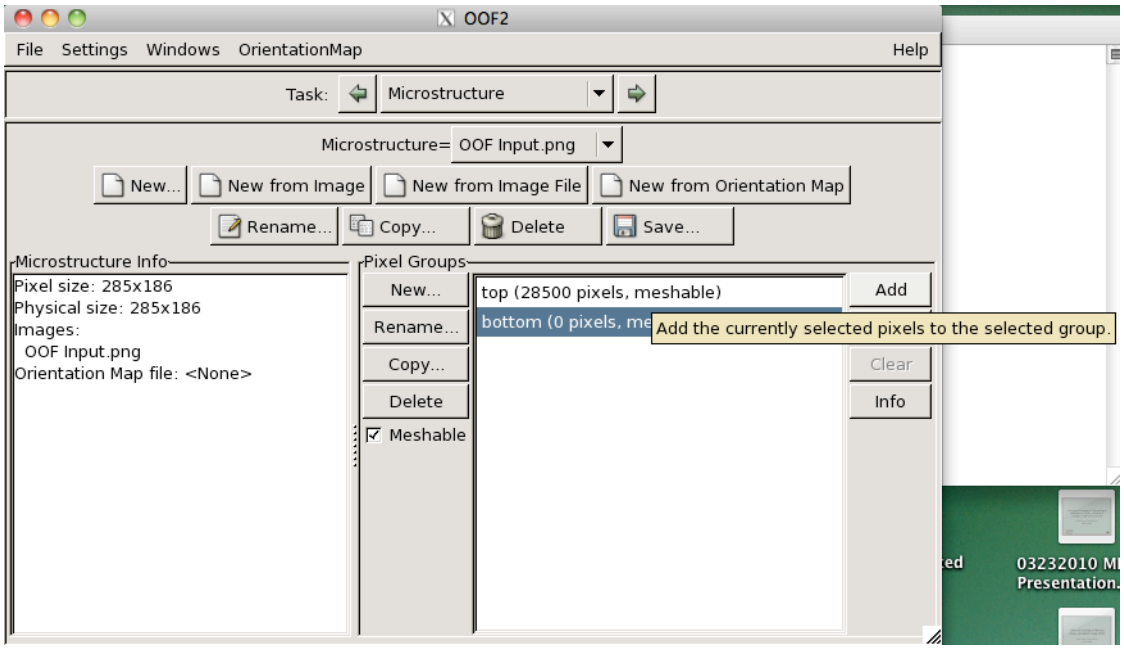

Now we are done with the pixel selection process. Let’s move on to the materials property assigning.

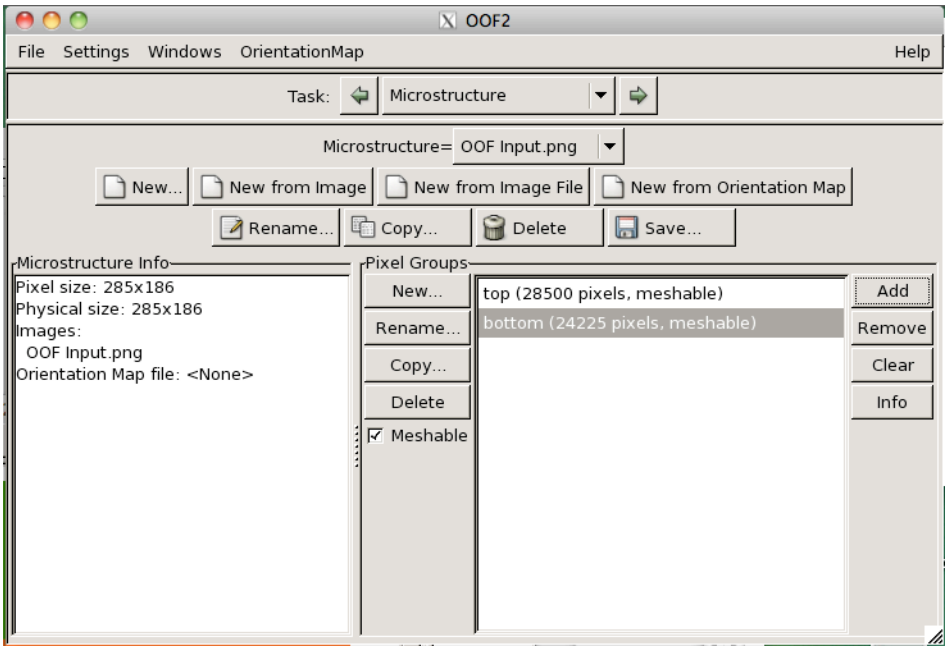

Click on “Task” menu and select “Materials”.

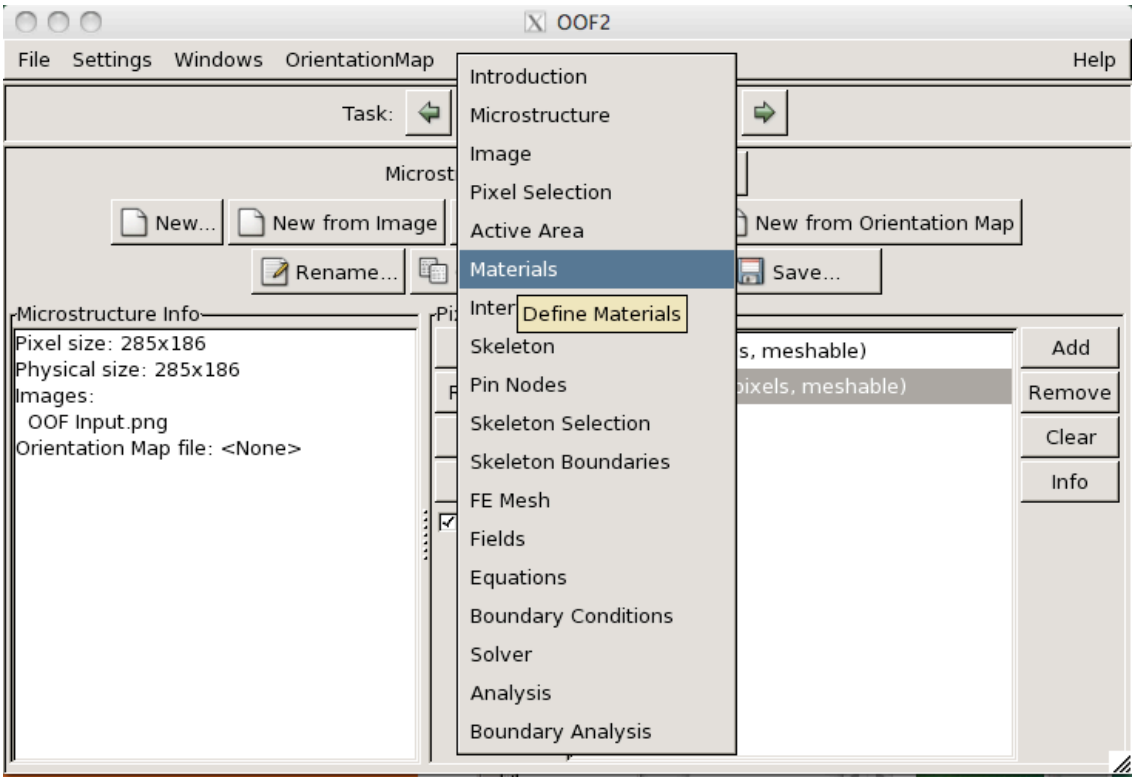

You will be in this Materials page.

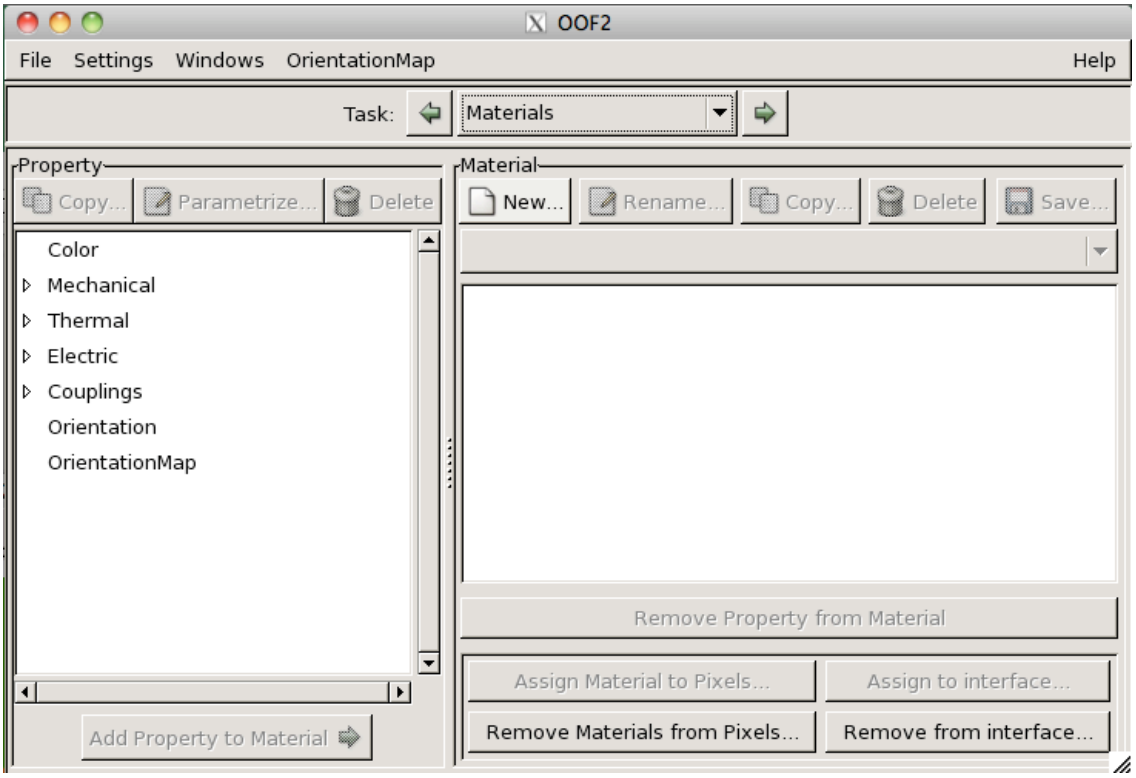

Here you will need to create 2 different materials files and assign them to the correct pixel groups we have done. We will create one materials file called “top” and assign it to the pixel group “top” and do the same for “bot”.

From Materials - click on New - click on in the checkbox and give a name called “top”. Note that the name here does not have to match with the ones in pixel group. You can call it as “top_material” or whatever you want but no space between 2 words.

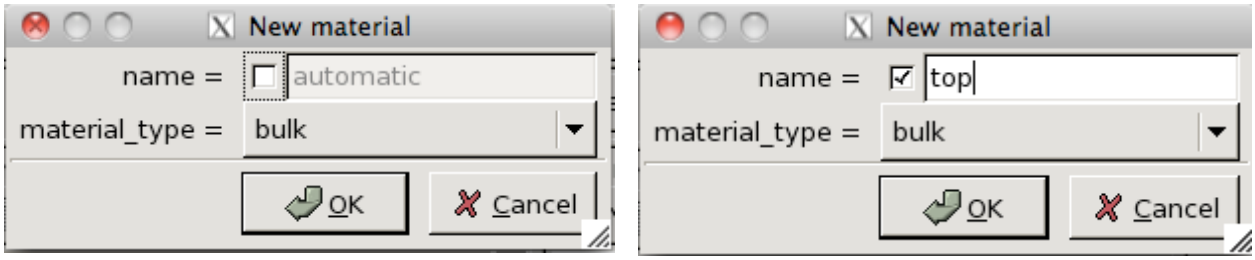

Now we are in this top “Material” page and click on Mechanical > Elasticity > Isotropic from the “Property” box

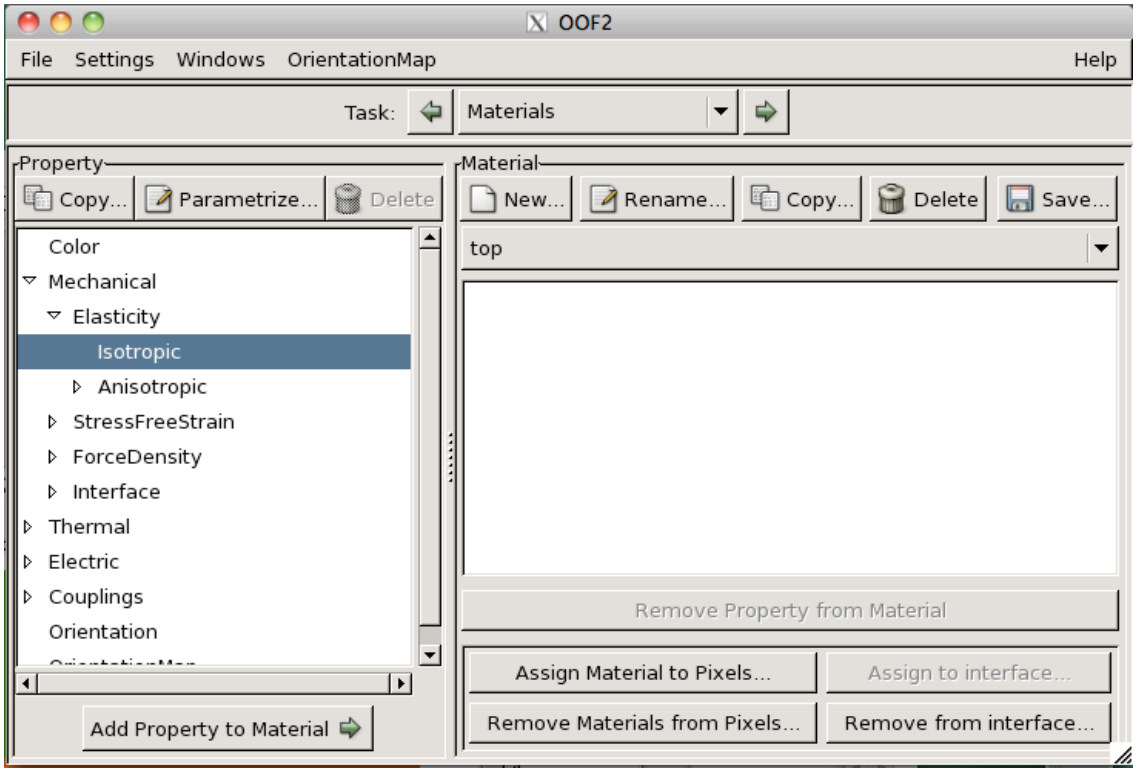
OOF2
File
Settings
Windows
OrientationMap
Help
Task:
Materials
Property
Copy...
Parametrize...
Delete
Color
Mechanical
Elasticity
Isotropic
Anisotropic
StressFreeStrain
ForceDensity
Interface
Thermal
Electric
Couplings
Orientation
Add Property to Material
Material
New...
Rename...
Copy...
Delete
Save...
top
Remove Property from Material
Assign Material to Pixels...
Assign to interface...
Remove Materials from Pixels...
Remove from interface...

Click and highlight “Isotropic” and click on copy. A window will pop out and give a name called “topMaterial”

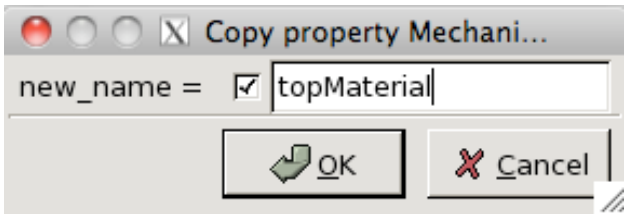

You will see a “topMaterial” file created. Highlight it and click on “Parametrize”

Here you can give assign values such as tensor properties or Young’s modulus and Poisson’s ratio. For this tutorial we are going to scroll down the menu to “E and nu”

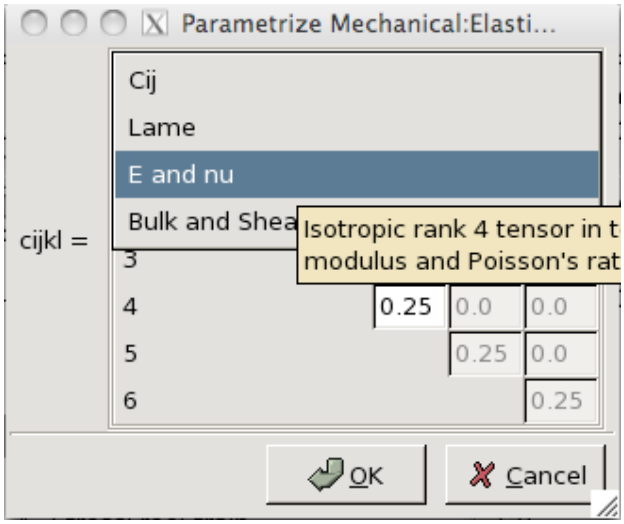

We assign 300 to the Young’s modulus and 0.3 for the poisson’s ratio

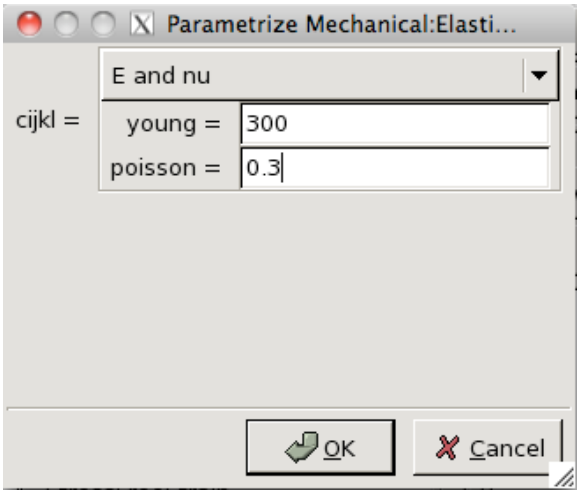

Click OK and click on “Assign Property to Material” on the bottom left of the main menu

You will see that the “top” material file has this values added. Now we want to add coefficient of thermal expansion into this file

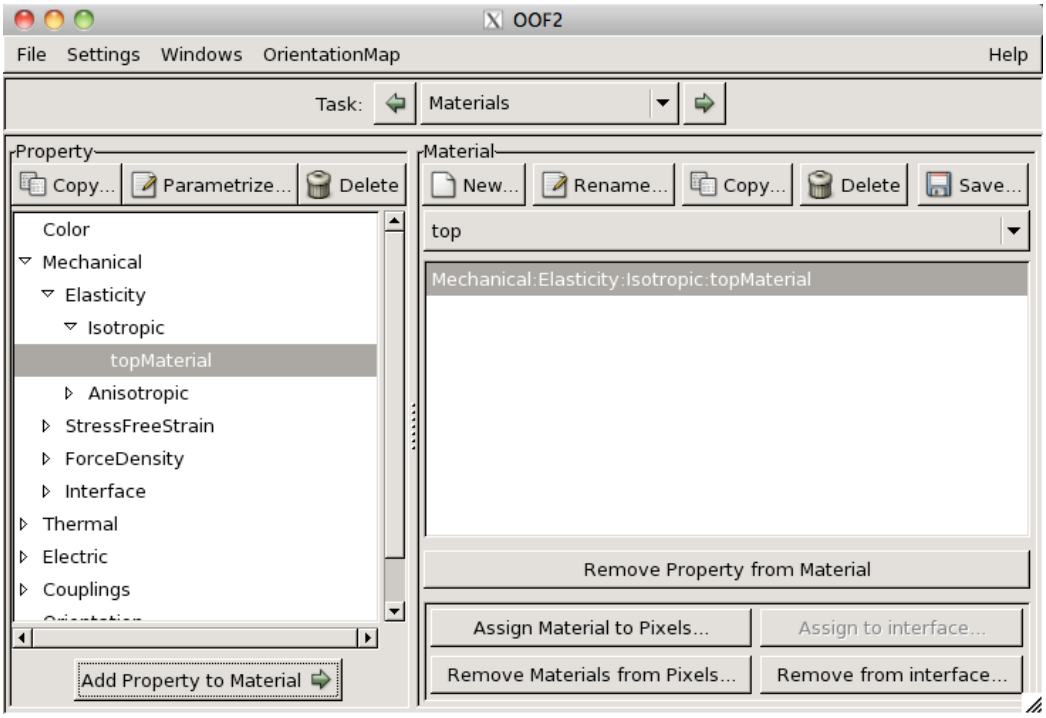

Click on Couplings > ThermalExpansion > Isotropic

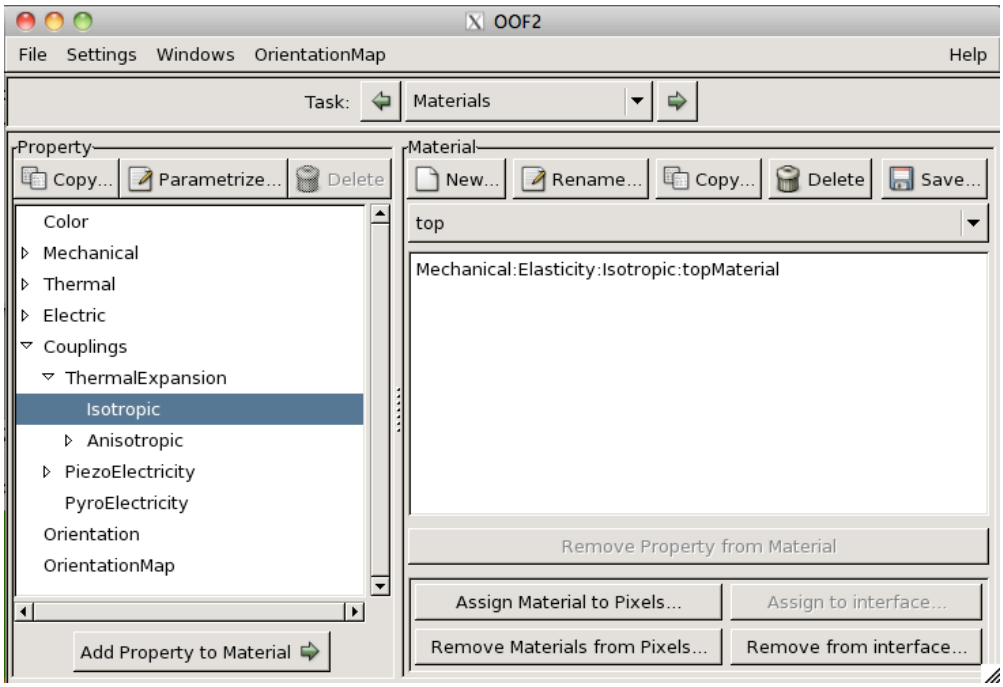

Click on “Copy” again and give a name “topMaterial”

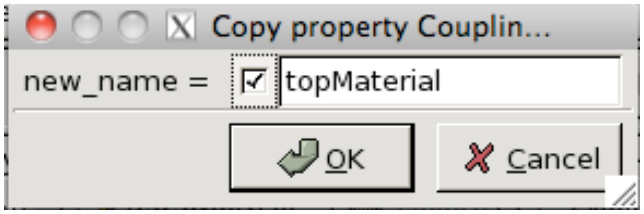

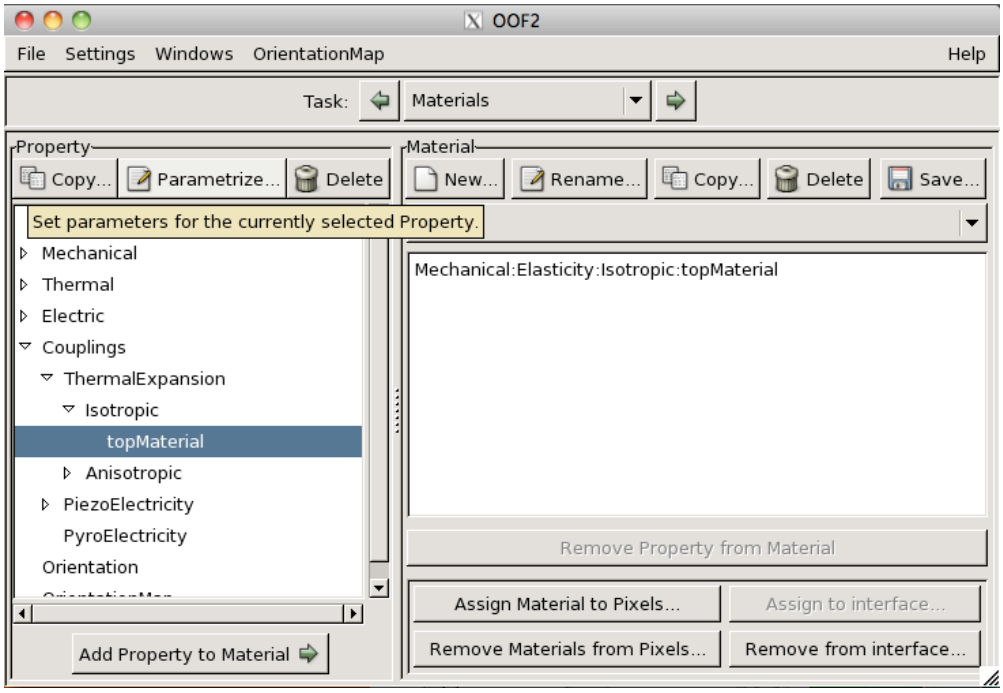
OOF2
File
Settings
Windows
OrientationMap
Help
Task:
Materials
Property
Copy...
Parametrize...
Delete
Set parameters for the currently selected Property.
Mechanical
Thermal
Electric
Couplings
ThermalExpansion
Isotropic
topMaterial
Anisotropic
PiezoElectricity
PyroElectricity
Orientation
Add Property to Material
Material
New...
Rename...
Copy...
Delete
Save...
Mechanical:Elasticity:Isotropic:topMaterial
Remove Property from Material
Assign Material to Pixels...
Assign to interface...
Remove Materials from Pixels...
Remove from interface...

Highlight “topMaterial” and click on Parametrize. For alpha (coefficient of thermal expansion) for the material on top, we are going to assign 0.000003.

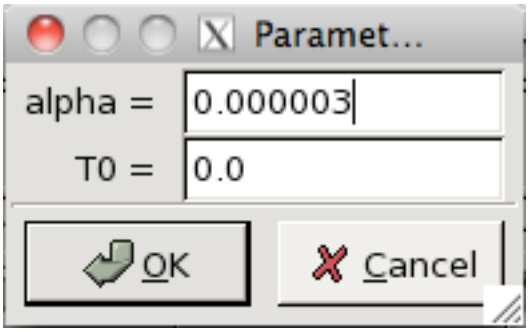

Click on “Add Property to Material” to add the thermal expansion value into the file.

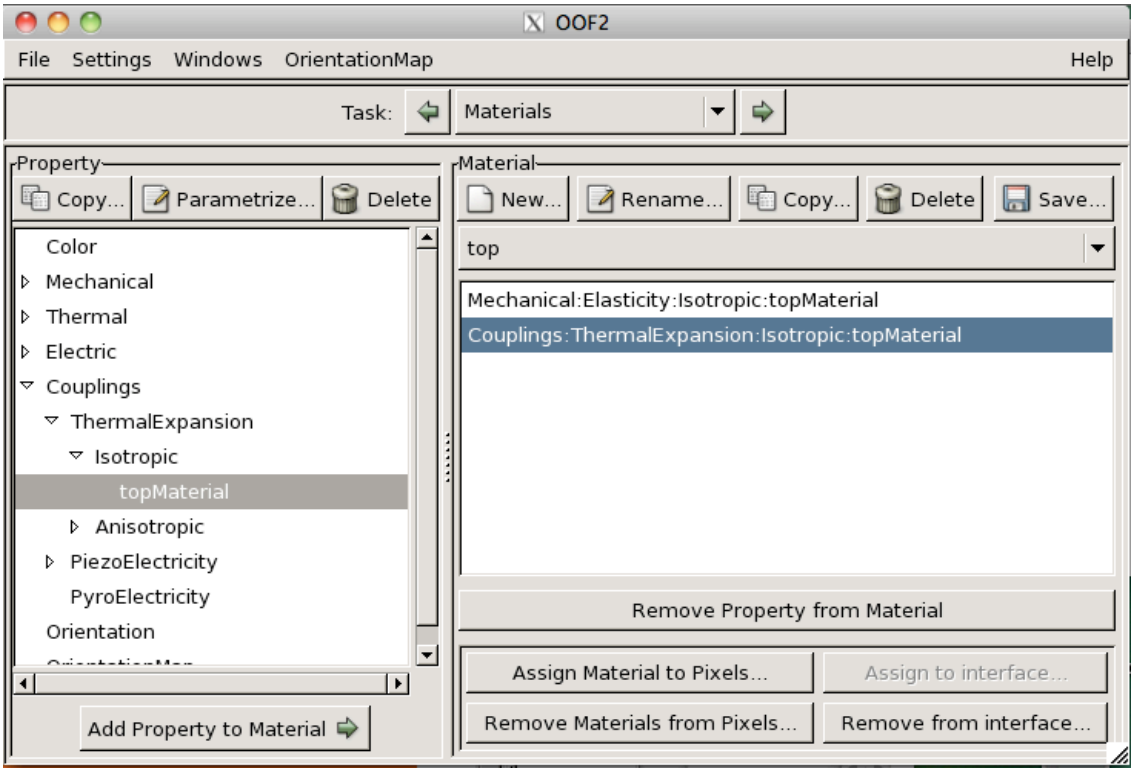

Now, underneath the Material file. there are file buttons, click on “Assign Material to Pixels”.

A window will pop out and we want to select “top” for the microstructures. Note that these are the pixel groups we created in the previous tutorial (from page 2 - 6)

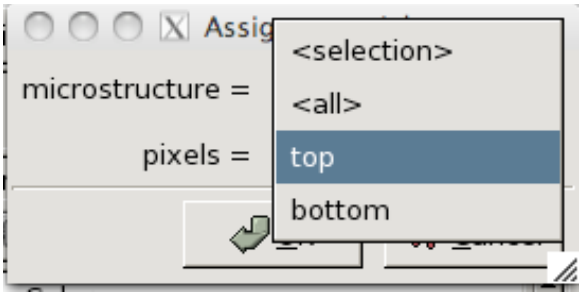

Now we will want to create another material file for bottom material. Follow the same steps above and assign these values for bottom

Young’s Modulus: 500

Poisson’s Ratio: 0.3

Coefficient of thermal expansion: 0.000005

Note that you will need to add the values to the material file you created and assign them to the “bottom” pixel groups.

We will move on to the “Skeleton” part of the tutorial

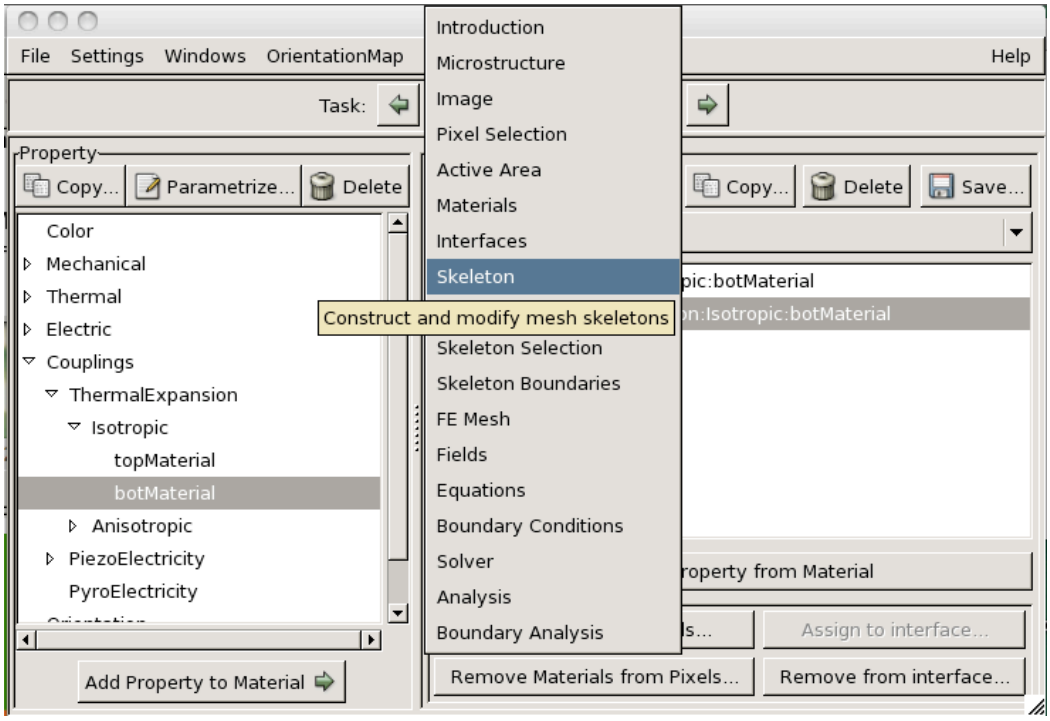
File
Settings
Windows
OrientationMap
Help
Task:
Property
Copy...
Parametrize...
Delete
Color
Mechanical
Thermal
Electric
Couplings
ThermalExpansion
Isotropic
topMaterial
botMaterial
Anisotropic
PiezoElectricity
PyroElectricity
Add Property to Material
Introduction
Microstructure
Image
Pixel Selection
Active Area
Materials
Interfaces
Skeleton
Construct and modify mesh skeletons
Skeleton Selection
Skeleton Boundaries
FE Mesh
Fields
Equations
Boundary Conditions
Solver
Analysis
Boundary Analysis
Copy...
Delete
Save...
pic:botMaterial
on:Isotropic:botMaterial
roperty from Material
Assign to interface...
Remove Materials from Pixels...
Remove from interface...

You will always need to click on “New” to start creating skeletons

Since this is a simple structure, we are going to use 10 by 10 and select “TriSkeleton” as the skeleton geometry. Here TriSkeleton means the the finite element is going to be triangles (you can merge these triangles later on). Quadskeleton means that the finite element is going to be in quad (four sided) shape.

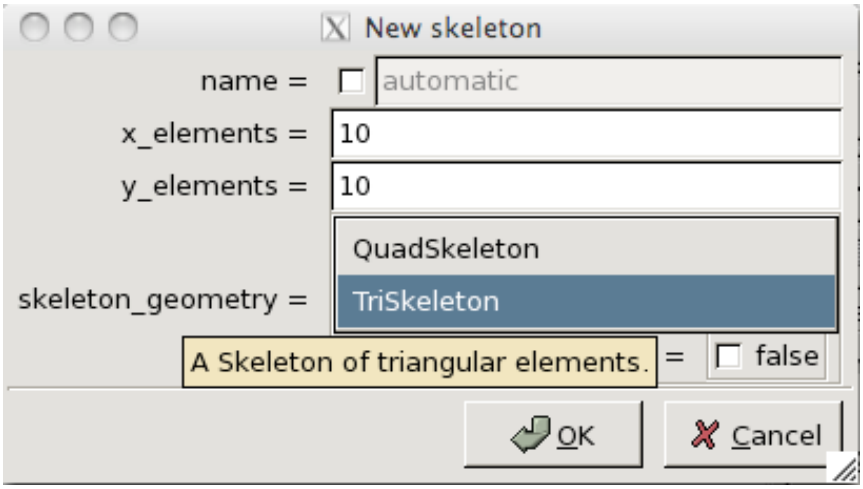

Click OK to move on ~ You should be able to see skeleton built up in the graphics menu

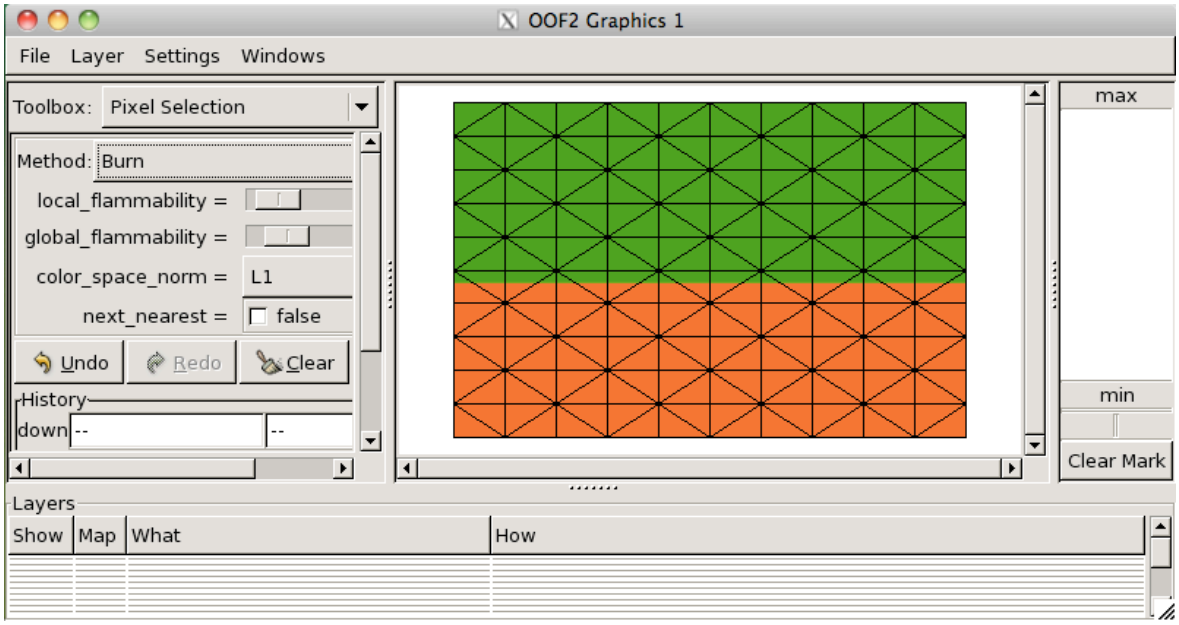

In the skeleton menu, you can modify the skeleton and look at how good your skeleton

is by looking at the “Homogenerity Index” in the Skeleton Status on the left. This value is the average homogeneity within each element. Basically you want to try to get this value as close to 1 as possible in simple structures. If you have complicated structure with more than 50,000 elements in it, the value has to be as close to 0.85 as possible.

Now click on Snap Refine from the skeleton modification method and click OK

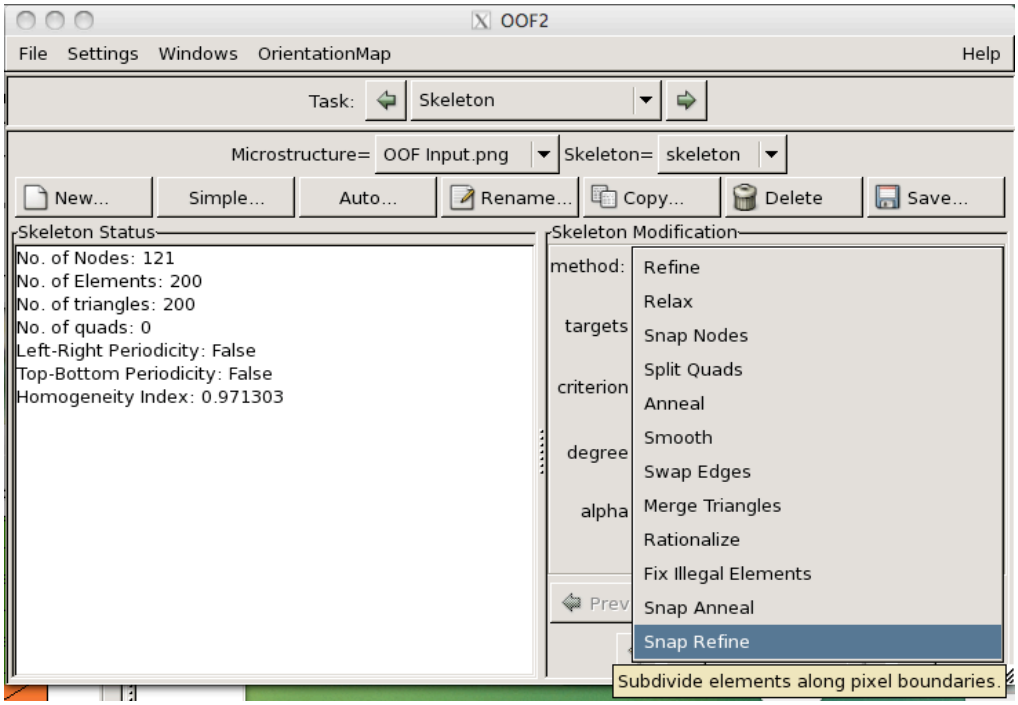

The skeleton will refine itself based on the pixel groups.

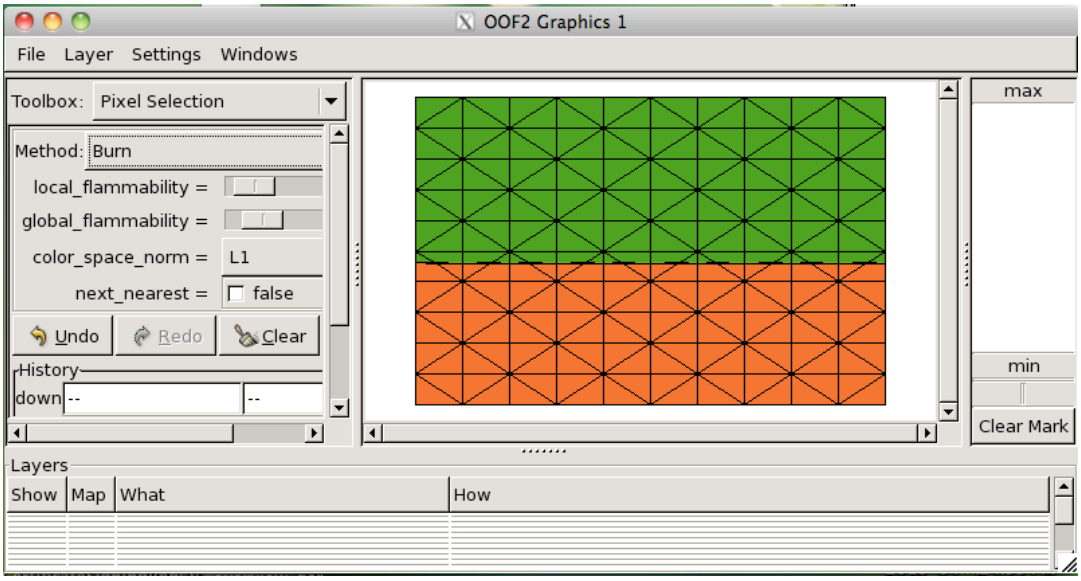

Note that the homogeneity goes up to 0.997 after that. Now we can select “Merge Triangles” method and click OK.

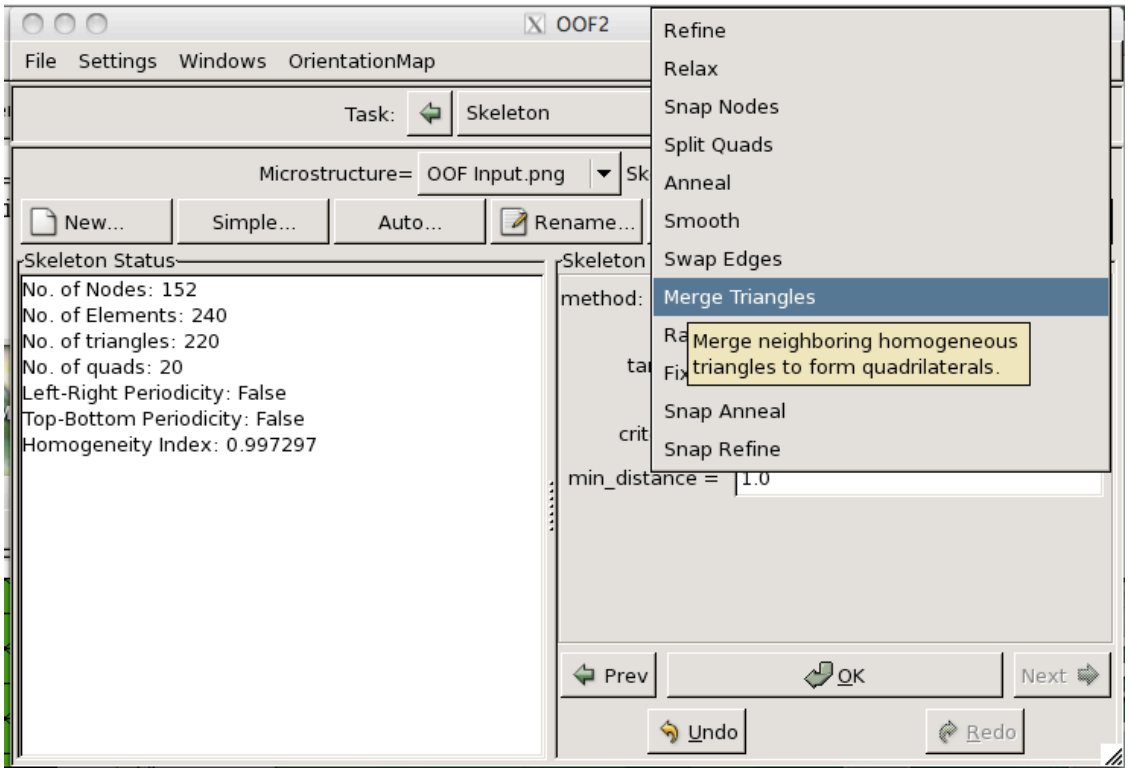

Note that the triangles in each pixel groups have been merged to become rectangular shape. There are different other skeleton modification method you may want to try out if you have lots of elements (>5000) or your skeleton is very complicated.

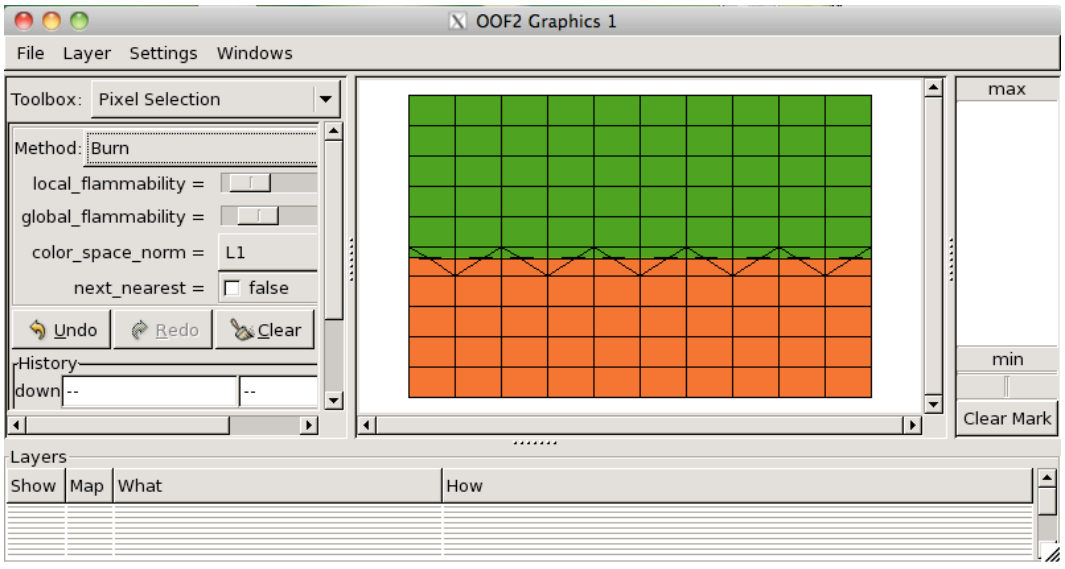

Now we can move on to the finite element mesh part. Click on “FE Mesh” from the Task menu.

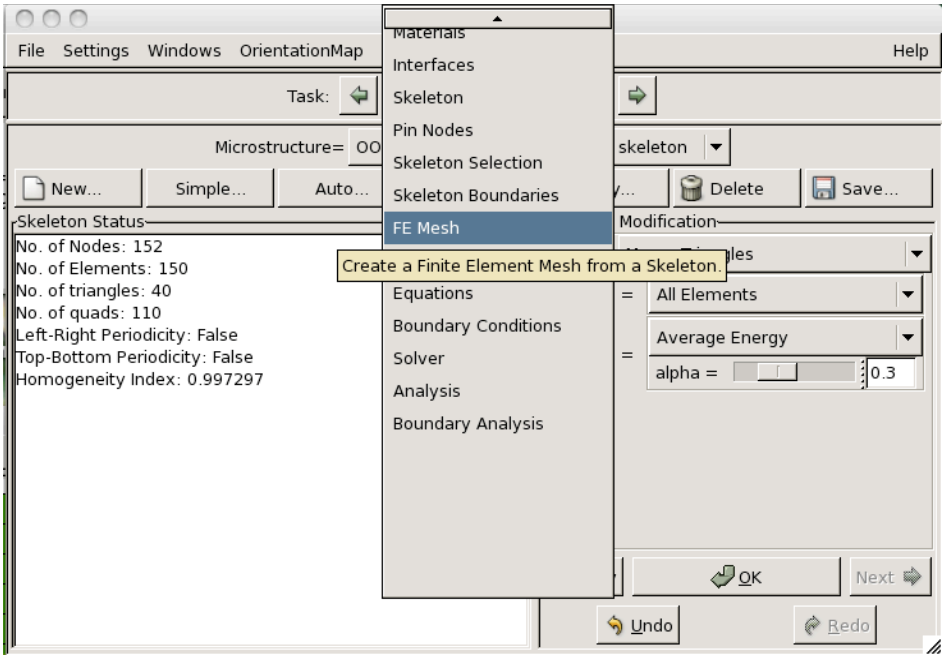

Click New

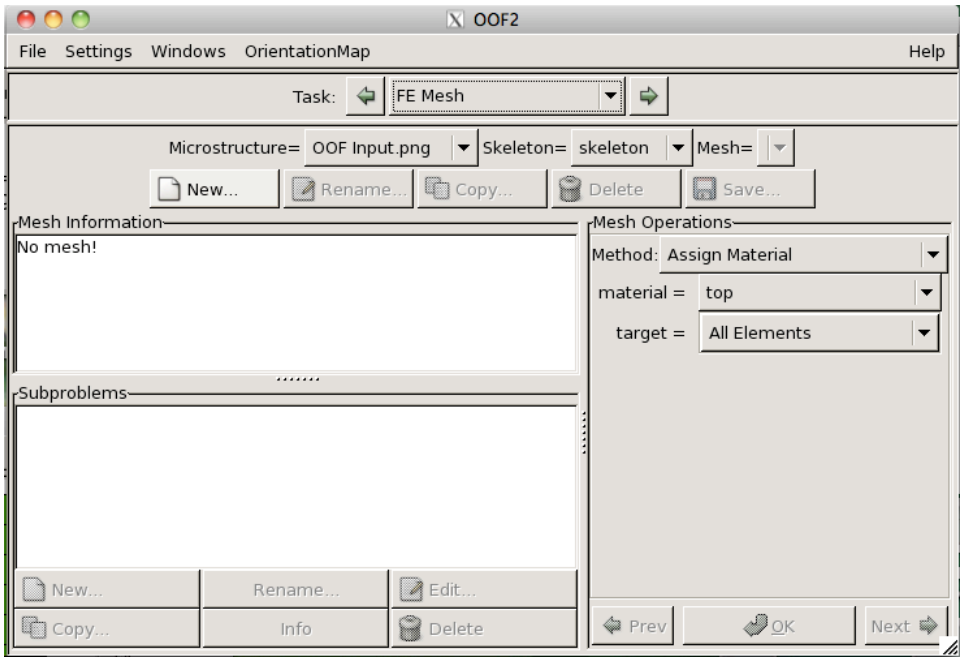

Here you can just click OK and mesh will be built automatically.

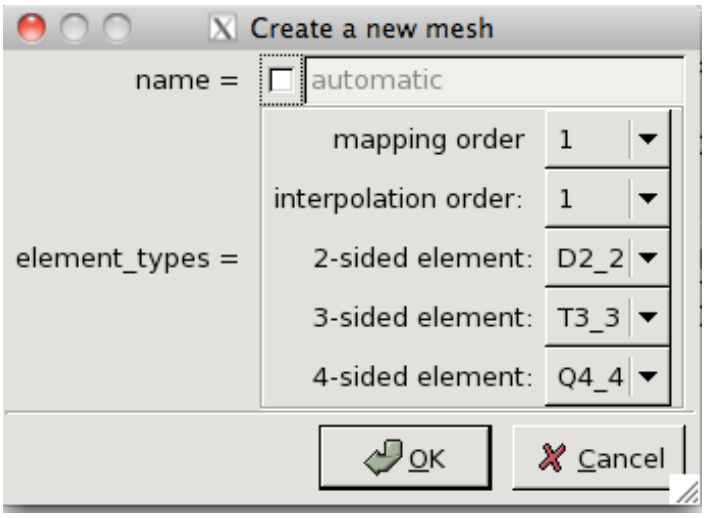

In OOF2. Mesh is built directly on top of the skeleton. You cannot modify the shape of the mesh. The only way you can change the shape of the mesh is through the skeleton menu, where you will have to delete the mesh you created and go back to skeleton to modify it. Once thats done you have to come back and create a new file.

Note that you will need to have materials properties assigned to the pixel group before proceeding to create mesh.

Once the mesh is built your window will look like this.

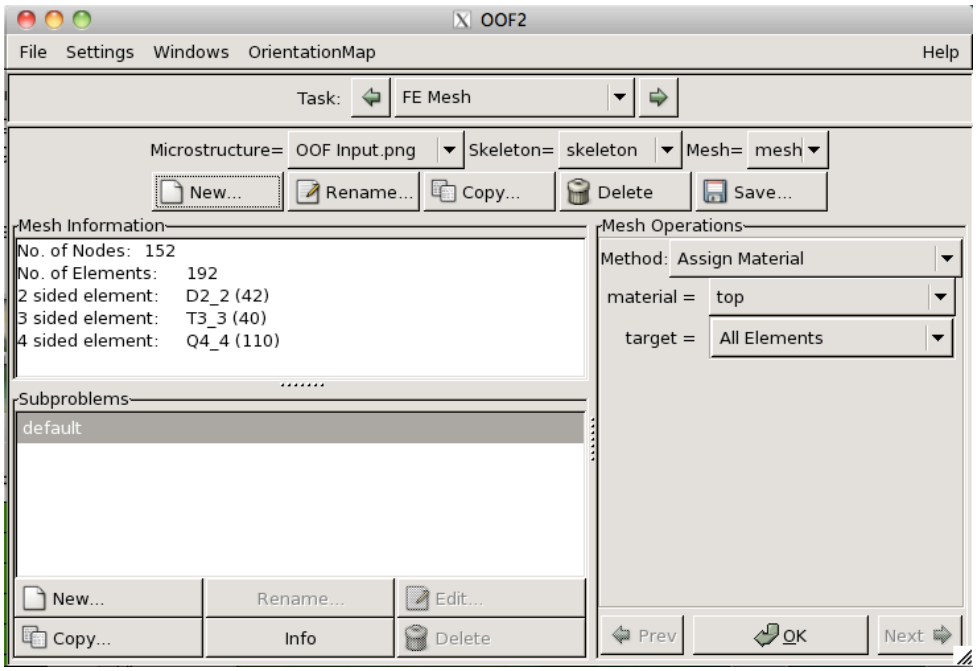

Now we can move on to the “Field” page

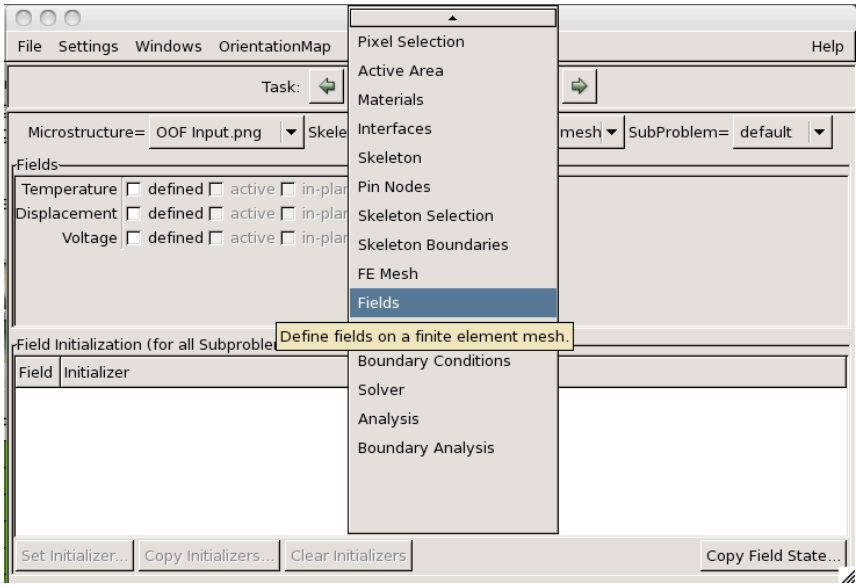

Click on the Temperature defined box and the Displacement defined box shown below. Also click on “active” for Displacement. When the defined box is checked, that means that these values will be in used as parameters in the equations (We will set this in the next Task menu) you want to solve. By activating it, you will be able to define boundary conditions based on these parameters. By clicking the in-plane value you are telling the mesh to include an out of plane derivatives.

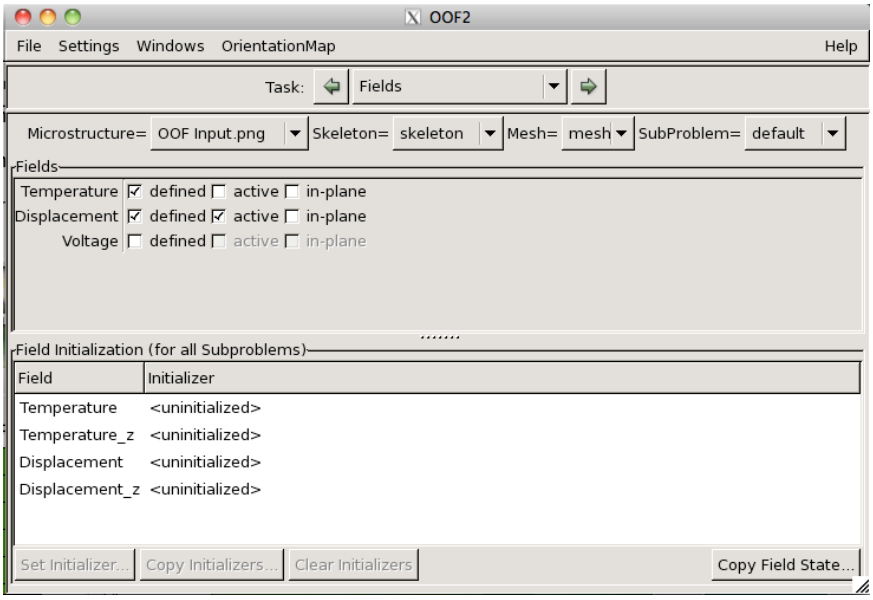

Highlight the Temperature field under Field Initialization and click on “Set Initializer”. Set the menu to be “Constant” and assign -800 to the value.

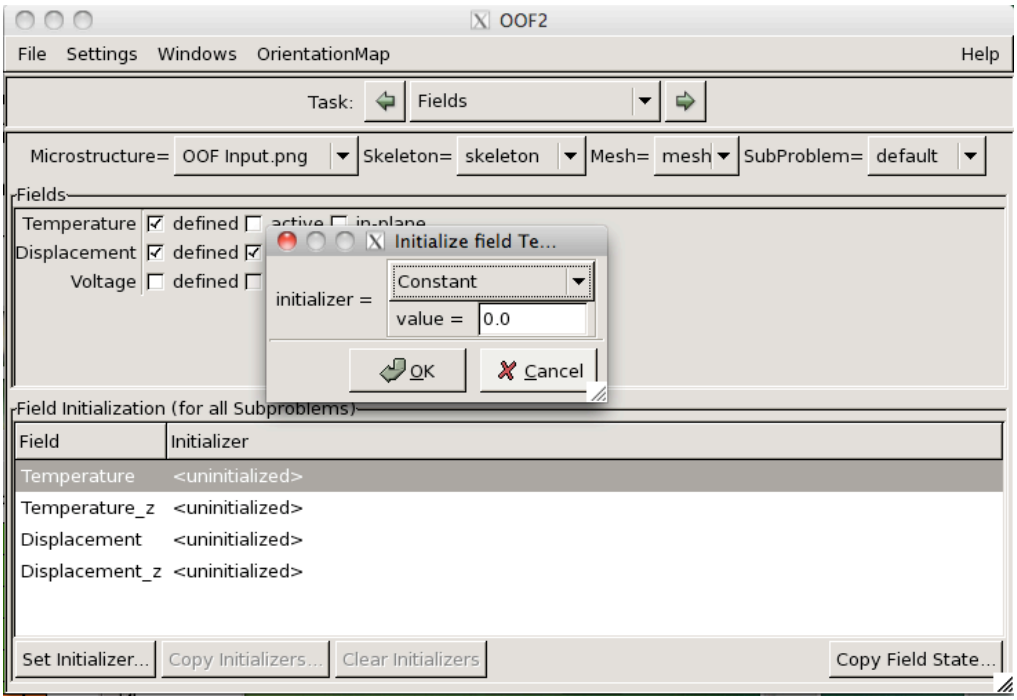

Your main menu for “Field” will look like this below:

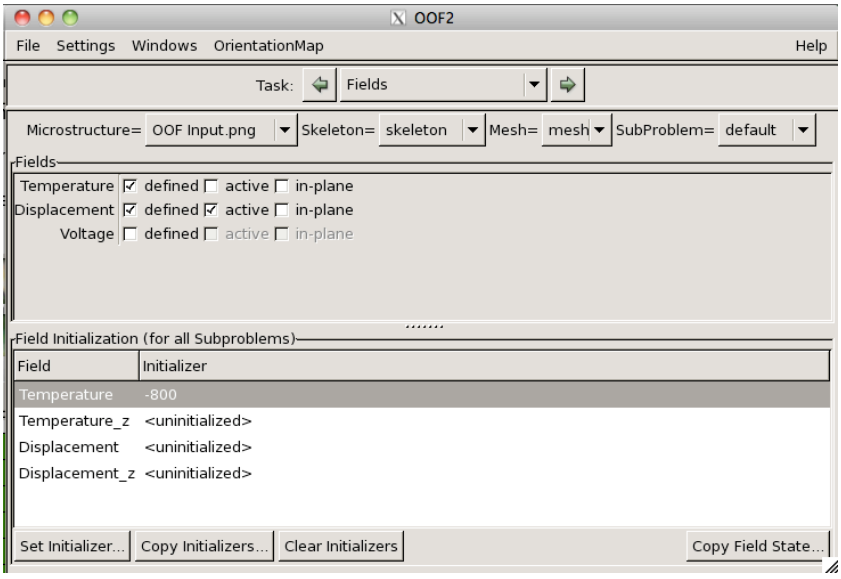

Now we can go to the “Equations” under Task menu. Check the box of “Force Balance” and “Plane Stress”.

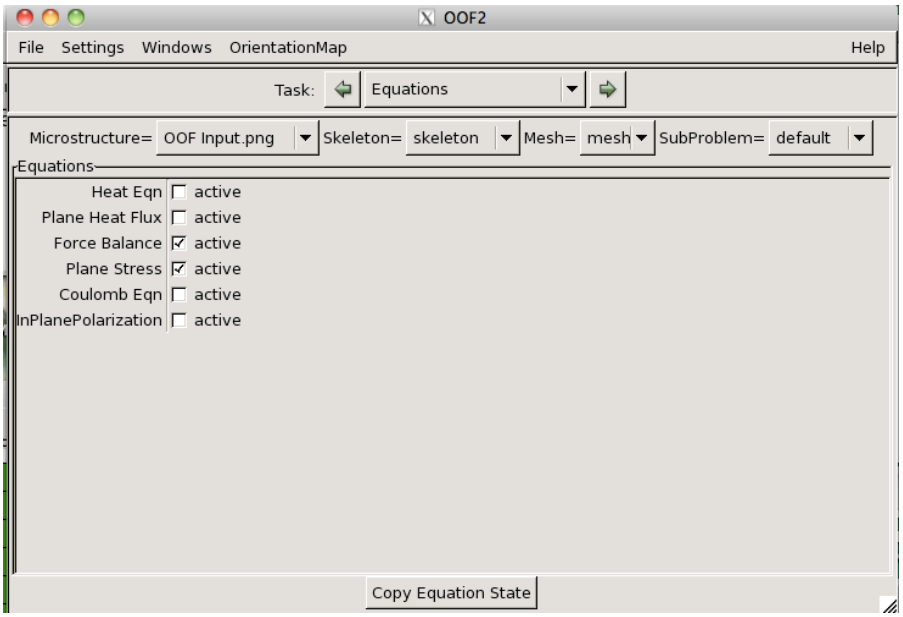

After that you can proceed to “Boundary Conditions” and click “New” to assign fixed boundary conditions like zero displacement on four size of the system. In this tutorial we will work on zero stress and assign no boundary conditions.

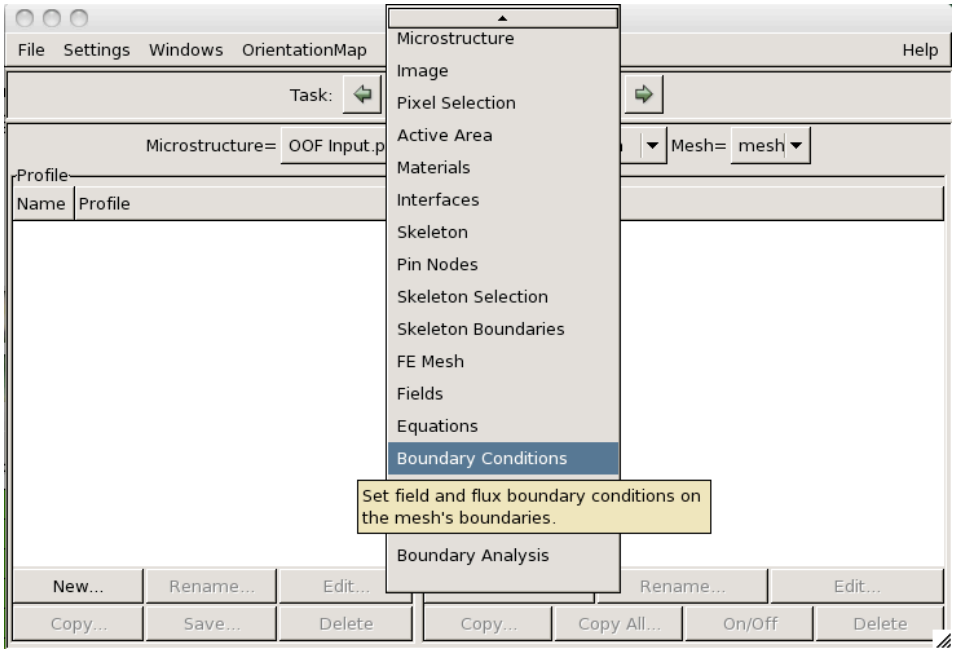

Now we are ready to solve our problem. Move on to “Solver” under Task Menu.

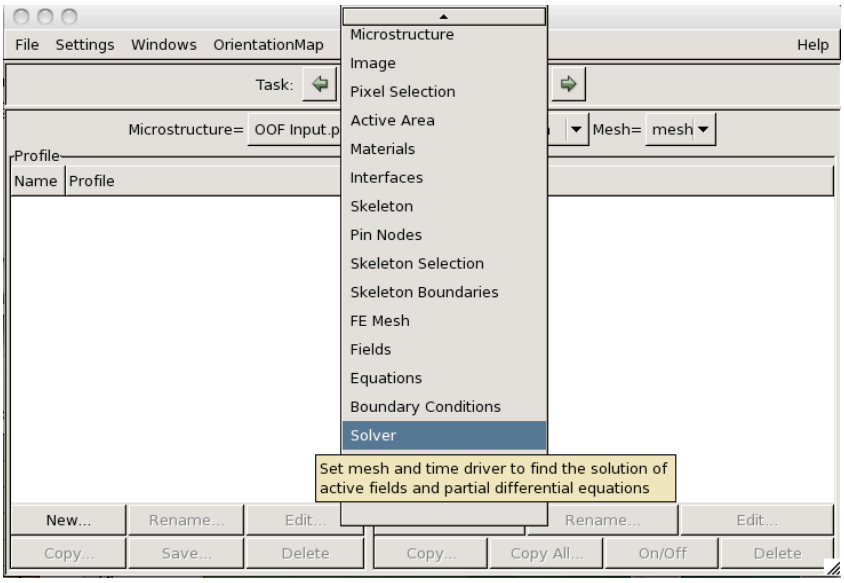

Click “Solve” on the bottom right corner. I am using Linear Drivers here - you can use different solvers and try see how your result will be different. When you get the message on the left saying “CG converged”, that means that you have successfully solved the problem

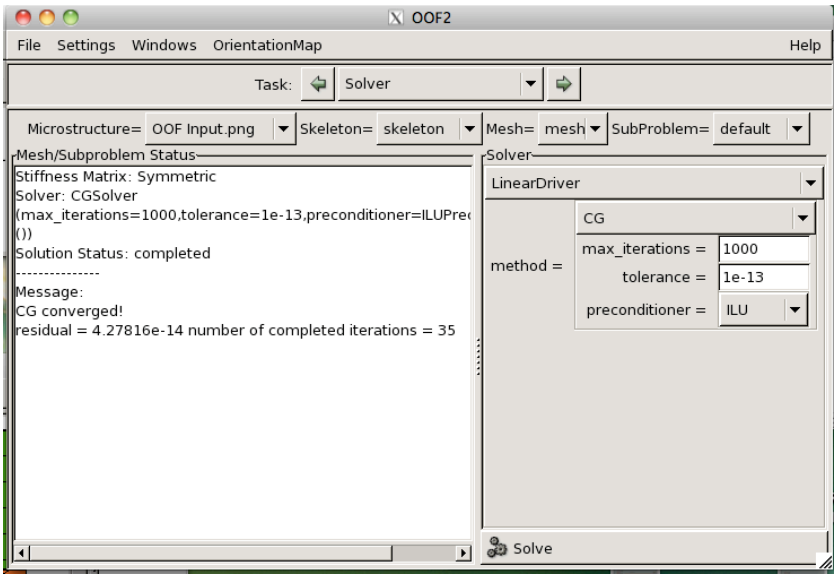

To view your solution, you have to go to the graphics windows. Click on Layer > New.

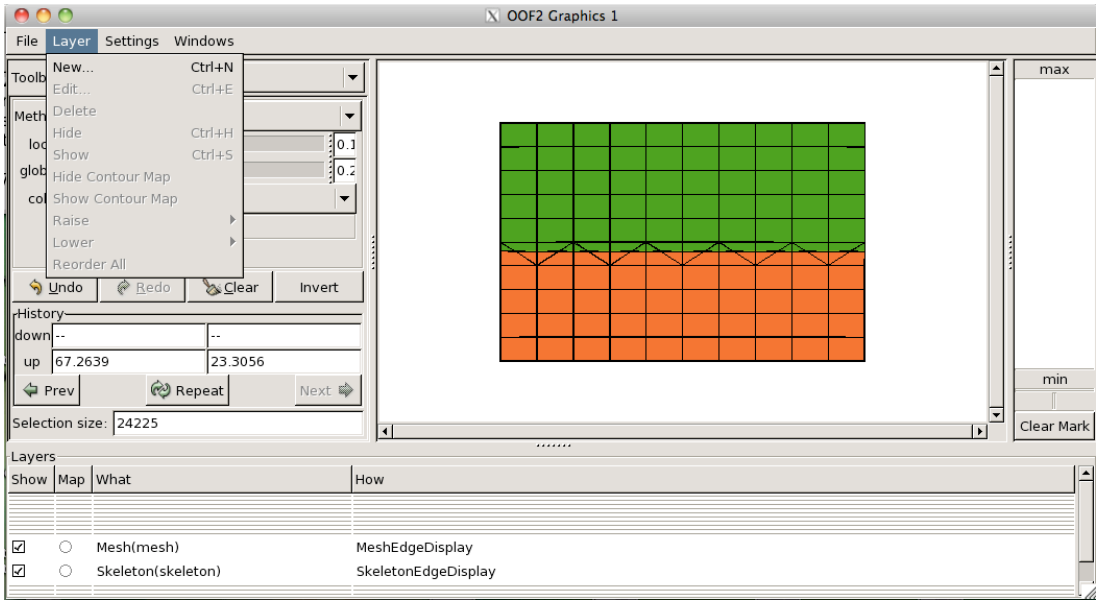

A window will pop out called the OOF2 Graphics Layer Editor. Click on the category menu and click on “Mesh”.

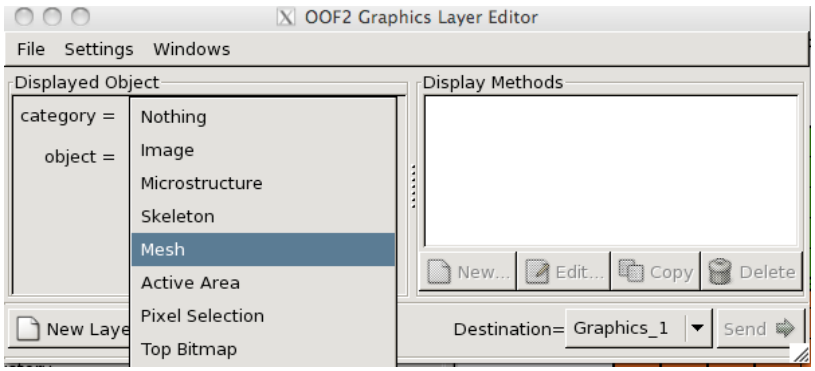

From the Display Methods, click on New

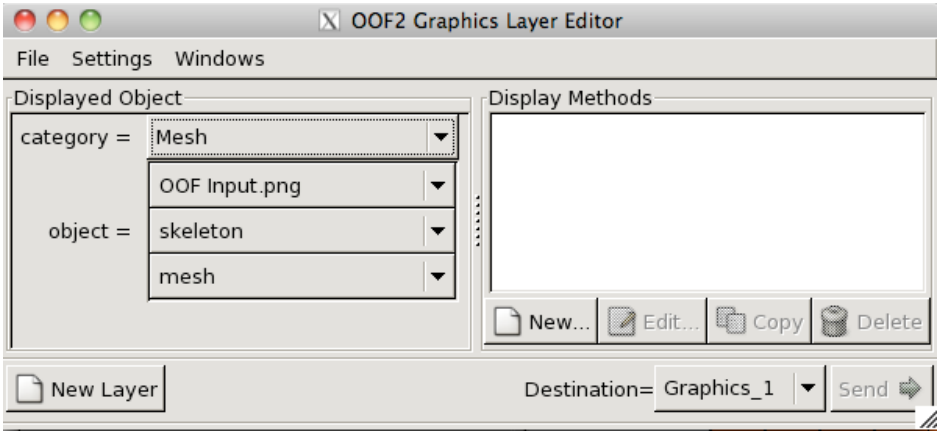

A window called New Display Method for Mesh m... select “Filled Contour” as method.

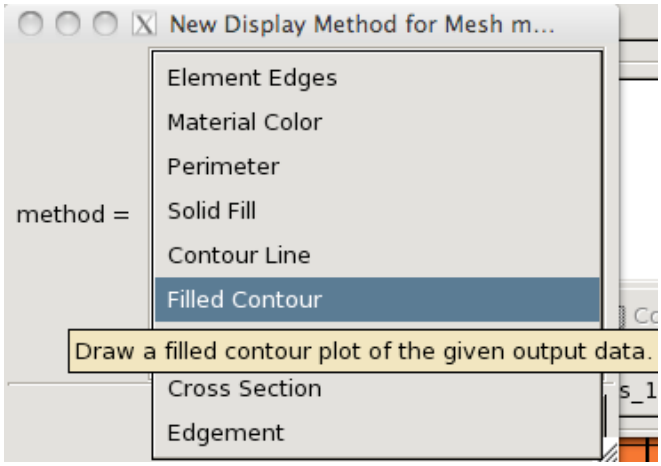

Here you will be able to see the things you want to plot. Click on “Flux” from the what menu.

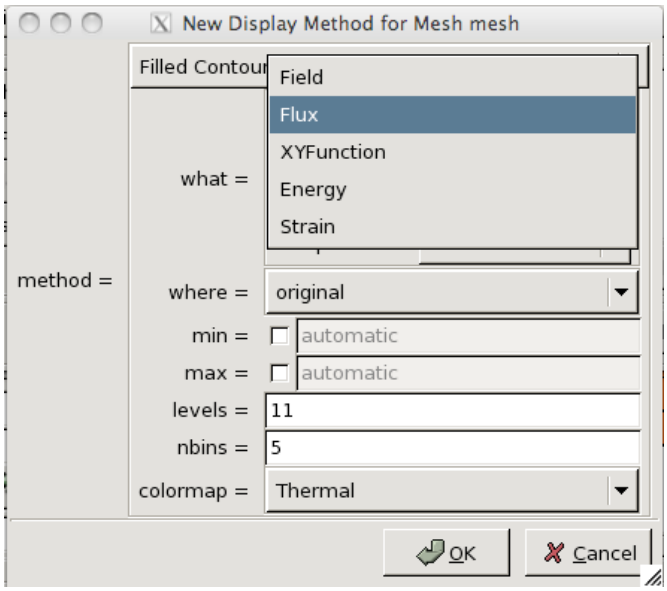

Here we want to solve the stress along the xx direction. So we will set the flux = stress and the component = xx

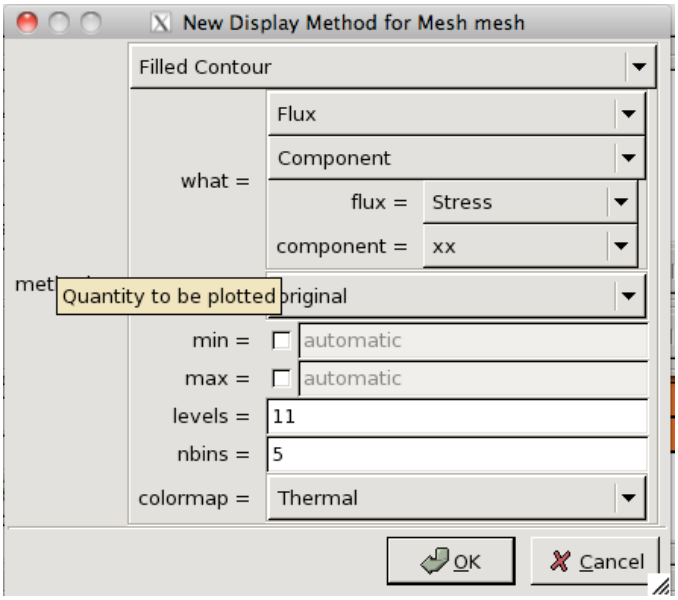

After click OK the system will automatically plot the solution and here it is:

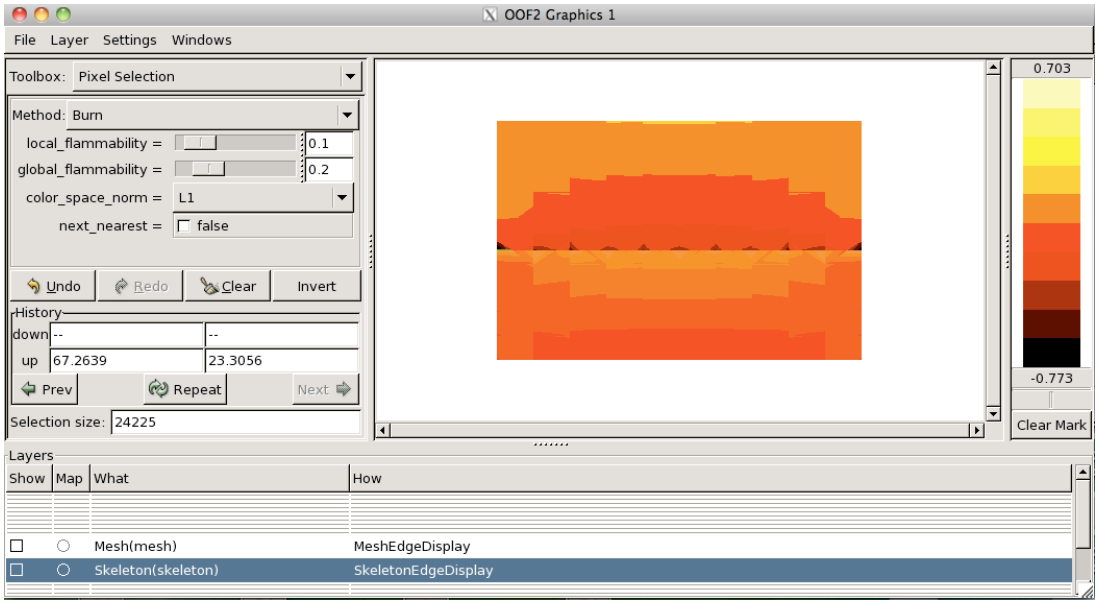

You can definitely plot the graph for elastic energy density, strains, or other things using the same method. Note that the scale bar only has 11 levels because that is the default value. You can plot it with 30 different levels for better quality in the Display Method. Also you can choose the max and min for the scale bar in the Display Method window as well.

If you have any questions about the units: OOF2 does not encounter this problem. The units of what your input is will also be the units of your output. For example, we have assigned 500GPa for the top material in the beginning. For the result, we are getting a scale from 0.703 to -0.773. The unit of 0.703 will be GPa or 703 MPa.